

Study of nonlinear structures and dynamics  
in collisionless plasmas created by the  
interaction between high power laser and  
cluster medium

Ryutaro Matsui

## Abstract

Due to an interaction between an ultra-short and high-power laser pulse with a peak intensity of  $10^{21-22}$  W/cm<sup>2</sup> and a medium consisting micron-size spherical dense objects (cluster medium), high energy density plasmas in the relativistic regime are produced. Based on the understanding of such plasmas, the work in this PhD thesis reveals the structure and dynamics of a collisionless plasma boundary layer, which is generally formed in an interface between the expansion front of a supernova and an interstellar gas, and presents a new way of producing a high quality protons exceeding 100 MeV, which is applicable to medical applications, e.g., cancer therapy. We performed numerical simulations utilizing particle based integrated code, EPIC3D, and reached following conclusions.

Firstly, the structure and dynamics of the boundary layer in between two distinct collisionless plasmas created by the interaction between a cluster and a laser pulse in the presence of an ambient gas is studied with two-dimensional (2D) particle-in-cell (PIC) simulations, which is described by three successive processes. *In the first phase*, a collisionless electrostatic shock wave, launched near the cluster expansion front, reflects the ambient gas ions at a contact surface as a moving wall, which allows a particle acceleration with a narrower energy spread. *In the second phase*, the contact surface disappears and the compressed surface of the ambient gas ions passes over the shock potential, leading to the formation of an overlapping region between the cluster expansion front and the compressed surface. Here, another type of nonlinear wave is found to be evolved, leading to a relaxation of the shock structure, while continue to reflect the ambient gas ions. The nonlinear wave exhibits a bipolar electric field structure which is sustained for a long time scale coupled with slowly evolving ion dynamics. This suggests that a Bernstein-Greene-Kruskal (BGK) type quasi-stationary kinetic equilibrium dominated by electron vortices in the phase space is established. *In the third phase*, a rarefaction wave is triggered and evolves at the compressed surface. This is because the ambient gas ions tend to pass over the potential of the bipolar electric field without reflection. Simultaneously, a ring-like structure, i.e., a kind of internal shock, is formed in the cluster due to the deceleration of cluster ions. The formation of such ring structures can be seen in many places in the universe. Such structure formations and successive dynamics accompanied by the transitions from the shock wave phase through the overlapping phase to the rarefaction wave phase are considered to be a unique nature at the boundary layer created by an explosion of a dense plasma object in an ambient dilute plasma.

Secondly, a new approach for producing highly-directional, quasi-monoenergetic protons reaching 300 MeV is investigated with three-dimensional (3D) PIC simulations. By the action of an ultrashort, high power laser irradiation, collisionless shocks are launched at a laser-irradiated hemisphere on a micron-size hydrogen cluster and propagate

---

toward the cluster center keeping a hemispheric shape. Subsequently, an electrostatic potential develops, leading to the shock acceleration and to the production of a quasi-monoenergetic proton bunch. During this process, when the pulse peak and shocks coinstantaneously reach the cluster center, a relativistic induced transparency (RIT), which temporarily increases the shock velocity, takes place. The RIT plays a role in keeping a monochromaticity of the proton bunch, while the shock structure starts to collapse after the RIT. After the shock acceleration, in the inside and outside of the cluster, the proton bunch is further accelerated in two stages by the electric field mainly derived from the Coulomb explosion. Ultimately, the kinetic energy of the proton bunch has a quasi-monoenergetic peak over 200 MeV, with  $\sim 10\%$  energy spread and  $\sim 5$  degree half-divergence angle via the effect of the RIT. This mechanism works for finite ranges of parameters with threshold values concerning the laser peak intensity and the cluster radius, resulting from the synchronization of the multiple processes in a self-consistent manner. The present scheme utilizing the internal and external degrees of freedom ascribed to the spherical cluster leads to the proton bunch alternative to the plain target, which allows the operation with high repetition rate and impurity free.

These conclusions in this PhD thesis is expected to help the understanding of various nonlinear structures and mechanisms of related particle accelerations in boundary layers not only in laboratory but also in space and universe. In terms of applications, the proposed ion acceleration scheme opens a promising way of developing high energy ions by laser plasma ion acceleration methods for medical and also industrial applications.

## Acknowledgements

Firstly, I would like to express all my gratitude to my supervisor Prof. Yasuaki Kishimoto for continuous support over the years of my master and PhD courses.

My sincere thanks also go to Doc. Yuji Fukuda for the fruitful support and guidance in the research. I would like to thank Doc. Kenji Imadera and Prof. Youichi Sakawa for fruitful advices, Doc. Tomohiro Masaki for technical support in simulation code, and Tomoko Takahashi and Renonna Ishii for helping me a lot support. Besides my advisers, I also thank the thesis committees.

I would like to thank all the members of Kishimoto laboratory who I had the opportunity to meet over the years. I really enjoyed the atmosphere and had many great conversations there.

Finally, I am extremely grateful for Aiko Yamada and my family.

# Contents

<b>1</b>	<b>Introduction</b>	<b>1</b>
1.1	Evolution of laser technology and high energy density physics . . . . .	1
1.1.1	Ultra-high intensity lasers and high energy density physics . . . . .	1
1.1.2	Basic laser parameters . . . . .	1
1.1.3	Motion of electrons in a relativistic regime . . . . .	3
1.2	Laser-matter interaction . . . . .	5
1.2.1	Interaction with overdense and underdense plasmas . . . . .	5
1.2.2	Interaction with cluster targets . . . . .	7
1.3	Ion acceleration . . . . .	8
1.3.1	Mechanisms of laser plasma ion acceleration . . . . .	8
1.3.2	Ion acceleration using cluster targets . . . . .	11
1.4	About this thesis . . . . .	14
1.4.1	Objectives . . . . .	14
1.4.2	Organization of the chapters . . . . .	14
<b>2</b>	<b>Interaction between a high-power laser and cluster medium</b>	<b>16</b>
2.1	Characteristics of cluster medium . . . . .	16
2.2	High energy ions from laser-irradiated cluster medium . . . . .	17
2.3	Characteristics of a single cluster expansion . . . . .	20
2.3.1	Cluster expansion into a vacuum . . . . .	20
2.3.2	Cluster expansion in the ambient gas . . . . .	30
2.3.3	Collisionless plasma boundary layer . . . . .	32
2.4	Summary . . . . .	33
<b>3</b>	<b>Shock characteristics in laser-cluster interaction</b>	<b>34</b>
3.1	Collisionless shocks due to the laser-matter interaction . . . . .	34
3.1.1	Collisionless shock formation and particle acceleration . . . . .	34
3.1.2	Schematic model of collisionless shock acceleration . . . . .	35
3.1.3	Theoretical model of collisionless shock . . . . .	37
3.1.4	Collisionless shock acceleration in 1D case . . . . .	41
3.2	Collisionless shocks in laser-irradiated cluster medium . . . . .	45
3.2.1	External collisionless shock . . . . .	45
3.2.2	Internal collisionless shock . . . . .	46

3.3	Summary . . . . .	47
<b>4</b>	<b>Structure and dynamics of the collisionless plasma boundary layer</b>	<b>49</b>
4.1	Overview . . . . .	49
4.2	Dynamics of boundary layer in between cluster and ambient gas . . . . .	51
4.2.1	Numerical modeling . . . . .	51
4.2.2	Overview of the dynamics of boundary layer . . . . .	55
4.2.3	Ion acceleration by nonlinear waves . . . . .	64
4.2.4	Formation of quasi-stationary kinetic equilibrium . . . . .	69
4.3	The effect of the ambient gas density on the transition dynamics of the boundary layer . . . . .	75
4.3.1	The structure of boundary layer for different ambient gas densities . . . . .	75
4.3.2	Density dependence for transition times . . . . .	80
4.3.3	Numerical investigation of transition time . . . . .	81
4.3.4	Maximum kinetic energy of the ambient gas ions . . . . .	85
4.4	Summary . . . . .	87
<b>5</b>	<b>Proton acceleration driven by hemispherically converging collisionless shock</b>	<b>90</b>
5.1	Overview . . . . .	90
5.2	Mechanisms for obtaining quasimonoenergetic protons . . . . .	92
5.2.1	Ion acceleration mechanisms (TNSA, RPA, BOA and CSA) . . . . .	92
5.2.2	Ion acceleration using cluster target . . . . .	94
5.3	Proton acceleration by intra-cluster collisionless shock ( $R=0.8 \mu\text{m}$ ) . . . . .	95
5.3.1	Numerical modeling . . . . .	95
5.3.2	Generation of quasimonoenergetic protons . . . . .	100
5.3.3	Effect of the magnetic field of the laser . . . . .	105
5.3.4	Dependence of laser intensity . . . . .	106
5.4	Dependence of the cluster size . . . . .	107
5.4.1	Proton acceleration for $R=0.6 \mu\text{m}$ . . . . .	107
5.4.2	Proton acceleration for $R=1.0 \mu\text{m}$ . . . . .	108
5.5	Density dependence / Effect of prepulse . . . . .	109
5.6	Summary . . . . .	110
<b>6</b>	<b>Conclusion</b>	<b>113</b>
6.1	Summary of the results . . . . .	113
6.1.1	Dynamics of boundary layer . . . . .	113
6.1.2	Monoenergetic protons reaching 300 MeV . . . . .	114
6.2	The meaning of this study . . . . .	116
6.3	Future work . . . . .	116

# Chapter 1

## Introduction

### 1.1 Evolution of laser technology and high energy density physics

#### 1.1.1 Ultra-high intensity lasers and high energy density physics

Recent evolution of a high-power laser technology enables us to create extreme state of matter, i.e., high-energy and high-density plasmas, by the irradiation of a high-power laser pulse to the matter. Figure 1.1 shows progress in laser peak intensity since the invention of the laser in 1960. Especially, due to the chirped pulse amplification (CPA) technology after 1985 [1], the peak intensity of the laser pulse exceeds  $10^{18}$  W/cm<sup>2</sup> and electron velocity reaches the relativistic region. Therefore, by the irradiation of a high-power laser pulse to the matter, the charge separation is induced in plasma and ultra-high intensity electric field ( $\sim$ TV/m) is produced in  $\sim$ femtosecond–picosecond time scale and  $\sim\mu\text{m}$  size area. This means that we can create high energy density astrophysical phenomena, such as a generation of collisionless shock produced by the supernova explosion, which is considered to be the origin of the high energy ( $\sim 10^{15}$  eV) cosmic ray, in laboratory conditions by the high-power laser irradiation to various types of targets. For example, formations of collisionless shocks [2–4] and associated particle acceleration, self-organization of electromagnetic field structures [5], magnetic field amplification by turbulence [6], formation of a scaled protostellar jet [7], and magnetic field generation via the Weibel instability [8] exhibit at various types of laser-irradiated plasmas.

#### 1.1.2 Basic laser parameters

Laser peak intensity is expressed by using the normalized amplitude of a laser  $a_0$ , which is defined as

## 1.1. EVOLUTION OF LASER TECHNOLOGY AND HIGH ENERGY DENSITY PHYSICS

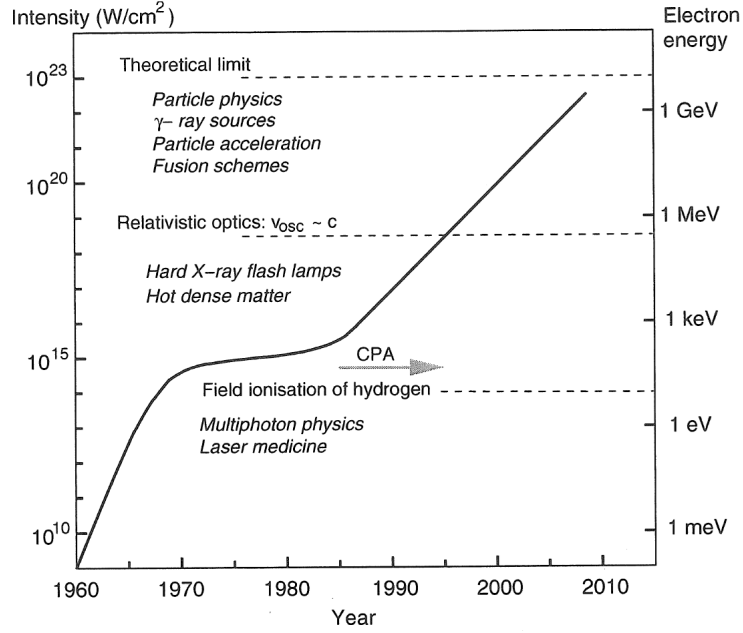


Figure 1.1: Laser technology progress for tabletop systems. The middle dash line represents the laser peak intensity of  $2.0 \times 10^{18} \text{ W cm}^{-2}$ , where the velocity of electron nearly reaches the light speed  $\sim c$ . Image is reprinted from P. Gibbon, “*Short Pulse Laser Interactions with Matter*”, Imperial College Press (2005), Fig. 1.1.

$$a_0 = \frac{eE_0}{m_e \omega_L c}, \quad (1.1)$$

where  $e$  is the elementary charge,  $E_0$  is the amplitude of the laser electric field,  $m_e$  is the electron mass,  $\omega_L$  is the laser frequency, and  $c$  is the light speed. Here, Eq. (1.1) is derived by  $m_e v_{max} / (m_e c)$ , where  $v_{max} = (E_0 / m_e \omega_L) \sin \omega_L t$  is the maximum electron velocity obtained by the oscillation of the laser electric field  $E = E_0 \cos \omega_L t$ . Namely,  $a_0 = 1$  means the maximum electron velocity  $v_{max}$  is close to the light speed  $c$ . The relation between the laser peak intensity  $I$  and the amplitude of the laser electric field  $E$  is represented as

$$I = \frac{1}{2} \varepsilon_0 c E_0^2, \quad (1.2)$$

where  $\varepsilon_0 = (4\pi)^{-1} c^{-2} \times 10^7 \text{ (F m}^{-1}\text{)}$  is permittivity of vacuum. From Eqs. (1.1) and (1.2),

$a_0$  is expressed by using the laser peak intensity  $I$  and the laser wavelength  $\lambda$  as follows:

$$a_0 = 8.55 \times 10^{-10} \{I(\text{Wcm}^{-2})\}^{\frac{1}{2}} \lambda(\mu\text{m}). \quad (1.3)$$

Namely, from Eq. (1.3), the motion of electrons becomes relativistic, i.e.,  $a_0 \sim 1$ , for a high-power laser with a peak intensity of  $I = 2.0 \times 10^{18} \text{ W cm}^{-2}$  and  $\lambda = 0.81 \mu\text{m}$ . As we discuss in Chapter 4 and 5, we assume high-power lasers with the peak intensity of  $I \sim 1.0 \times 10^{19} - 2.0 \times 10^{22} \text{ W cm}^{-2}$ , where corresponding  $a_0$  ranges roughly from 2 to 100, and the motion of electrons becomes relativistic. Therefore, in the following, we treat the motion of electrons in the *relativistic* regime ( $a_0 \geq 1$ ).

### 1.1.3 Motion of electrons in a relativistic regime

Motion equation of an electron in *cgs* Gauss unit is described as follows:

$$\frac{d\mathbf{p}}{dt} = e(\mathbf{E} + \frac{1}{c}\mathbf{v} \times \mathbf{B}). \quad (1.4)$$

Here,  $\mathbf{p} = \gamma_e m_e \mathbf{v}$  and  $\mathbf{v}$  are the momentum of electron and the velocity of electron, respectively, and  $\gamma_e = \{1 - (v/c)^2\}^{-\frac{1}{2}}$  is the Lorentz factor.  $\mathbf{E}$  and  $\mathbf{B}$  represent the laser electric field and the laser magnetic field, respectively. When we assume the laser propagates in the  $+y$  direction and the vector potential of the laser is represented as  $\mathbf{A} = (\delta a_0 \cos \phi, 0, (1 - \delta^2)^{\frac{1}{2}} a_0 \sin \phi)$ , from Eq. (1.4),  $(p_x, p_y, p_z)$  and  $(x, y, z)$  are derived as

$$\begin{cases} p_x = \delta a_0 \cos \phi \\ p_y = \frac{a_0^2}{4} [1 + (2\delta^2 - 1) \cos 2\phi] \\ p_z = (1 - \delta^2)^{\frac{1}{2}} \end{cases} \quad (1.5)$$

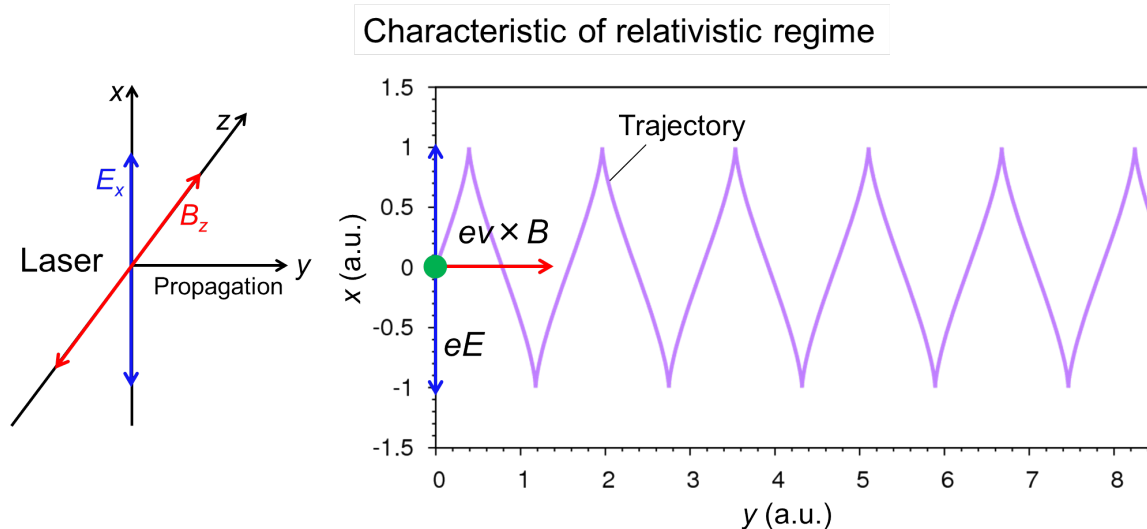


Figure 1.2: Electron trajectory by the action of the linearly polarized laser in the  $(x, y)$  plane. Laser propagates in the  $+y$  direction. The electron moves in the  $+y$  direction by the magnetic field component of the Lorentz force, i.e.,  $e\mathbf{v} \times \mathbf{B}$ , with oscillating in the  $x$  direction by the laser electric field  $\mathbf{E}$ .

$$\begin{cases} x = \delta a_0 \sin \phi \\ y = \frac{a_0^2}{4} \left[ \phi + \left( \delta^2 - \frac{1}{2} \right) \sin 2\phi \right] \\ z = -(1 - \delta^2)^{\frac{1}{2}} a_0 \cos \phi \end{cases} \quad (1.6)$$

Here,  $a_0$  is the normalized amplitude of a laser and  $\phi$  denotes  $\omega_L t - kr$ , where  $\omega_L$  is laser frequency and  $k$  is the wave number ( $=2\pi/\lambda$ ).  $\delta$  is determined by the laser polarization, i.e.,  $\delta = \pm 1$  for linearly polarized laser and  $\delta = \pm 1/\sqrt{2}$  for circularly polarized laser. In the case of  $a_0 \geq 1$ , the electron trajectory becomes so-called eight-figure motion. Figure 1.2 shows the motion of a single electron calculated by Eq. (1.6) in the  $(x, y)$  plane for  $\delta = \pm 1$  and  $a_0 = 1$ . The electron moves in the  $+y$  direction, which is the same as the laser propagation direction. As  $a_0$  becomes large, the relativistic effect, i.e., the magnetic field component of the Lorentz force  $e\mathbf{v} \times \mathbf{B}$  in Eq. (1.4), becomes dominant. As we discuss in Chapter 5, the electron's motion in the  $+y$  direction (in the same direction as the laser propagation) plays a role in the formation of an anisotropic intensity distribution of the electric field around the cluster.

## 1.2 Laser-matter interaction

### 1.2.1 Interaction with overdense and underdense plasmas

In the plasma, the laser electric field  $E$  and the laser magnetic field  $B$  satisfy the following Maxwell equation, which is described in *cgs* Gauss unit as

$$\nabla \times \mathbf{B} = \frac{4\pi}{c} \mathbf{j} + \frac{1}{c} \frac{\partial \mathbf{E}}{\partial t} \quad (1.7)$$

$$\nabla \times \mathbf{E} = -\frac{1}{c} \frac{\partial \mathbf{B}}{\partial t}, \quad (1.8)$$

where  $\mathbf{j}$  is the current. When we assume the electron is oscillated by the laser electric field in the  $x$  direction and the laser electric field  $\mathbf{E}$  is represented as

$$\mathbf{E} = E_0 \cos(kx - \omega_L t) \hat{\mathbf{x}}, \quad (1.9)$$

then, the current  $\mathbf{j}$  is derived as

$$\mathbf{j} = -n_e e v_x \hat{\mathbf{x}} = \frac{n_e e^2 E_0}{m_e \omega_L} \sin(kx - \omega_L t) \hat{\mathbf{x}}. \quad (1.10)$$

By using Eqs. (1.9) and (1.10), Eq. (1.7) becomes as follows:

$$\nabla \times \mathbf{B} = \frac{1}{c} \left( \omega_L - \frac{4\pi n_e e^2}{m_e \omega_L} \right) E_0 \sin(kx - \omega_L t) \hat{\mathbf{x}}. \quad (1.11)$$

When the following relation is satisfied, Eq. (1.11) has no solutions:

$$\omega_L - \frac{4\pi n_e e^2}{m_e \omega_L} = 0$$

$$\therefore \omega_L = \omega_p = \sqrt{\frac{4\pi n_e e^2}{m_e}} \sim 56.4 \times 10^3 \times \sqrt{n_e (\text{cm}^{-3})} \text{ (s}^{-1}\text{)}. \quad (1.12)$$

Namely, the laser field cannot propagate into the plasma for  $\omega_L = \omega_p$ . Here,  $\omega_p$  is a plasma frequency. Under the condition that the laser frequency  $\omega_L$  is larger than the plasma frequency  $\omega_p$ , i.e.,  $\omega_L > \omega_p$ , the Maxwell equation has the solution. Namely, the laser pulse can propagate into the plasma.

The frequency  $\omega_p$  is expressed as a function of the electron density of the plasma  $n_e$ . This means that when the density  $n_e$  satisfies the following relation,

$$n_e = n_c = \frac{m_e \omega_L^2}{4\pi n_e e^2} \sim 1.1 \times 10^{21} \times \frac{1}{\{\lambda (\mu\text{m})\}^2} \text{ (cm}^{-3}\text{)}, \quad (1.13)$$

the laser field cannot propagate into the plasma. Here, the density  $n_c$  is a cutoff density, where  $\lambda$  is the laser wavelength. For example, the density  $n_c$  is  $\sim 1.7 \times 10^{21} \text{ cm}^{-3}$  for  $\lambda = 0.81 \mu\text{m}$ . The plasma which satisfies the relation  $n_e < n_c$  for a given laser wavelength  $\lambda$  is called *underdense* plasma, while the plasma  $n_e > n_c$  for a given laser wavelength  $\lambda$  is called *overdense* plasma.

By taking the cross product of Eqs. (1.7) and (1.8), and utilizing the relation  $\nabla \times (\nabla \times \mathbf{E}) = \nabla(\nabla \cdot \mathbf{E}) - \nabla^2 \mathbf{E} = -\nabla^2 \mathbf{E}$ , we obtain the following *dispersion relation*:

$$\omega_L^2 = \omega_p^2 + c^2 k^2. \quad (1.14)$$

When the relation  $\omega_L > \omega_p$  is satisfied, Eq. (1.14) has a real root concerning  $k$  and the laser can propagate into the plasma. On the other hand, in the case of  $\omega_p > \omega_L$ , the laser electric field  $E$  is represented by

$$E = \text{Re}[E_0 \exp\{-i(kx - \omega_L t)\}] = E_0 \exp\left(-\frac{\sqrt{\omega_p^2 - \omega_L^2}}{c}x\right) \cos \omega_L t, \quad (1.15)$$

where the wave number  $k$  is calculated as  $i\sqrt{\omega_p^2 - \omega_L^2}/c$  by using Eq. (1.14). Eq. (1.15) indicates that the amplitude of the laser electric field, i.e.,  $E_0 \exp(-\sqrt{\omega_p^2 - \omega_L^2}/cx)$ , damps in proportion to the depth  $x$ . Then, the depth is defined as an electron skin depth  $\delta_e$ ,

$$\delta_e = \frac{c}{\sqrt{\omega_p^2 - \omega_L^2}}, \quad (1.16)$$

which means that the amplitude of the laser electric field becomes  $1/e$  during the propagation of the distance  $\delta_e$  into the overdense plasma. In the case of  $\omega_p \gg \omega_L$ , i.e., the electron density of the plasma is high, the skin depth  $\delta_e$  is approximated as

$$\delta_e \sim \frac{c}{\omega_p} \sim 53.2 \times 10^2 \times \{n_e(\text{cm}^{-3})\}^{-\frac{1}{2}} \text{ (m)}. \quad (1.17)$$

### 1.2.2 Interaction with cluster targets

Various targets, e.g., gas targets with the electron density of  $\sim 10^{19} \text{ cm}^{-3}$  and solid targets with the electron density of  $\sim 10^{23} \text{ cm}^{-3}$ , have been so far studied to create the high energy density state, e.g., astrophysical plasmas, in the laboratory conditions aiming at understanding the astrophysical phenomena including the generation of high energy particles. On the other hand, the interaction of cluster targets, composed of nano-micro meter size clusters and ambient gas, with intense laser pulses has been actively researched for over 20 years [9,10] because the cluster targets allow very efficient coupling with laser pulses compared with solid targets [11–13] even in the radiation dominant regime [14] due to high absorption rate of the laser energy. Here, cluster is a nano-micro meter size spherical object having a solid density. The pioneering experimental works in the 1990s of generating bright x-rays [15] and MeV-class multiply charged ions [16] from Coulomb exploding high-Z clusters, and fusion neutrons from Coulomb exploding deuterium clusters [17] have attracted wide attention. These are attributed to collective electron dynamics in individual clusters. On the other hand, the cluster targets act as efficient nonlinear media for the self-focusing of an incident laser pulse [18], leading to the formation of a self-guided plasma channel [19] and a plasma filament [20], which are closely

### 1.3. ION ACCELERATION

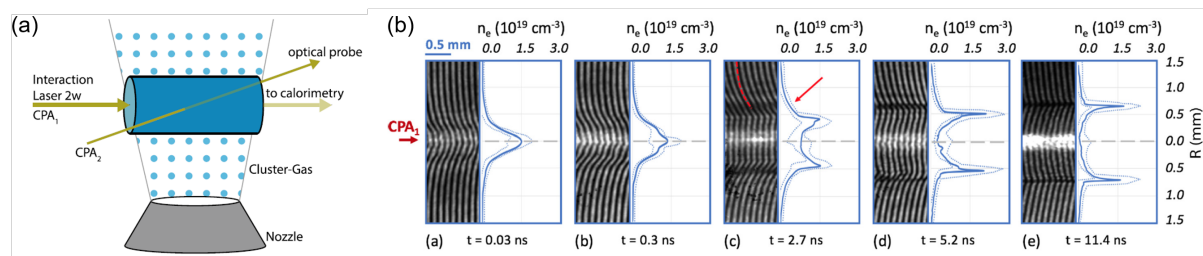


Figure 1.3: (a) Schematic view of experimental setup concerning the interaction between cluster target (Argon cluster and Argon gas) and a high power laser with a peak intensity of  $I \sim 10^{18}$  W/cm<sup>2</sup>. (b) Experimental results concerning the generation and propagation of a blast wave in a laser-irradiated cluster medium. Figures are reprinted from ref. [26], and Figures (a) and (b) correspond to Figures 1 and 2 in ref. [26].

connected with the recent remarkable studies including enhanced soft x-ray generation [21] and multi-MeV ion acceleration [22], high-charge sub-GeV electron acceleration [23], bright keV betatron x-rays [24], MeV-energy neutral atoms [25], and nonlocal electron transport in radiative blast wave [26].

Figure 1.3 shows latest experimental results concerning the generation of a blast wave [26]. In this experiment, due to the high-power laser irradiation with a peak intensity of  $I \sim 10^{18}$  W/cm<sup>2</sup> with a pulse duration of  $\tau \sim 1$  picosecond to the cluster target consisting of Argon cluster and ambient Argon gas [see Fig. 1.3(a)], the blast wave with  $\sim$ mm size is generated and propagate during  $\sim$ picosecond–nanosecond time scale [see Fig. 1.3(b)]. This is a typical example of *macro-scale structure* generated in laser-irradiated cluster target.

## 1.3 Ion acceleration

### 1.3.1 Mechanisms of laser plasma ion acceleration

In terms of applications concerning laser-matter interaction, we can obtain high energy (MeV/u–GeV/u) ions by utilizing the large electric field produced in the laser-irradiated matter. This ion acceleration scheme is called *laser plasma ion acceleration methods*. This scheme has a large advantage to the scheme using massive ion accelerator in terms of a large acceleration gradient. For example, LINAC (linear accelerator) at J-PARC (Japan Proton Accelerator Research Complex), which is one of the famous massive ion accelerator, attains 400 MeV protons with several hundred meters ( $\sim 250$  m), which leads to an accelerating gradient of  $\sim 1.6$  MeV/m. On the other hand, by the irradiation of the high-power laser to the matter, we can create 1 MeV protons with several dozen micrometers, which leads to an accelerating gradient of  $\sim 1 \times 10^5$  MeV/m. This indicates that the accelerating gradient of laser plasma ion acceleration methods is approximately  $10^5$  times larger than that of the massive ion accelerator. Therefore, laser plasma ion acceleration is expected to realize a tabletop ion accelerator, which is useful for medical

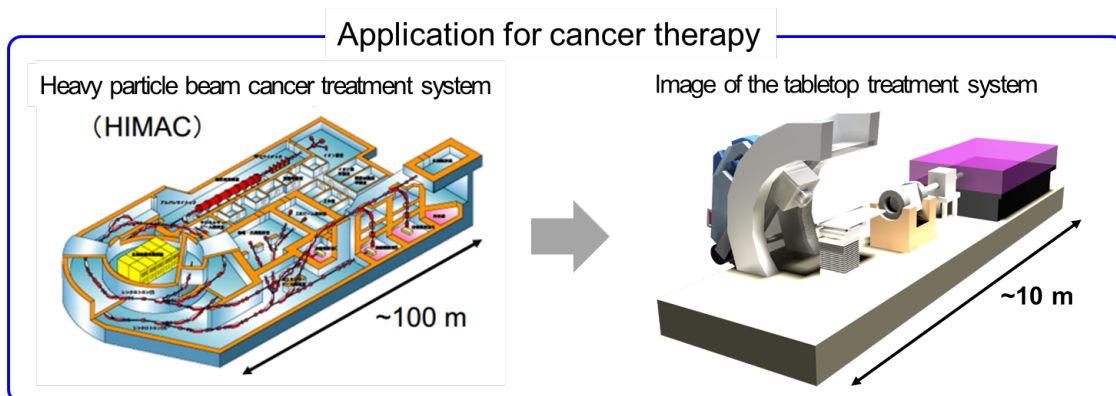


Figure 1.4: Schematic views of the heavy particle beam cancer treatment system (HIMAC), National Institute of Radiological Sciences (NIRS), QST (picture in the left) and the tabletop treatment system in the future (picture in the left). Images are offered from Doc. Yuji Fukuda, KPSI-QST.

application, such as a cancer therapy (see Fig. 1.4).

The recent advancements in both laser and target fabrication techniques have led to the enhancement of the accelerated proton cut-off energies close to 100 MeV [27–29]. However, the energy spectra of ions show a wide spread, which reduces the effective beam current to be utilized. In addition, lower angular divergence of accelerated ions and also higher repetition rates, which are technological issues using solid thin film targets, are requested for the wider applications of this scheme.

For medical applications, high energy ions exceeding 100 MeV with narrow energy spread are required. Several schemes have been so far proposed to explain experimental results and to explore further efficient acceleration. Figure 1.5(a) shows ion acceleration mechanisms which have been mainly studied in laser plasma ion acceleration fields. As shown in Fig. 1.5(a), mechanisms are divided into two main groups, i.e., opaque regime (solid density) and transparent regime (gas density).

In opaque regime, a target normal sheath acceleration (TNSA) [30–35] is one of the most famous ion acceleration mechanism. In TNSA mechanism, as shown in Fig. 1.6(a), by the irradiation of the high-power laser to the solid target, high energy electrons are ejected from the rear side of the target. Subsequently, a large electric field, i.e., a sheath electric field, is established at an interface between the rear side of the target and vacuum. Consequently, high energy ions are also ejected from the rear side of the target with a wide energy spread due to the large electric field. Considerable efforts have been made to obtain a narrow energy spectrum via the engineering of target structures [34, 35], however, the TNSA mechanism generally exhibits broad exponential energy spectra with wide angular divergence.

On the other hand, radiation pressure acceleration (RPA) [37–53] has been attracted wide attention. This is because the RPA mechanism has a potential to produce monoenergetic ions. In RPA mechanism, by the irradiation of an ultra-high power laser

### 1.3. ION ACCELERATION

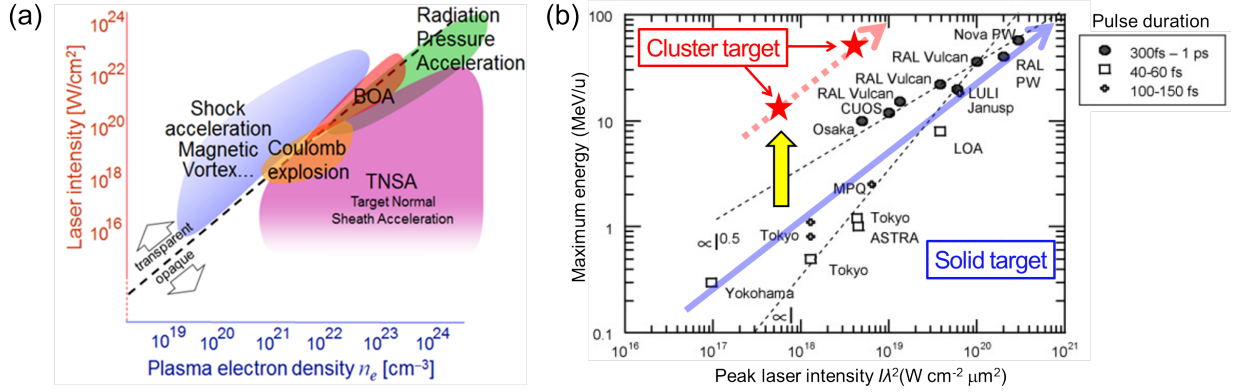


Figure 1.5: (a) Ion acceleration mechanisms which have been mainly studied in laser plasma ion acceleration fields. The graph is reprinted from P. Mackenna, EAAC (2015). (b) Experimental results concerning maximum ion energy per nucleon by laser plasma interaction. Red line shows the scaling of results using cluster targets [22, 63]. Blue lines show the scaling of results using solid targets (TNSA mechanism). The graph is reworked from Fig. 9(b) in ref. [64].

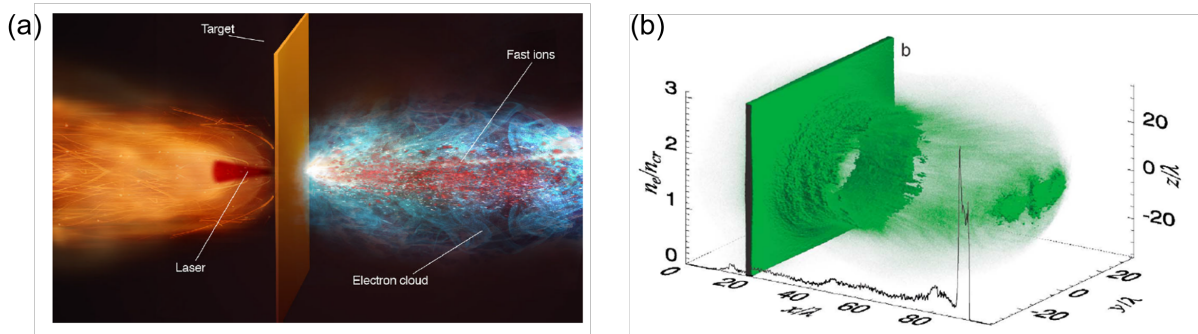


Figure 1.6: (a) Artist's view of a typical experiment on proton emission from laser-irradiated solid targets by target normal sheath acceleration (TNSA) mechanism. The picture is reprinted from Fig. 1 in ref. [36]. (b) The simulation result of the spatial density distribution of ions accelerated by radiation pressure acceleration (RPA) mechanism. The picture is reprinted from Fig. 1 in ref. [37].

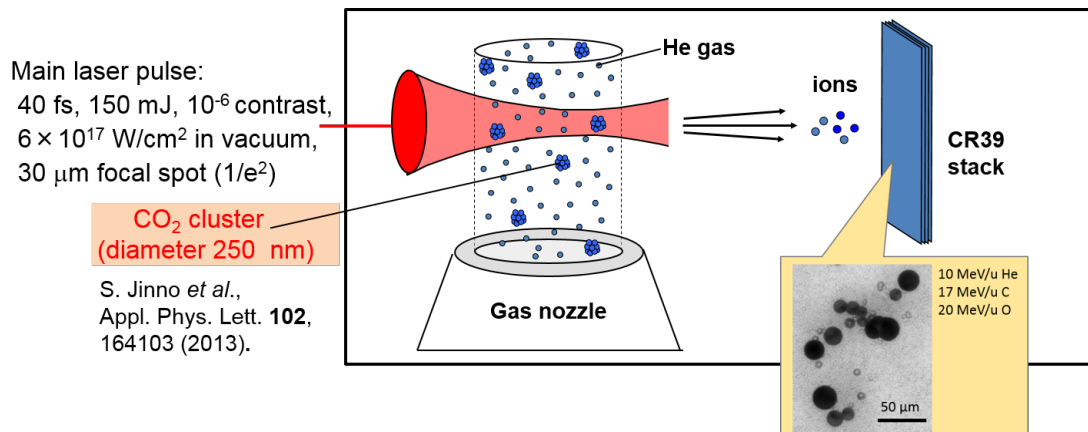


Figure 1.7: Experiment concerning laser-cluster target interaction. Cluster target consists of CO<sub>2</sub> cluster with a diameter of 250 nm and ambient He gas. High energy ions accelerated up to 10-20 MeV/u are obtained by using a short laser pulse with the peak intensity of  $6 \times 10^{17}$  W/cm<sup>2</sup> [22].

pulse with a peak intensity of  $\sim 10^{23} - 10^{24}$  W/cm<sup>-2</sup> to the ultra-thin solid target with a thickness of  $\sim 10$  nm, high energy ( $\sim$ GeV/u) monoenergetic ions are theoretically produced in the longitudinal (laser propagation) direction. Figure 1.6(b) shows the simulation results concerning the RPA mechanism in ref. [37]. In this simulation, high-energy and highly-directional protons reaching  $\sim$ GeV are obtained by using the ultra-high power laser with the peak intensity of  $I \sim 10^{23}$  W/cm<sup>2</sup>.

In transparent regime, recently, the break-out afterburner (BOA) [54], and the collisionless shock acceleration (CSA) [46, 55–62] have also been explored to obtain high energy ions with a low energy spread. In most of these cases, however, the results are either preliminary or require further confirmation. In these ion acceleration mechanisms, the solid target (TNSA, RPA) and/or gas target (BOA, CSA) are used. Namely, most of laser energy is not absorbed due to reflection (solid) or penetration (gas), leading to a low energy conversion efficiency.

### 1.3.2 Ion acceleration using cluster targets

On the other hand, cluster targets, which consists of cluster and ambient gas, show unique natures, i.e., having both gas and solid features, which leads to high absorption rate of laser energy. For example, from the experiment conducted at KPSI-QST, 10-20 MeV/u (2009) [22] and 50 MeV/u (2013) [63] ions have been observed by using cluster target. Fig. 1.7 shows the schematic view of the experiment concerning laser-cluster target interaction and experimental result [22]. Due to the interaction between the cluster target, which consists of CO<sub>2</sub> cluster with a diameter of  $\sim 250$  nm and He gas, and a high power laser pulse with a peak intensity of  $6 \times 10^{17}$  W/cm<sup>2</sup>, high energy ions with the maximum energy of 10-20 MeV/u have been obtained. The ion acceleration mechanism concerning these experiments is explained as *magnetic vortex model* [22, 65–68]. In this model, magnetic

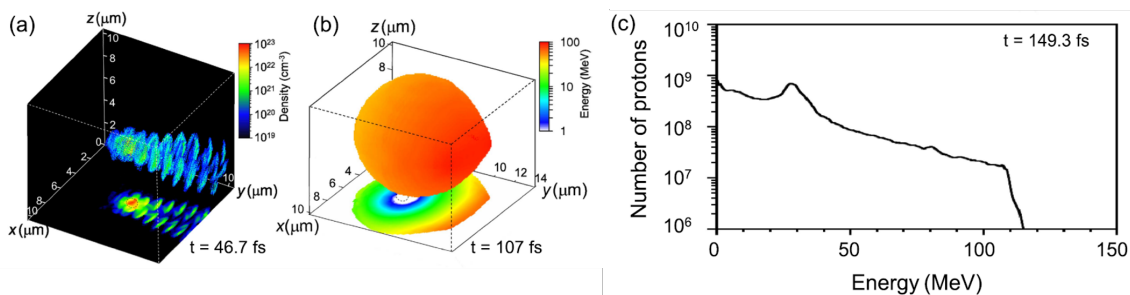


Figure 1.8: Simulation results concerning the interaction between a high power laser with the peak intensity of  $1.0 \times 10^{22}$  W/cm<sup>2</sup> and a hydrogen cluster with a diameter of  $1.2 \mu\text{m}$ . Here, a laser pulse is irradiated at  $t = 0$  and propagates in the  $+y$  direction. Spatial distributions of the density of cluster electrons (a) and the kinetic energy of cluster ions (b), and the energy spectrum of the cluster ions (c) are shown. Figures are reprinted from Figure 9 in ref. [70].

vortex, which is produced in the near critical density plasma, plays an important role in accelerating ions. In these experimental results [22, 63], cluster is considered to be fully melt by the prepulse of the laser and supply electrons to create the near critical density plasma [22].

Figure 1.5(b) shows the experimentally obtained maximum ion energy (per nucleon) by utilizing laser plasma interaction methods. Red line shows the scaling of results using cluster targets [22, 63] and blue lines show the scaling of results using solid targets by TNSA mechanism. These scaling lines indicate that in laser plasma ion acceleration methods, the obtained maximum ion energy increases in accordance with the peak laser intensity. However, the maximum ion energies obtained from using cluster targets are approximately 10 times larger than those obtained from using solid targets. Namely, by using cluster targets, we can obtain high acceleration efficiency compare to that obtained by using solid targets under the condition that lasers which show the same level of peak intensity is employed [see Fig. 1.5(b)].

As discussed in the former subsection, in laser plasma ion accelerations, the generation of ion beams with low bandwidth and low divergence at a high repetition rate still remains a critical issue. In addition, from a view point of practical applications, i.e., medical applications for cancer therapy, high-purity proton beams are quite advantageous. In experiments using thin foil targets, however, protons from surface contaminants along with the high- $Z$  component materials are accelerated together, making the production of impurity-free proton beams unrealistic.

Aiming at obtaining impurity-free protons, recently, a hydrogen cluster target, consisting of micro-meter size hydrogen clusters and ambient hydrogen gas, have been developed [69, 70]. When we focus on individual clusters in the cluster target, a laser-irradiated cluster undergoes a Coulomb explosion, which is the famous mechanism of the high energy ion generation [13, 16, 71–74]. The maximum ion energy by the Coulomb explosion is in proportion to the cluster size as we discuss in Chapter 2. Namely, when a

large hydrogen cluster undergoes the Coulomb explosion, high-energy and impurity-free protons can be obtained. Figure 1.8 shows simulation results concerning the interaction between a high-power laser with the peak intensity of  $1.0 \times 10^{22}$  W/cm<sup>2</sup> and a hydrogen cluster with a diameter of  $1.2 \mu\text{m}$  [70]. A laser pulse is irradiated at  $t = 0$  and propagates in the  $+y$  direction. As shown in Fig. 1.8(a), electrons removed from the cluster move forward (in the  $+y$  direction) due to the relativistic effect. Resultantly, the Coulomb explosion of the cluster is anisotropic and directed forward [see Fig. 1.8(b)]. Consequently, the maximum energy of protons reaches 117 MeV as shown in Fig. 1.8(c). These results indicate that high-energy and impurity-free protons exceeding 100 MeV, which has not been attained in the world at present, can be obtained via the Coulomb explosion, which is a micro-scale dynamics of the laser-irradiated cluster, due to the interaction between high-power laser and hydrogen cluster target.

## 1.4 About this thesis

### 1.4.1 Objectives

The present thesis aims at understanding of the structure and dynamics of a plasma collisionless boundary layer, which is universally formed at an interface between two distinct collisionless plasmas with different characteristics, based on the understanding of high energy density plasmas which are produced by an interaction between a high power laser and a cluster medium. This may help understand the origin of high energy cosmic rays because they are considered to be produced at the boundary layer, i.e., the interface between supernova and interstellar gas.

For this purpose, we regard an interface between the expansion front of the laser-irradiated cluster and ambient gas as the collisionless boundary layer, and reveal the structure and dynamics of the boundary layer through the interaction between the high-power laser and the cluster medium by performing two-dimensional (2D) particle-in-cell (PIC) simulations.

It is a critical issue to understand the acceleration mechanisms of the high energy ions not only for the academic significance, i.e., the acceleration mechanism of high energy cosmic rays, but also for medical applications. In order to utilize high energy density plasmas produced by the high-power laser irradiation to the cluster medium for medical applications, we also perform three-dimensional (3D) PIC simulations concerning the interaction between the high-power laser and a hydrogen cluster medium and investigate the production of high quality protons which are useful for practical applications including proton therapy for cancer treatment.

### 1.4.2 Organization of the chapters

The outline of the study and its chapters are given below.

In Chapter 2, we introduce basic characteristics which are obtained by the interaction between a high-power laser and cluster medium. Firstly, we present the characteristics of the cluster medium as a target of a high power laser and important experimental observations. Secondly, we introduce the dynamics of the laser-irradiated cluster in vacuum. The new point of our study is that we investigate the cluster expansion in the presence of the ambient gas. The interface between the cluster expansion front and the surface of the ambient gas is regarded as a boundary layer. We discuss the characteristics of the boundary layer and the similarity between the cluster expansion in the ambient gas and supernova explosion in the interstellar gas.

In Chapter 3, we present the nature of electrostatic collisionless shock launched in the laser-irradiated plasma. Collisionless shock acceleration (CSA) is widely studied because the mechanism shows a promising way to obtain quasimonoenergetic ions, which is applicable to medical applications, e.g., cancer therapy. In the laser-irradiated cluster medium, two kinds of collisionless shocks are produced. We introduce the formation process and ion acceleration mechanisms of these two shocks, i.e., the external collisionless

shock and the internal collisionless shock.

In Chapter 4, we focus on the structure and dynamics of the contact region, where the cluster expansion front and the compressed surface of the ambient gas interact with each other. From a viewpoint that the region is characterized as the boundary layer, we classified the dynamics of the boundary layer into three successive phases and investigated the acceleration mechanisms of the ambient gas ions. We also introduced the theoretical model to understand the transition time from the first phase to the second phase.

In Chapter 5, we propose a new approach for producing a quasimonoenergetic proton bunch based on the use of hemispherically converging collisionless shock created in laser-cluster interactions at a relativistically induced transparency (RIT) regime. Our results suggest that we can obtain high energy ( $\sim 300$  MeV) quasimonoenergetic ( $\delta E/E \sim 10\%$ ) protons, which are applicable to medical applications, by using currently available laser system. The finite ranges of parameters with threshold values concerning the peak intensity of laser and the cluster size are also discussed.

Finally, conclusion is given in Chapter 6.

# Chapter 2

## Interaction between a high-power laser and cluster medium

### 2.1 Characteristics of cluster medium

A cluster is a spherical dense object, which consists of a sub-micron size of agglomerated molecules via Van der Waals' forces, e.g., frozen carbon dioxide. The interaction of a cluster target, composed of nano-micro meter size clusters, with intense laser pulses has been actively researched for over 20 years because the cluster target allows very efficient coupling with laser pulses compared to solid targets [11,12]. The pioneering experimental works of producing high energy electrons and ions [16, 75–78], generating bright x-rays [79,80], high-harmonics [81,82] and fusion neutrons from Coulomb exploding deuterium clusters [17] have attracted wide attention. These are attributed to collective electron dynamics in individual clusters.

On the other hand, the cluster targets act as efficient nonlinear media. In real experimental conditions, cluster targets include ambient gas [83]. Namely, not only clusters but also ambient gas surrounding the clusters is considered to play an important role in regulating the dynamics in the laser-irradiated cluster target. For instance, the ambient gas with a density of  $\sim 10^{19} \text{ cm}^{-3}$  in the cluster targets [84–86] regulates the self-focusing of an incident laser pulse [18, 19], leading to the formation of a long plasma filament [20] and a self-guided plasma channel [87], which are responsible for cylindrically symmetric blast wave generation [26, 88, 89], enhanced electron charge in electron acceleration [23, 90], enhanced betatron x-ray radiation [91], MeV-energy neutral atoms [25], and enhanced ion acceleration [22] via a magnetic vortex [65–68].

The interaction between the cluster and a high-power laser has been numerically studied using a hydrodynamical model approach [71, 72], Molecular Dynamics (MD) approach [92–94] and particle-in-cell (PIC) approach [13, 73, 74, 95–98].

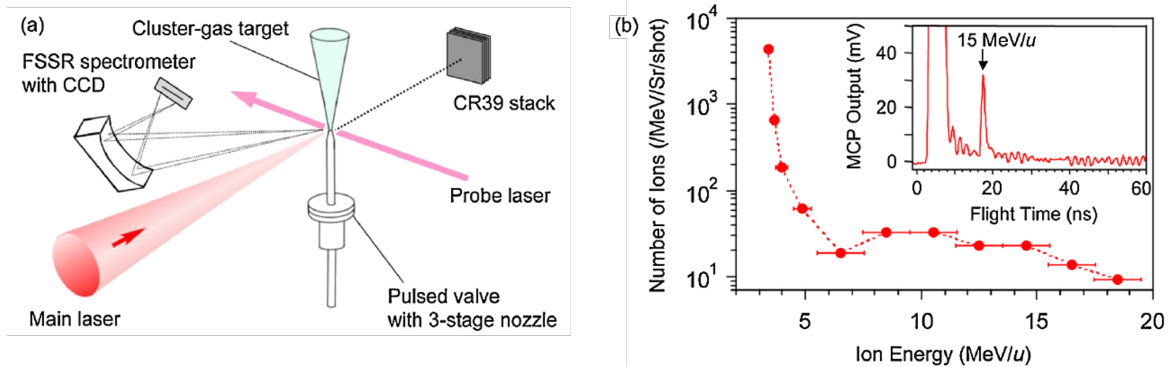


Figure 2.1: Experiment concerning laser-cluster target interaction. Cluster target consists of  $\text{CO}_2$  cluster with a diameter of 250 nm [110] and ambient He gas. High energy ions accelerated up to 10-20 MeV/u are obtained by the irradiation of a short laser pulse with the peak intensity of  $6 \times 10^{17} \text{ W/cm}^2$  to the cluster target [22].

## 2.2 High energy ions from laser-irradiated cluster medium

Laser plasma ion acceleration is characterized by a very large accelerating electric field gradient and a short pulse length and represents one of the most active areas of research over the past decade [36, 99] because accelerated MeV/u-class ion beams have unique properties, such as ultrashort duration, high brilliance, and low emittance, that enable their use in a broad range of applications, including proton radiography [100], hadron therapy [101–103], nuclear science [104, 105], fast-ignition [106, 107], isochoric heating of matter [108], and radiation-induced processes in matter [109].

In terms of the production of high energy ions, cluster targets have an advantage compare to solid targets. In experiments using cluster targets, high energy ions up to 10-20 MeV/u [22] and 50 MeV/u [63] are obtained. Figure 2.1 shows the experimental result concerning the production of high energy ions using cluster target ( $\text{CO}_2$  clusters with the size of  $\sim 250 \text{ nm}$  [110] and ambient He gas), conducted at KPSI-QST in 2009 [22]. In this experiment, 10-20 MeV/u ions ( $\text{C}^{6+}$ ,  $\text{O}^{8+}$  and  $\text{He}^{2+}$ ) have been obtained by an irradiation of a high-power laser pulse with a peak intensity of  $I \sim 6.0 \times 10^{17} \text{ W/cm}^2$  to the cluster target. The maximum ion energy is approximately 10 times larger than that obtained by using solid target with the same class of the laser system ( $I \sim 10^{17} \text{ W/cm}^2$ ) as discussed in Fig. 1.5(b).

In this scheme, a magnetic vortex [65–68], which is formed in the near critical density plasma, is considered to play an important role in accelerating ions. Figure 2.2(a) shows the schematic view of magnetic vortex acceleration of ions. As shown in Fig. 2.2(a), the strong magnetic vortex is formed around the interface between the plasma and the vacuum, where the energy of the laser pulse is fully absorbed by the near critical density plasma. Then, the energy of the magnetic vortex is converted into the energy of the

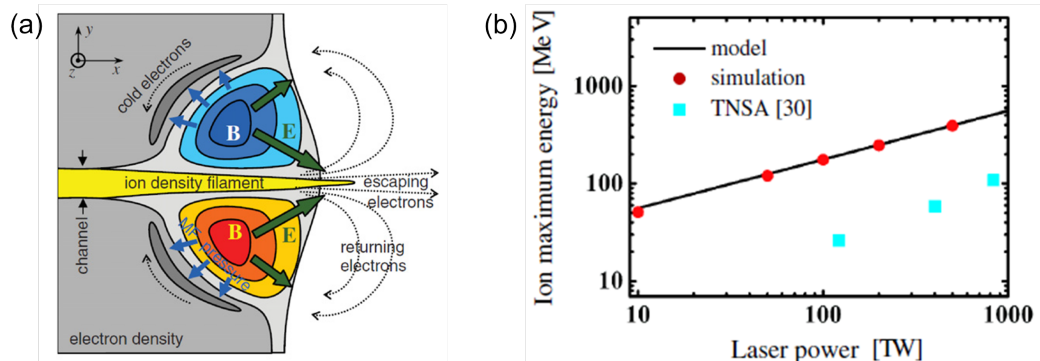


Figure 2.2: (a)The schematic view of magnetic vortex acceleration of ions. The picture is reprinted from Fig. 1 in ref. [67]. (b)Energy scaling for the magnetic vortex acceleration. The solid line shows the maximum ion energy predicted by the theoretical model concerning the magnetic vortex acceleration introduced by [68]. The blue squares are for ion acceleration using solid targets, where TNSA model is applied. The graph is reprinted from Fig. 4 in ref. [68].

electrostatic field, which accelerates ions. Figure 2.2(b) shows energy scaling for the magnetic vortex acceleration. The solid line shows the maximum ion energy predicted by the theoretical model concerning the magnetic vortex acceleration introduced by [68]. The blue squares are for ion acceleration using solid targets, where TNSA model is applied. As seen in Figure 2.2(b), the magnetic vortex mechanism has large acceleration efficiency compared to the TNSA mechanism using a solid target. However, the condition where this acceleration mechanism effectively works is hardly reproducible and hardly controlled in the real experimental conditions. This is because the optimal plasma density required for the generation of the magnetic vortex, which is  $\sim 10$  times higher than the general gas density, is too high.

In the experimental results [22, 63], on the other hand, clusters are considered to produce such near critical density plasma because clusters are melt by the prepulse of the laser and works as an electron source. Namely, the cluster target becomes near critical density plasma when the main pulse of the laser reaches the target. As a result, the magnetic vortex acceleration is considered to take place. It is noted that in this acceleration mechanism, the characteristics of cluster, e.g., Coulomb explosion, are not considered and cluster is considered to work only for the electron source.

On the other hand, in the experiment conducted at KPSI-QST in 2013, high energy ambient gas ions accelerated up to 1.6 MeV/u have been obtained [111]. Figure 2.3 shows the experimental result concerning the production of high energy ions using cluster target ( $\text{CO}_2$  clusters with the size of  $\sim 250$  nm [110] and ambient  $\text{H}_2$  gas) and a high power laser with the peak intensity of  $I = 1.0 \times 10^{19}$  W/cm<sup>2</sup>, conducted at KPSI-QST in 2013 [111]. In this experiment, cluster ions ( $\text{C}^{6+}$ ,  $\text{O}^{8+}$ ), which are accelerated up to 1.1 MeV/u, and ambient gas ions ( $\text{H}^+$ ), which are accelerated up to 1.6 MeV/u, are successfully detected separately by the magnet [see Fig. 2.3(a)]. As shown in Fig. 2.3(b), resulting energy

## 2.2. HIGH ENERGY IONS FROM LASER-IRRADIATED CLUSTER MEDIUM

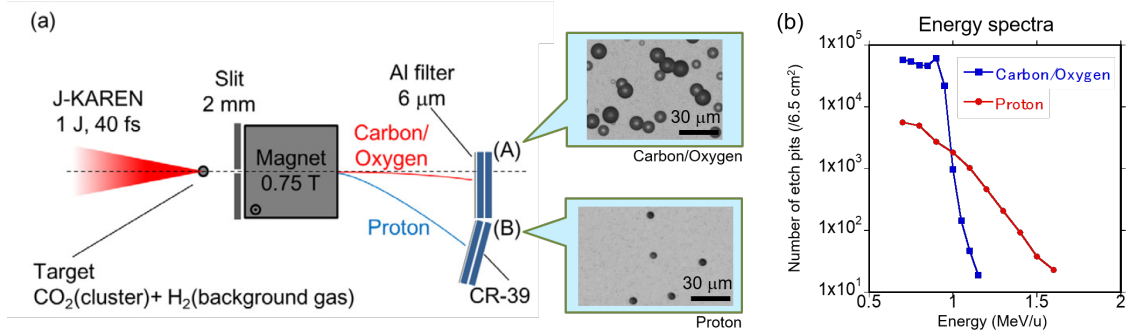


Figure 2.3: Experiment concerning Laser-cluster medium interaction. Cluster medium consists of CO<sub>2</sub> cluster with a diameter of 250 nm [110] and ambient H<sub>2</sub> gas. High energy ions accelerated up to 1.6 MeV/u (H<sup>+</sup>) and 1.1 MeV/u (C<sup>6+</sup>/O<sup>8+</sup>) are obtained by using a short laser pulse with the peak intensity of  $1 \times 10^{19}$  W/cm<sup>2</sup> [111].

spectra of ions shows different characteristics, i.e., sharp decrease around the maximum energy for cluster ions (C<sup>6+</sup>, O<sup>8+</sup>) and gentle decrease from the low energy area to high energy area for ambient gas ions (H<sup>+</sup>). Interestingly, the maximum energy per nucleon of ambient gas ions is larger than that of cluster ions.

This experimental result suggests that cluster ions and ambient gas ions are accelerated by the different acceleration mechanism. Moreover, the shape of the energy spectrum for cluster ions exhibits the characteristics of the Coulomb explosion of the cluster, indicating that clusters are considered to undergo the Coulomb explosion [Fig. 2.3(b)]. According to ref. [111], high energy ambient gas ions have not been obtained in the absence of the cluster. Namely, these experimental results suggest that the cluster plays an role in ion acceleration at the interface between the cluster and the ambient gas. From this viewpoint, we discuss the ion acceleration mechanisms by studying the structure and dynamics of the interface in the laser-irradiated cluster medium in Chapter 4.

## 2.3 Characteristics of a single cluster expansion

### 2.3.1 Cluster expansion into a vacuum

#### *Classification of cluster expansion dynamics*

Due to the irradiation of the laser pulse to the cluster, electrons of the cluster are stripped from their host cluster. Consequently, the positively charged cluster expands by the Coulomb repulsive force. This is a *Coulomb explosion* of a cluster.

However, the Coulomb explosion of the cluster strictly exhibits different characteristics depending on the relation between the cluster radius  $a$ , the electron skin depth  $\delta_e$  and the electron excursion length  $\xi_e$  [13]. Figure 2.4 shows the laser-irradiated cluster expansion models, which are categorized by the relation between  $a$ ,  $\delta_e$  and  $\xi_e$ .

*Case (i):*  $\xi_e \ll a, \delta_e$

When the excursion length  $\xi_e$  is much smaller than the cluster radius  $a$  and the skin depth  $\delta_e$ , electrons oscillated by the laser electric field exist around the cluster surface due to the strong Coulomb attractive force. In this case, as shown in Fig. 2.4(i), the cluster expands hydrodynamically with a velocity of  $c_s$ , where  $c_s$  is the sound velocity. The typical expansion time of the cluster, i.e.,  $a/c_s$ , is  $\sim$ picosecond–nanosecond, and the kinetic energy of cluster ions reaches  $\sim$ KeV/u.

*Case (ii):*  $\delta_e < a \sim \xi_e$

On the other hand, when the skin depth  $\delta_e$  is smaller than the cluster radius  $a$  and the excursion length  $\xi_e$  is comparable to the cluster radius  $a$ , the laser fields only interact with the peripheral region of the cluster. Consequently, as shown in Fig. 2.4(ii), the peripheral region of the cluster undergoes the Coulomb explosion, while the cluster core expands hydrodynamically.

*Case (iii):*  $a, \delta_e \ll \xi_e$

Finally, when the excursion length  $\xi_e$  is much higher than the cluster radius  $a$  and the skin depth  $\delta_e$ , as shown in Fig. 2.4(iii), all electrons of the cluster are fully stripped from their host cluster and the cluster undergoes a pure Coulomb explosion due to the Coulomb repulsive force of cluster ions. The typical expansion time of the cluster is  $\sim$ femtosecond, and the kinetic energy of ions reaches  $\sim$ several tens of MeV/u.

The typical energy spectra which correspond to three (i), (ii) and (iii) cases in Fig. 2.4 are shown in Fig. 2.5. In case (i), the spectrum shows the sharp decrease from low energy area to high energy area. Number of particles per energy  $dN/dE$  is proportional to  $\sqrt{E} \exp(-E)$  as shown in Fig. 2.5(i). In case (iii), as shown in Fig. 2.5(iii), the spectrum has a plateau structure from low energy area to high energy area and the cutoff structure around the maximum energy. Number of particles is proportional to  $\sqrt{E}$ . In case (ii), the spectrum has both (i) and (ii) features. Namely, the sharp decrease around low energy area, and the plateau and cutoff structure around high energy area.

### 2.3. CHARACTERISTICS OF A SINGLE CLUSTER EXPANSION

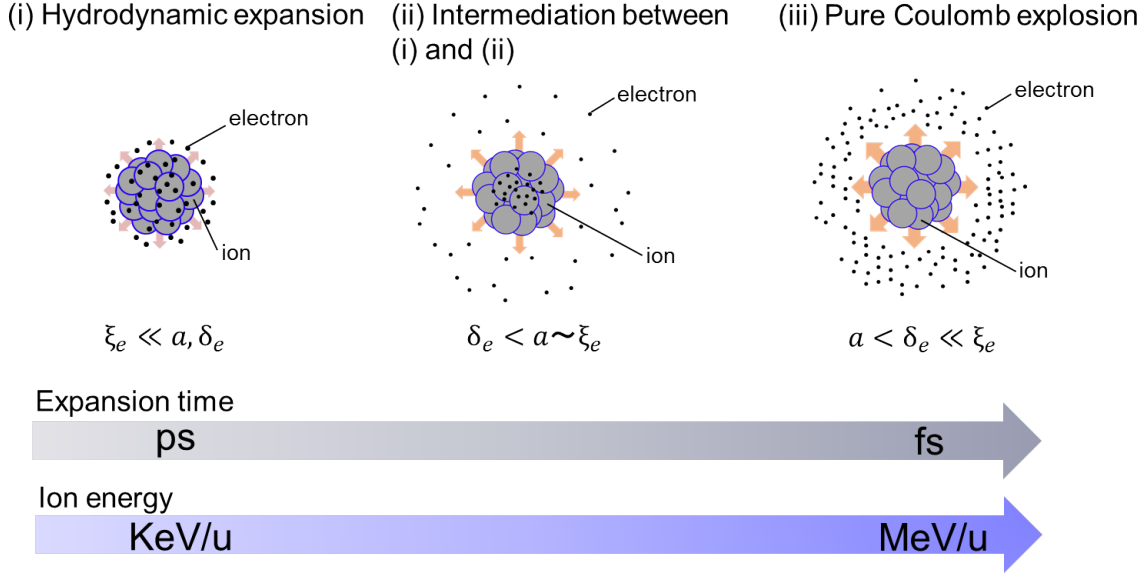


Figure 2.4: Cluster expansion models categorized by the relations between the cluster radius  $a$ , the electron skin depth  $\delta_e$  and the electron excursion length  $\xi_e$ . (i) Cluster expands hydrodynamically under the condition of  $\xi_e \ll a, \delta_e$ . (ii) The peripheral region of the cluster undergoes the Coulomb explosion and the core region of the cluster expands hydrodynamically under the condition of  $\delta_e < a \sim \xi_e$ . (iii) Cluster undergoes the pure Coulomb explosion under the condition of  $a < \delta_e \ll \xi_e$ .

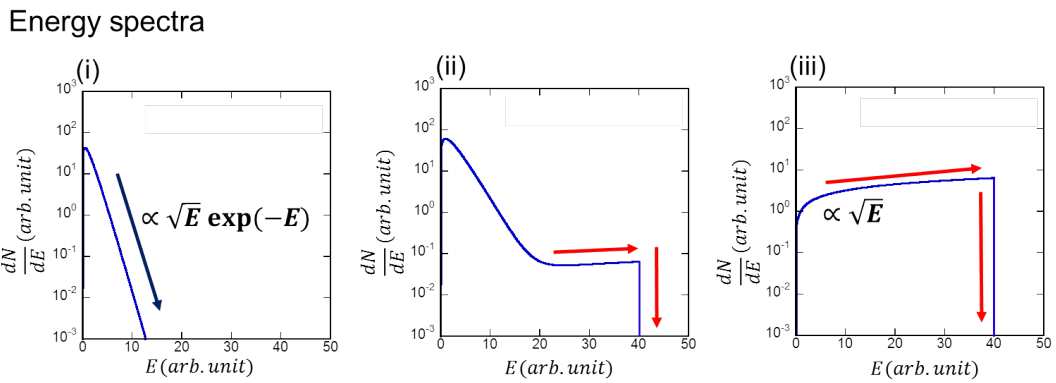


Figure 2.5: The typical energy spectra which corresponds to three (i), (ii) and (iii) cases in Fig. 2.4.

***Maximum energy of cluster ions***

Here, we consider the maximum energy of Coulomb-exploded cluster ions in case (iii), i.e., pure Coulomb explosion. In the pure Coulomb explosion model, the intensity of the electric field created both in the inside and outside the cluster after all electrons of the cluster are fully stripped from their host cluster depends on the dimension. From Gauss' law, the electric field as a function of the distance  $r$  from the cluster center is described as follows:

$$E_{2D}(r) = \begin{cases} \frac{Zn_i e}{2\varepsilon_0} r & 0 \leq r \leq R_0 \\ \frac{R_0^2 Zn_i e}{2\varepsilon_0} \frac{1}{r} & R_0 \leq r \end{cases} \quad (2.1)$$

$$E_{3D}(r) = \begin{cases} \frac{Zn_i e}{3\varepsilon_0} r & 0 \leq r \leq R_0 \\ \frac{R_0^3 Zn_i e}{3\varepsilon_0} \frac{1}{r^2} & R_0 \leq r \end{cases} \quad (2.2)$$

Here,  $E_{2D}(r)$  and  $E_{3D}(r)$  are in two-dimensional (2D, cylindrical rod) and three-dimensional (3D, spherical cluster) cases, respectively, and are shown as a function of  $r$  in Fig. 2.6.  $Z$  is the ion charge state,  $n_i$  is the ion density,  $e$  is the elementary charge, and  $\varepsilon_0$  is the permittivity of free space.

*(1) 2D case:*

The ion initially located at  $r = R_0$  finally obtains the maximum energy in all cluster ions. Then, the kinetic energy of the ion  $K(r)$  is calculated as follows:

$$K(r) = \int_{R_0}^r ZeE_{2D}(r)dr = \left[ \frac{Z^2 n_i e^2 R_0^2}{2\varepsilon_0} \log r \right]_{R_0}^r = \frac{Z^2 n_i e^2 R_0^2}{2\varepsilon_0} \log \frac{r}{R_0}. \quad (2.3)$$

Namely, the kinetic energy of ions  $K(r)$  shows a logarithmic divergence in 2D case.

*(2) 3D case:*

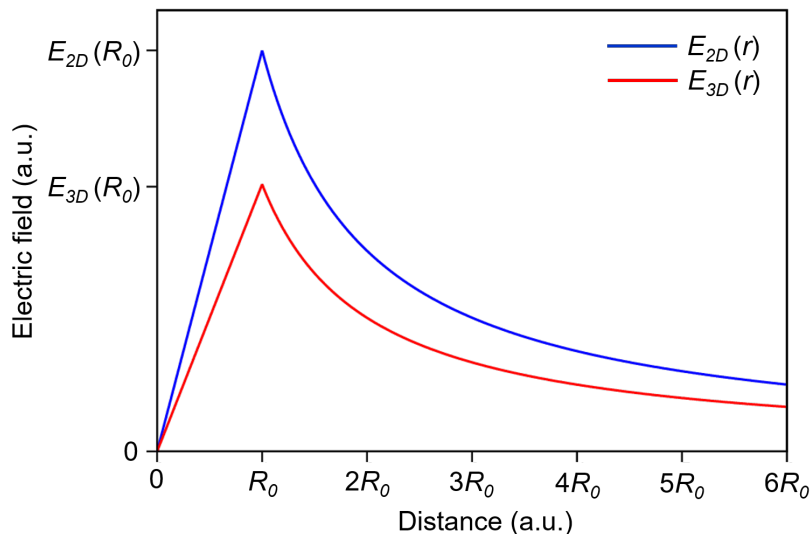


Figure 2.6: Electric field  $E_{2D}(r)$  (in 2D case, blue line) and  $E_{3D}(r)$  (in 3D case, red line) as a function of the distance  $r$  from the cluster center at  $t = 0$  fs.

In the 3D case, the kinetic energy of the ion  $K(r)$ , which is initially located at  $r = R_0$ , is calculated as

$$K(r) = \int_{R_0}^r qE_{3D}(r)dr = \left[ -\frac{Z^2 n_i e^2 R_0^3}{3\epsilon_0} \frac{1}{r} \right]_{R_0}^r = \frac{Z^2 n_i e^2 R_0^3}{3\epsilon_0} \left( \frac{1}{R_0} - \frac{1}{r} \right). \quad (2.4)$$

In the condition of  $r \gg R_0$ , the energy  $K(r)$  is approximated as

$$K(r) = \frac{Z^2 n_i e^2 R_0^2}{3\epsilon_0} = 301 \times Z^2 \left\{ \frac{n_i (\text{cm}^{-3})}{5 \times 10^{22} (\text{cm}^{-3})} \right\} \{R_0 (\mu\text{m})\}^2 (\text{MeV}). \quad (2.5)$$

For example, when a hydrogen cluster ( $Z=1$ ) with an ion density of  $n_i=4.6 \times 10^{22} \text{ (cm}^{-3}\text{)}$ , with a radius of  $1.0 \mu\text{m}$  undergoes the pure Coulomb explosion, from Eq. (2.5), the maximum ion energy obtained from the Coulomb explosion is approximately 277 (MeV). This result indicates that the kinetic energy of ions  $K(r)$  converges to a constant value in 3D case, while that in 2D case shows a logarithmic divergence.

### ***Cluster expansion into vacuum (2D simulation)***

Here, we show the expansion dynamics of the high-power laser irradiated cluster

### 2.3. CHARACTERISTICS OF A SINGLE CLUSTER EXPANSION

Table 2.1: System parameters

species	values or conditions
$x$	$-12.8 \leq x \leq 12.8 \mu\text{m}$
$y$	$-12.8 \leq y \leq 12.8 \mu\text{m}$
Mesh numbers $N_x$	2560
Mesh numbers $N_y$	2560
Grid size $\Delta_x$	10 nm
Grid size $\Delta_y$	10 nm
Time step $\Delta t$	$6.67 \times 10^{-18}$ fs
Boundary conditions	transparent in $x$ and $y$ directions for both particles and fields

into the vacuum by the 2D simulation using EPIC3D [112]. The schematic view of the simulation system is shown in Fig. 4.1(1) (Chapter 4). Simulation parameters are shown in Table 2.1 (system parameters), Table 2.2 (target parameters) and Table 2.3 (laser parameters).

A single carbon cluster with a radius of  $a = 125$  nm, with an electron density of  $n_e^{cl} = 3.8 \times 10^{23} \text{ cm}^{-3} (= 227n_c)$ , where  $n_c$  is the critical density of the plasma corresponding to the laser wavelength  $\lambda = 810$  nm, is employed. The initial cluster radius  $a$  is greater than the collisionless electron skin depth  $\delta_e = 11.6$  nm, which is defined by  $\delta_e = c/\omega_p$ , where  $c$  is the speed of light and  $\omega_p = \sqrt{4\pi e^2 n_e / \gamma m_e}$  (the Lorentz factor  $\gamma$  is defined by  $\gamma = \sqrt{1 + a_0^2/2}$  for the linearly polarized laser pulse) is a relativistic plasma frequency. Transparent boundary conditions are employed for the fields and the particles in the  $x$  and  $y$  directions. The number of PIC particles representing the carbon cluster is 2,453,000. The simulation box size is  $L_x \times L_y = 25.60 \times 25.60 \mu\text{m}$  containing  $2560 \times 2560$  cells. The cluster is located at the center of the box at  $(x, y) = (0, 0)$ .

A linearly polarized laser pulse in the  $x$  direction with a pulse duration (FWHM)  $\tau = 33$  fs is generated from an antenna located at  $y = -12.78 \mu\text{m}$  and propagates in the  $+y$  direction. Here, we assume that the laser is the plane wave in both  $x$  and  $z$  directions. The peak intensity of the laser pulse is set to  $1.0 \times 10^{19} \text{ W/cm}^2$ , which corresponds to the normalized amplitude  $a_0 = 2.19$ , where  $a_0 = eE_0/m_e\omega_L c$ . The laser pulse is irradiated from the antenna at  $t = 0$  fs. The pulse peak passes through the center of the cluster at  $t = 86.7$  fs. For simplicity of analysis, a fully ionized plasma is employed as the initial condition because the laser pulse electric field is strong enough to generate  $\text{C}^{6+}$  [113]. Moreover, the plasma is treated as collisionless since temperatures of both ions and electrons are enough high.

Figure 2.7 shows the time histories of normalized field energy (green line), electron energy (blue line), and ion energy (red line). The peak intensity of a laser pulse reaches

### 2.3. CHARACTERISTICS OF A SINGLE CLUSTER EXPANSION

---

Table 2.2: Cluster parameters

species	values
Cluster species	Carbon
Cluster radius	125nm
Cluster ion density	$6.3 \times 10^{22} \text{ cm}^{-3}$
Cluster electron density	$3.8 \times 10^{23} \text{ cm}^{-3}$ (fully ionized at the initial condition)
Particle numbers (Cluster ions)	2,453,000 (5,00 per cell of cluster)

Table 2.3: Laser parameters

species	values
Laser type	Gaussian pulse (plane wave in the $x$ and $z$ directions)
Peak intensity	$1.0 \times 10^{19} \text{ W cm}^{-2}$
Normalized amplitude	$a_0 = 2.19$
Wavelength	$0.81 \mu\text{m}$
Critical density	$1.7 \times 10^{21} \text{ cm}^{-3}$
Pulse width	33 fs (Full Width at Half Maximum)
Antenna position	$-12.78 \mu\text{m}$
Polarization	Linearly polarized (P)
Propagation	$+y$ direction
Electric field	$x$ direction
Magnetic field	$z$ direction

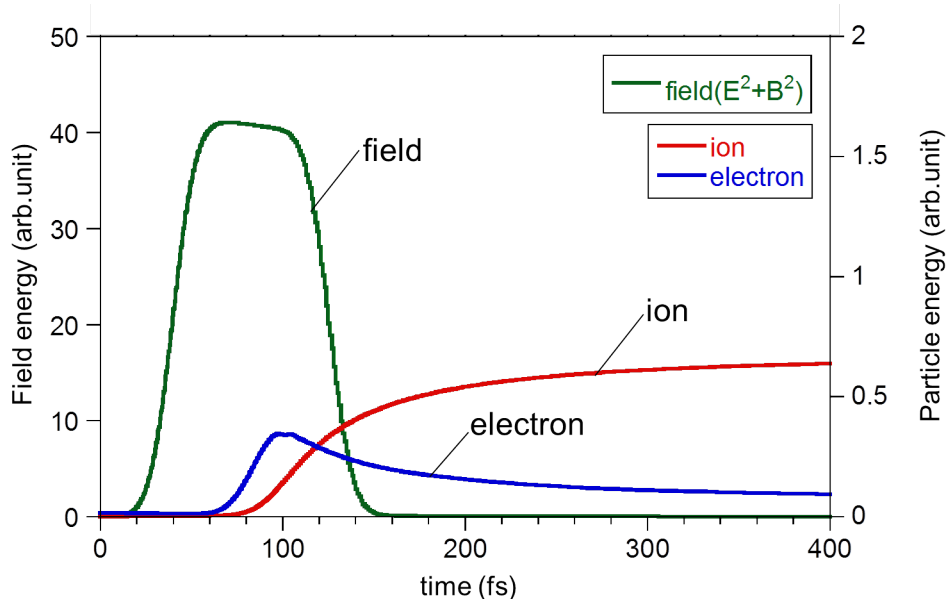


Figure 2.7: The time history of normalized field energy (green line), electron (blue line) and ion (red line) kinetic energies.

the cluster center at  $t = 86.7$  fs. As shown in Fig. 2.7, the laser energy is absorbed first by electrons around  $60 \leq t \leq 100$  fs, and then the ion energy gradually increases around  $80 \leq t$  [13]. The laser pulse goes out from the simulation box at around  $t = 150$  fs. That is, after  $t = 150$  fs, there is no supply of laser energy into the system. In this simulation, the 1.8 percent of input laser energy is absorbed by the cluster.

Figures 2.8(a)-2.8(h) show 2D images of the charge density distributions of cluster ions ( $C^{6+}$ ) and electrons. In an early stage of the interaction when the pulse peak of the laser reaches the cluster, since the cluster radius  $r = 125$  nm is greater than the electron skin depth  $\delta_e = 11.6$  nm, the laser fields cannot fully penetrate into the cluster, but interact only with the peripheral region of the cluster and stripped off electrons of this region, while most of electrons at the cluster core region remains unstripped [see Fig. 2.8(a)]. Therefore, the electrons are stripped from the peripheral region, but most of the electrons in the core region remain intact after the passage of the laser pulse [see Figs. 2.8(b)-2.8(d)].

Most electrons, which are stripped from the peripheral region of the cluster by laser fields, are moved forward (in the  $+y$  direction) with a figure eight motion by the Lorentz force,  $\mathbf{v} \times \mathbf{B}$  [see Fig. 2.8(a)], while the heavier ions stay still [see Fig. 2.8(e)]. Here, the peripheral region of the cluster is regarded as the electron skin depth  $\delta_e = 11.6$  nm and the radius of the figure eight motion is represented as an electron excursion length  $\xi_e$  defined as

### 2.3. CHARACTERISTICS OF A SINGLE CLUSTER EXPANSION

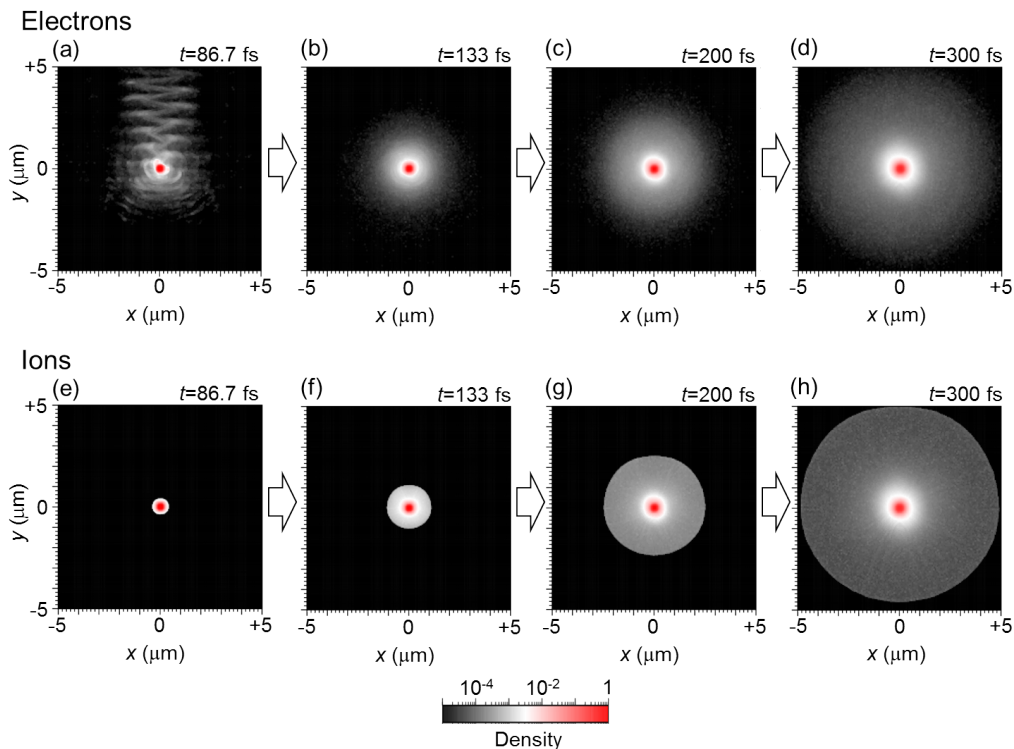


Figure 2.8: Snapshots of 2D images for the charge density distributions of (a), (b), (c), (d) electrons and (e), (f), (g), (h) ions at (a), (e)  $t = 86.7$  fs, (b), (f)  $t = 133$  fs, (c), (g)  $t = 200$  fs and (d), (h)  $t = 300$  fs. Densities are normalized by the initial charge density of the cluster ions and displayed on a log scale.

$$\xi_e = \frac{c}{\omega} \arcsin \left( \frac{a_0}{\sqrt{1 + a_0^2}} \right), \quad (2.6)$$

which corresponds to 147 nm at the peak of the laser pulse ( $a_0 = 2.19$ ) and is comparable to the cluster radius of  $a = 125$  nm. Therefore, an electric field exhibiting radially symmetric is established around the peripheral region of the cluster and cluster starts to expand by the electric field in the radial direction [see Fig. 2.8(e)-2.8(h)]. It is noted that the cluster core expands hydrodynamically because most electrons remain in the cluster core [see Figs. 2.8(a)-2.8(d)].

Namely, the relation  $\delta_e < a \sim \xi_e$  is satisfied and this type of the cluster expansion corresponds to *Case (ii)*. It is noted that the cluster expansion dynamics is slightly anisotropic (directed forward) as seen in Fig. 2.8(h) due to the anisotropic density distribution of electrons at the earlier interaction phase [see Fig. 2.8(a)].

Figure 2.9 shows the kinetic energy distributions of cluster ions at several different

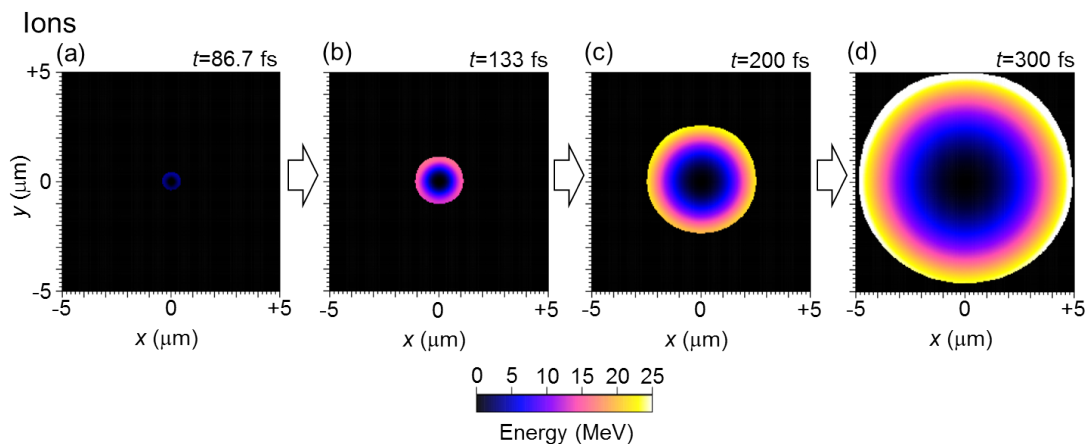


Figure 2.9: Snapshots of 2D images for the spatial energy distribution of ions at (a)  $t = 86.7$  fs, (b)  $t = 133$  fs, (c)  $t = 200$  fs and (d)  $t = 300$  fs.

times, which correspond to Fig. 2.8. The velocity of cluster ions becomes large in proportion to the initial position (= distance) from the cluster center because the intensity of the electric field linearly increases from the center of the cluster to the outside of the cluster. Then, the kinetic energy of the cluster ions also becomes large in proportion to the initial position from the center of the cluster and shows the peak value at the expansion front. It is noted that the spatial energy distribution of ions has an anisotropic structure in the  $+y$  direction [Figs. 2.9(b)-2.9(d)]. This is because the intensity of the electric field in the  $+y$  direction is slightly larger than that in other directions because electrons stripped from the cluster are mainly accelerated forward [see Fig. 2.8(a)]. This anisotropy clearly emerges when we increase the laser peak intensity and the effect of the laser magnetic field, i.e.,  $\mathbf{v} \times \mathbf{B}$ , becomes dominant. The details are discussed in Chapter 5.

Figure 2.10 shows 1D cross sectional views for the charge density distributions of cluster ions  $\rho_{i,cl}$  and electrons  $\rho_{e,cl}$ , and the resulting electric field  $E_y$  created at the cluster-vacuum boundary along the  $+y$  direction from the center of the cluster at several different times. Phase space distributions of cluster ions are also shown on the right sides. At  $t = 86.7$  fs, when the peak of the laser pulse reaches the cluster, electrons are stripped from the peripheral region due to the penetration of laser fields. As a result,  $\rho_{e,cl}$  is almost the same as  $\rho_{i,cl}$  for the cluster core region ( $y < 0.20 \mu\text{m}$ ), while the peripheral region ( $0.20 \mu\text{m} < y < 0.40 \mu\text{m}$ ) is positively charged and the outside of the cluster ( $0.40 \mu\text{m} < y$ ) is negatively charged. Consequently, the ambipolar electric field  $E_y$  having a peak intensity of 8 TV/m is created around the cluster-vacuum boundary [Fig. 2.10(a)]. The intensity of  $E_y$  decays gradually outside of the cluster approximately as an exponential function. The details are discussed in Chapter 4. Note that the corrugation of the  $\rho_{e,cl}$  with the length of  $0.40 \mu\text{m} \sim \lambda/2$  at  $1.0 \mu\text{m} < y < 6.40 \mu\text{m}$  represents the oscillation by the ponderomotive force of the laser fields in the  $+y$  direction. The corrugation disappears after the passage of the laser pulse [see Figs. 2.8(b)-2.8(d)]. Due to the ambipolar field  $E_y$ ,

### 2.3. CHARACTERISTICS OF A SINGLE CLUSTER EXPANSION

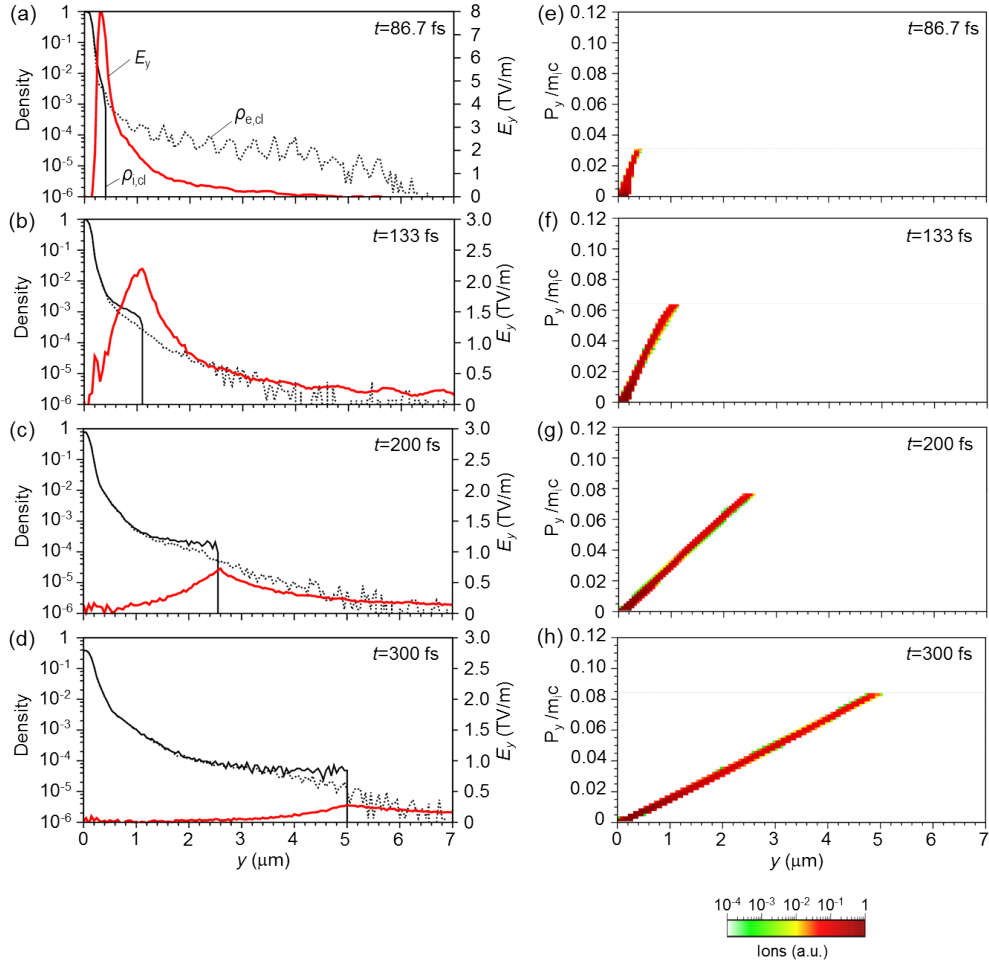


Figure 2.10: (a)-(d) 1D cross sectional views for the charge density distributions of cluster ions  $\rho_{i,cl}$  (black solid line), cluster electrons  $\rho_{e,cl}$  (black dotted line), and the resulting electric field  $E_y$  (red solid line) along the  $+y$  direction from the center of the cluster at (a)  $t = 86.7$  fs, (b)  $t = 133$  fs, (c)  $t = 200$  fs and (d)  $t = 300$  fs. Densities are normalized by the initial density of the cluster ions. (e)-(h) Phase space distributions of cluster ions along the  $+y$  direction from the center of the cluster at (e)  $t = 86.7$  fs, (f)  $t = 133$  fs, (g)  $t = 200$  fs and (h)  $t = 300$  fs. Phase space distributions are normalized by the initial charge density of the cluster ions and displayed on a log scale.

the peripheral region of the cluster undergoes a Coulomb explosion, while the cluster core expands hydrodynamically [Figs. 2.10(a)-2.10(d)]. The velocity of the cluster ions linearly increases from the center of the cluster to the outside of the cluster [Figs. 2.10(e)-2.10(h)].

As time goes on, the peak intensity of the ambipolar field  $E_y$  decreases with time [see red lines in Figs. 2.10(a)-2.10(d)] with keeping the ambipolar structure. This type of cluster breakup dynamics, consisting of two different mechanisms, is called a hydrodynamic *ambipolar expansion* [13]. As the cluster expansion develops, as shown in Figs. 2.10(a)-2.10(d), the charge separation at the the cluster expansion front decreases and therefore the intensity of the field  $E_y$  gradually decreases.

### 2.3.2 Cluster expansion in the ambient gas

Many studies concerning the interaction between the high-power laser and the cluster target have been theoretically and experimentally made so far, while the existence of an ambient gas in the cluster target has not been considered. However, in real experimental conditions, the cluster target inevitably includes the ambient gas [83]. As discussed in Fig. 2.3, the recent experimental results indicates that a new acceleration mechanism is found to take place at around an *interface* between the cluster and the ambient gas. Namely, in order to fully understand the structure and dynamics which take place in the laser-irradiated cluster target, the study of such a microscopic structure is necessary.

From the viewpoint of the explosion of the spherical dense object into the ambient dilute gas, cluster expansion into the ambient gas has a similarity to the supernova explosion into the interstellar gas. The supernova remnant evolves in the following five phases [114]:

- *Free expansion phase*: A supernova experiences free expansion with compressing an interstellar gas. In this phase, the radius of the supernova  $R$  is in proportion to the time  $t$ , i.e.,  $R \propto t$ .
- *Explosion ejecta driving phase*: The supernova starts to be decelerated by the compressed interstellar gas and internal shock is generated in the inside of the supernova, leading to the heating of the supernova remnant. In this phase, the radius  $R$  and the time  $t$  satisfy the relation,  $R \propto t^{0.8-0.9}$ .
- *Adiabatic expansion phase*: In this phase, the radius  $R$  and the time  $t$  satisfy the Sedov-Taylor solution,  $R \propto t^{0.4}$ .
- *Isothermal expansion phase*: The dynamics of the supernova remnant is dominated by radiation cooling. In this phase, the radius  $R$  and the time  $t$  satisfy the following relation,  $R \propto t^{0.25-0.3}$ .
- *Disappearance*: When the velocity of the supernova remnant slows down to the sound velocity, the remnant is hardly distinguishable from the interstellar gas.

### 2.3. CHARACTERISTICS OF A SINGLE CLUSTER EXPANSION

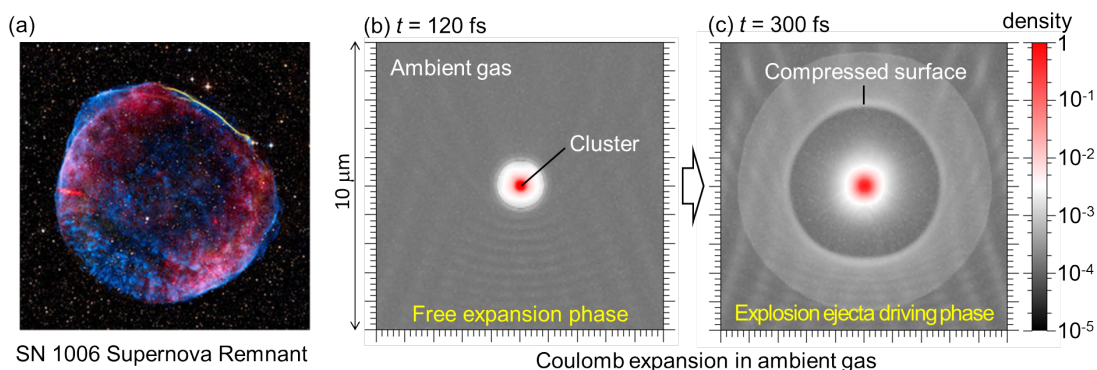


Figure 2.11: (a) Supernova explosion (SN1006) in the interstellar gas. Image is reprinted by [<https://apod.nasa.gov/apod/ap140712.html>]. Simulation results of spatial density distributions of ions resulting from the cluster expansion in the ambient gas at (b)  $t = 120$  fs and (c)  $t = 300$  fs. Densities are normalized by the initial cluster density.

Figure 2.11 shows (a) supernova explosion (SN1006) in the interstellar gas and (b), (c) simulation results of spatial density distributions of ions resulting from the cluster expansion in the ambient gas. As shown in Fig. 2.11(b), in the early expansion phase of the cluster, the cluster density are much higher than the of ambient gas density, cluster experiences free expansion with compressing ambient gas. This phase is considered to correspond to *Free expansion phase* in the supernova explosion.

As time goes on, the density of compressed ambient gas becomes high due to the continuous compression of the ambient gas by the cluster expansion, while the density of the cluster rapidly becomes low due to the significant expansion of the cluster. Resultantly, as shown in Fig. 2.11(c), the density of the compressed surface of the ambient gas becomes higher than the density of the cluster expansion front, leading to the deceleration of the cluster expansion. This phase is considered to correspond to *Explosion ejecta driving phase* in the supernova explosion.

Figure 2.12 shows the cluster radius  $R$  ( $\mu\text{m}$ ) as a function of  $t$  (fs), which is represented by blue circle, and the Sedov-Taylor solution,  $R \propto t^{0.4}$ , which is shown as red solid line. As seen in Fig. 2.12, the relation between the radius  $R$  and the time  $t$  gradually approaches the Sedov-Taylor solution,  $R \propto t^{0.4}$ . These relations suggest that the process of the cluster expansion into the ambient gas correspond to the transition from the *Free expansion phase* through the *Explosion ejecta driving phase* to the *Adiabatic expansion phase*. In addition to the similarity of the scaling law which is mentioned in Fig. 2.12, the ring-like structure, which is a kind of internal shock observed in the supernova remnant, and the establishment of the quasi-stationary kinetic equilibrium dominated by electron vortices in the phase space, which is related to the electrostatic solitary wave around magnetotail, are observed by the laser-irradiation to the cluster in the presence of the ambient gas, as we discuss in Chapter 4. Namely, to understand the structure and dynamics of the laser-irradiated cluster expansion into the ambient gas may lead to help understand the astrophysical

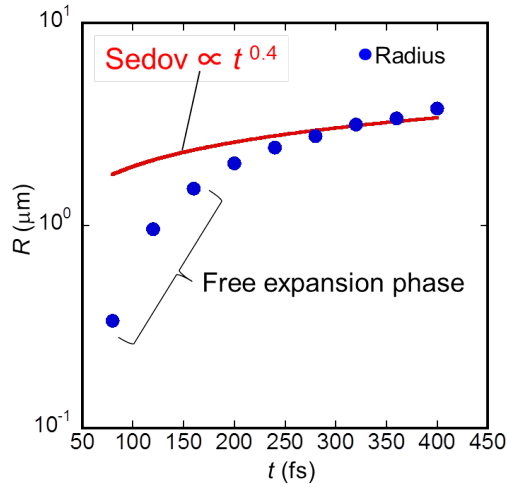


Figure 2.12: The cluster radius  $R$  ( $\mu\text{m}$ ) as a function of  $t$  (fs), which is represented by blue circle. The laser irradiation takes place at  $t = 0$  and the laser pulse reaches the cluster at  $t \sim 50$  fs. The Sedov-Taylor solution  $R \propto t^{0.4}$  is also shown as red solid line.

phenomena, e.g., the dynamics of the supernova remnant, where the high-energy cosmic rays are considered to be produced.

### 2.3.3 Collisionless plasma boundary layer

Collisionless plasma boundary layers in laboratory and natural plasmas, i.e., space and astrophysical plasmas, are generally formed when two collisionless plasmas with different characteristics interact with each other, leading to a wide range of instabilities and associated nonlinear structures.

Recently, high energy density plasmas produced by the interaction between high-power lasers in the relativistic regime and various types of targets have been widely interested, since they exhibit prominent dynamics and structures by properly choosing parameters of laser and target, which leads to academic and also industrial applications.

A typical example is the generation of high energy particles aiming at compact accelerator. An interaction between a solid thin film in the order of micro-meter and a high intensity laser has been studied to generate high energy ions by utilizing strong electrostatic sheath fields produced at the interface between the rear surface of target and vacuum. Acceleration of ions by the shock induced in a near critical density plasma irradiated by a high intensity laser has been proposed, where the shock potential produced in the downstream region with high pressure reflects ions of that of the upstream across the interface between two plasmas.

These acceleration events are found to take place at the interface between plasma and vacuum and/or that between two plasmas with different characteristics, i.e., temperature, density, species, etc., which exhibits prominent dynamics and structures as a boundary layer. Such various boundary layers, which exhibits various phenomena including those

mentioned in the above, emerge not only in laboratory but also in space and universe.

The boundary layer produced by supernova explosion in interstellar gas is an example, where complex spatio-temporal structures causing shock waves and particle accelerations are produced. Such structures, which are influenced by two-dimensional (2D) and/or three-dimensional (3D) effects, belong to a different class of structures from those produced in a planar target [57, 58, 115] irradiated by a high-power laser.

In order to elucidate the details of such structures, we propose to utilize a cluster, i.e., a spherical dense object with a solid density, as a target. This is because the cluster irradiated by a high-power laser exhibits a nearly isotropic expansion in the ambient gas, which is dimensionally similar to that of a spherical dense object in a three dimensional space, e.g., supernova explosion. From this viewpoint, in Chapter 4, we investigate the Coulomb expansion of a laser-irradiated cluster into an ambient gas aiming at the understanding of the characteristics of the boundary layer created during an explosion of a dense object into an ambient dilute gas.

## 2.4 Summary

In this Chapter, we discussed the basic characteristics of the laser-irradiated cluster, i.e., the classification of the cluster expansion dynamics, typical structures of the electric field of the Coulomb explosion, the expansion dynamics of the laser-irradiated cluster expansion into the vacuum, and the significance of the ambient gas in the cluster medium. Especially, the existence of the ambient gas is considered to play an important role in exhibiting interesting nonlinear structures, e.g., electrostatic collisionless shock, particle acceleration, establishment of quasi-stationary kinetic equilibrium, onset of rarefaction wave, through the interface between the cluster expansion front and the compressed surface. This situation can be regarded as the dynamics of the microscopic boundary layer.

From this viewpoint, in Chapter 4, we discuss the structure and dynamics of the laser-irradiated cluster expansion into the ambient gas and reveal the characteristics of the boundary layer created during an explosion of a dense object into an ambient dilute gas., which is related to the astrophysical phenomena, e.g., the dynamics of the supernova remnant in the interstellar gas.

# Chapter 3

## Shock characteristics in laser-cluster interaction

### 3.1 Collisionless shocks due to the laser-matter interaction

#### 3.1.1 Collisionless shock formation and particle acceleration

In an interaction between a high power laser pulse and a target, a part of electrons of the target is pushed forward, i.e., in the direction of the laser propagation (+ $y$  direction), due to a strong ponderomotive force and electrons are piled up in front of the laser pulse. Here, for the linearly polarized (LP) laser pulse, the ponderomotive force  $f_{p(y)}$  in the + $y$  direction is defined as

$$\mathbf{f}_{p(y)} = -\frac{1}{4} \frac{e^2}{m_e \omega_L^2} (1 + \cos 2\omega_L t) \frac{\partial}{\partial y} E(x, y)^2 \hat{\mathbf{y}}, \quad (3.1)$$

where  $m_e$ ,  $\omega_L$  and  $E(x, y)$  are the electron mass, the laser frequency and the electric field of the laser pulse as a function of  $x$  and  $y$ . Note that the second term of  $f_{p(y)}$  represents the oscillation term, which appears in the LP laser pulse.

On the other hand, ions do not directly respond to the laser fields due to their greater mass, leading to the production of a large charge separation. Then, remaining ions are attracted by electrons via a large electric field established between ions and electrons in the direction of the laser propagation. Such kinds of propagation of ions and electrons via the irradiation of the short pulse laser is called *collisionless shock*, where the mean free path is much larger than the shock width. Here, shock width is approximately determined by the Debye length.

### 3.1.2 Schematic model of collisionless shock acceleration

Collisionless shock forms the electrostatic potential at the shock front. When upstream ions are reflected by the shock potential in the shock rest frame, *collisionless shock acceleration (CSA)* takes place. Here, we show schematic models representing the relation between the potential height and the kinetic energy of the upstream ion. Situations are categorized into three patterns.

*I.*  $v_{sh} > v_{expand}$  and  $\Delta U > K_{ion} = 1/2m_i(v_{sh}-v_{expand})^2$

Figure 3.1 shows the 1D images of the shock acceleration in the shock rest frame. In the shock rest frame, electrostatic potential created by the shock reflects incoming upstream ions. Note that when upstream ions are accelerated by the leading edge of the shock potential or the sheath electric field prior to the shock acceleration, upstream ions have a velocity of  $v_{expand}$  in the laboratory frame. In the condition that the velocity of the upstream ion  $v_{expand}$  is smaller than the shock velocity  $v_{sh}$  [Fig. 3.1(A)] and the kinetic energy of incoming upstream ion  $K_{ion} = 1/2m_i(v_{sh} - v_{expand})^2$  belows the shock potential height  $\Delta U$ , the upstream ion climbs the potential hill and temporarily stops at the turn-round point on the halfway of the potential [Fig. 3.1(B)]. It is noted that the process from (A) to (B) results in the formation of a thermalized part in the phase space distribution of upstream ions, which leads to the increase of the downstream region. The upstream ion is reflected by the potential and turns back on the potential slope. Finally, the upstream ion obtains the velocity of  $v_{sh} - v_{expand}$  in the  $+y$  direction [Fig. 3.1(C)] after reflection. This situation corresponds to the case (i) in the laboratory frame (Fig. 3.2).

In the laboratory frame, the shock acceleration occurs in the case (i). That is, in the case  $v_{sh} > v_{expand}$  and  $\Delta U > K_{ion} = 1/2m_i(v_{sh} - v_{expand})^2$ , the shock front catches up with the upstream ion with an initial velocity of  $v_{expand}$  and accelerates the ion as the moving wall, i.e., the shock potential with a constant velocity of  $v_{sh}$  (Fig. 3.2(A)). Then, the velocity of the ion becomes the same velocity as the moving wall, i.e.,  $v_{sh}$  (Fig. 3.2(B)). Finally, the ion is further accelerated by the potential slope and obtains the velocity of  $2v_{sh} - v_{expand}$  (Fig. 3.2(C)). Note that in the ideal condition of  $v_{expand} = 0$ , upstream resting ion finally obtains the velocity of  $2v_{sh}$ .

*II.*  $v_{sh} > v_{expand}$  and  $\Delta U < K_{ion} = 1/2m_i(v_{sh}-v_{expand})^2$

In the condition that  $v_{sh} > v_{expand}$  and the kinetic energy of incoming ions  $K_{ion}$  exceeds the shock potential height  $\Delta U$ , as shown in Fig. 3.3, the upstream ion is not reflected by the potential wall and pass over it. Namely, the ion has a velocity of  $v_{tmp1}$  ( $0 < v_{tmp1} < v_{sh}$ ) at the top of the potential [Fig. 3.3(B)]. After that, the ion is slightly accelerated to the velocity of  $v_{tmp2}$  by the backward of the potential, while its velocity cannot reach to  $v_{sh}$  [Fig. 3.3(C)].

*III.*  $v_{sh} < v_{expand}$

Finally, as shown in Fig. 3.4, in the condition that the upstream ion with the velocity of  $v_{expand1}$  exceeds the shock velocity  $v_{sh}$  ( $v_{sh} < v_{expand1}$ ), the ion is further accelerated

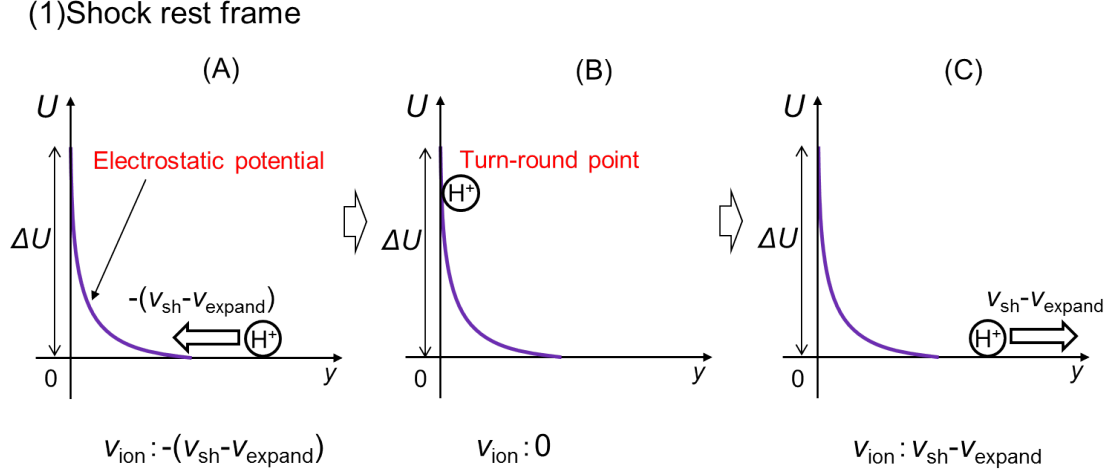


Figure 3.1: 1D images of the shock acceleration in the *shock rest frame* in the  $+y$  direction. Purple solid lines represent the electrostatic shock potential. (A) The upstream ion is incoming to the electrostatic shock potential with the velocity of  $-(v_{sh} - v_{expand})$  in the  $-y$  direction. (B) The incoming ion temporarily stops on the halfway of the potential. (C) The ion obtains the velocity of  $v_{sh} - v_{expand}$  in the  $+y$  direction.

(2) Laboratory frame

(i)  $v_{sh} > v_{expand} \geq 0$ ,  $\Delta U \geq K_{ion}$

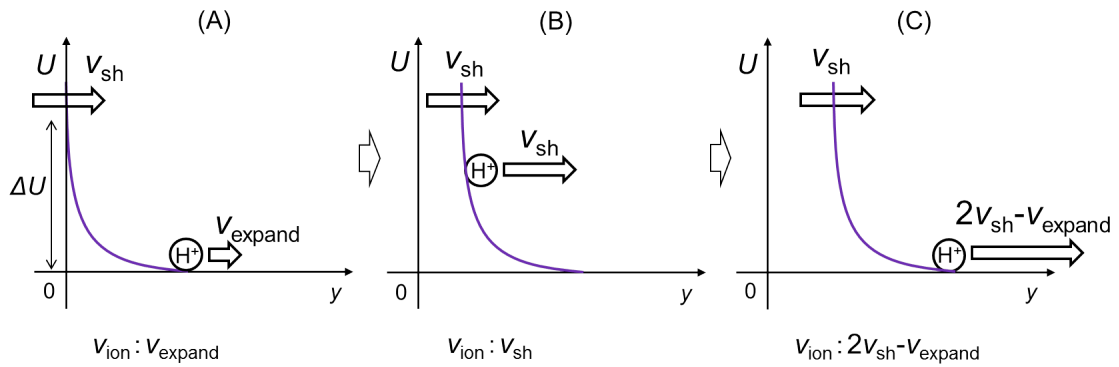


Figure 3.2: 1D images of the shock acceleration in the *laboratory frame* in the  $y$  direction. Purple solid lines represent the shock potential. (A) The upstream ion moves with the velocity of  $v_{expand}$  in the  $+y$  direction. (B) The ion moves with the velocity of  $v_{sh}$  in the  $+y$  direction. (C) Finally the ion obtains the velocity of  $2v_{sh} - v_{expand}$ .

(2) Laboratory frame

(ii)  $v_{sh} > v_{expand} \geq 0$ ,  $\Delta U < K_{ion}$

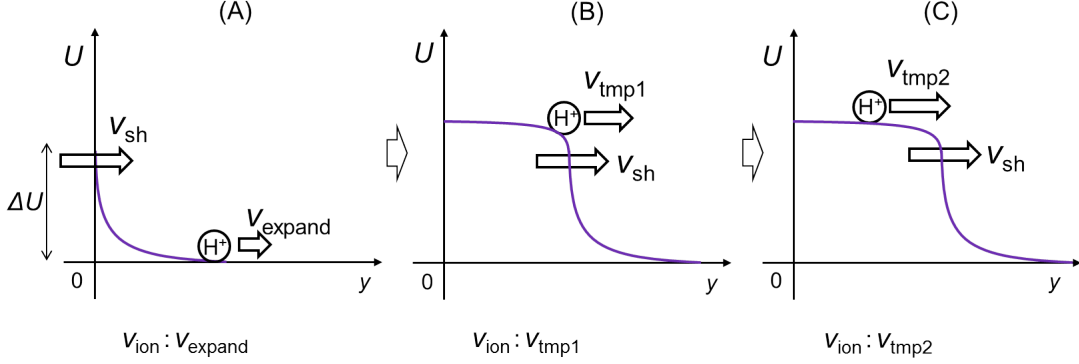


Figure 3.3: 1D images of the shock acceleration in the *laboratory frame* in the  $y$  direction. Purple solid lines represent the shock potential. (A) The upstream ion moves with the velocity of  $v_{expand}$  in the  $+y$  direction. (B) On the top of the shock potential, the ion moves with the velocity of  $v_{tmp1}$  ( $v_{tmp1} < v_{sh}$ ) in the  $+y$  direction. (C) Finally the ion obtains the velocity of  $v_{tmp2}$  ( $v_{tmp2} < v_{sh}$ ). That is, the ion passes over the shock potential.

by the leading edge of the shock potential (Fig. 3.4(A)). As a result, its velocity becomes  $v_{expand2}$  ( $v_{expand1} < v_{expand2}$ ) (Fig. 3.4(B)). This situation is not categorized to the shock acceleration.

### 3.1.3 Theoretical model of collisionless shock

In this subsection, we derive the relation between the Mach number and the shock potential. We begin by using following equations, i.e., the continuity equation, the force equation and Poisson's equation for the ion fluid:

$$\frac{\partial n}{\partial t} + \frac{\partial}{\partial x}(nv) = 0 \quad (3.2)$$

$$\frac{\partial v}{\partial t} + v \frac{\partial v}{\partial x} = -\frac{Ze}{M} \frac{\partial \phi}{\partial x} \quad (3.3)$$

$$-\frac{\partial^2 \phi}{\partial x^2} = 4\pi e(Zn - n_e) \quad (3.4)$$

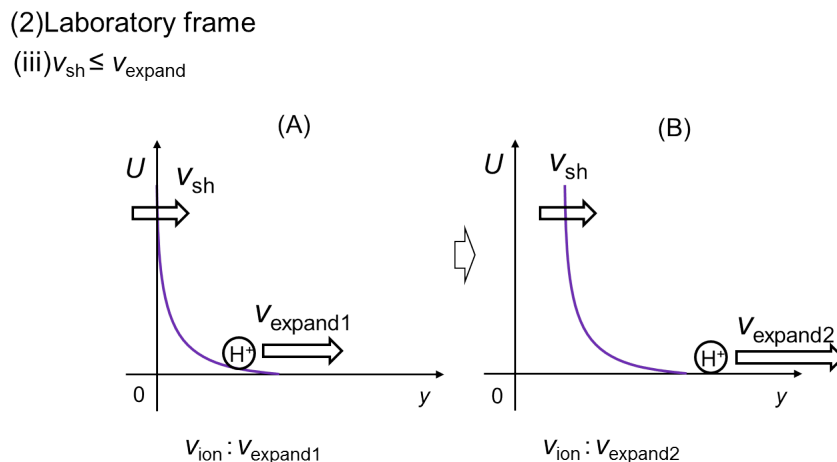


Figure 3.4: 1D images of the shock acceleration in the *laboratory frame* in the  $y$  direction. Purple solid lines represent the shock potential. (A) The upstream ion moves with the velocity of  $v_{expand1}$  in the  $+y$  direction ( $v_{sh} < v_{expand1}$ ). (B) The ion is accelerated by the leading edge of the shock potential and obtains the velocity of ( $v_{sh} < v_{expand1} < v_{expand2}$ ) in the  $+y$  direction.

Here, we assume the ion pressure is negligible compared with the electron pressure. Here,  $n$  and  $v$  are the ion density and flow velocity,  $e$  is the elementary charge,  $Z$  the ion charge state,  $M$  is the ion mass,  $\phi$  is the electrostatic potential,  $n_e$  is the electron density. In the shock rest frame ( $\partial/\partial t = 0$ ), Eq. (3.2) becomes

$$\frac{\partial}{\partial x}(nv) = 0$$

$$\therefore nv = n_1 v_1 \quad (3.5)$$

Here,  $n = n_1$  and  $v = v_1$  at infinity. Eq. (3.3) also becomes

$$v \frac{\partial v}{\partial x} + \frac{Ze}{M} \frac{\partial \phi}{\partial x} = 0$$

$$\frac{\partial}{\partial x} \left( \frac{1}{2} M v^2 + Ze\phi \right) = 0$$

$$\therefore \frac{1}{2}Mv^2 + Ze\phi = \text{const.} \quad (3.6)$$

By using  $v = v_1$  and  $\phi = 0$  at infinity, we obtain from Eq. (3.6)

$$\begin{aligned} \frac{1}{2}Mv^2 + Ze\phi &= \frac{1}{2}Mv_1^2 \\ \therefore v &= \sqrt{v_1^2 - \frac{2Ze\phi}{M}} \end{aligned} \quad (3.7)$$

Substituting Eq. (3.7) into Eq. (3.5), we obtain

$$n = \frac{n_1 v_1}{v} = \frac{n_1 v_1}{\sqrt{v_1^2 - \frac{2Ze\phi}{M}}} \quad (3.8)$$

We consider the Boltzmann distribution for electrons, i.e.,  $n_e = n_e^0 \exp(e\phi/kT_e)$ , where  $n_e^0 = Zn_1$ ,  $k$  is Boltzmann's constant and  $T_e$  is the electron temperature. Substituting Eq. (3.8) and  $n_e = Zn_1 \exp(e\phi/kT_e)$  into Eq. (3.4), we obtain

$$-\frac{\partial^2 \phi}{\partial x^2} = 4\pi e \left\{ \frac{Zn_1 v_1}{\sqrt{v_1^2 - \frac{2Ze\phi}{M}}} - Zn_1 \exp\left(\frac{e\phi}{kT_e}\right) \right\} \quad (3.9)$$

Multiplying by  $(\partial\phi/\partial x)$  gives

$$\frac{\partial \phi}{\partial x} \left[ -\frac{\partial^2 \phi}{\partial x^2} - 4\pi e n_1 \left\{ \frac{Zv_1}{\sqrt{v_1^2 - \frac{2Ze\phi}{M}}} - Z \exp\left(\frac{e\phi}{kT_e}\right) \right\} \right] = 0 \quad (3.10)$$

Integrating with respect to  $x$ ,

$$-\frac{1}{2} \left( \frac{\partial \phi}{\partial x} \right)^2 - 4\pi e n_1 \int \frac{Z v_1}{\sqrt{v_1^2 - \frac{2Ze\phi}{M}}} d\phi + 4\pi e n_1 \int Z \exp\left(\frac{e\phi}{kT_e}\right) d\phi = 0 \quad (3.11)$$

$$\therefore \frac{1}{2} \left( \frac{\partial \phi}{\partial x} \right)^2 - 4\pi n_1 M v_1 \sqrt{v_1^2 - \frac{2Ze\phi}{M}} - 4\pi n_1 Z k T_e \exp\left(\frac{e\phi}{kT_e}\right) + C = 0 \quad (3.12)$$

Here,  $C$  is integral constant. The constant is evaluated as  $C = 4\pi n_1 (M v_1^2 + Z k T_e)$  by noting that  $\phi = 0$  and  $\partial\phi/\partial x = 0$  at  $x \rightarrow \infty$ . Then, Eq. (3.12) becomes

$$\therefore \frac{1}{2} \left( \frac{\partial \phi}{\partial x} \right)^2 - 4\pi n_1 M v_1 \sqrt{v_1^2 - \frac{2Ze\phi}{M}} - 4\pi n_1 Z k T_e \exp\left(\frac{e\phi}{kT_e}\right) + 4\pi n_1 (M v_1^2 + Z k T_e) = 0 \quad (3.13)$$

Under the condition of the existence of the shock potential,  $\partial\phi/\partial x = 0$  is satisfied. By substituting  $\partial\phi/\partial x = 0$  into Eq. (3.13), we obtain

$$-4\pi n_1 M v_1 \sqrt{v_1^2 - \frac{2Ze\phi}{M}} - 4\pi n_1 Z k T_e \exp\left(\frac{e\phi}{kT_e}\right) + 4\pi n_1 (M v_1^2 + Z k T_e) = 0 \quad (3.14)$$

Dividing by  $-4\pi n_1$ , Eq. (3.14) becomes

$$M v_1 \sqrt{v_1^2 - \frac{2Ze\phi}{M}} = Z k T_e \left\{ 1 - \exp\left(\frac{e\phi}{kT_e}\right) \right\} + M v_1^2 \quad (3.15)$$

Organizing Eq. (3.15),

$$\begin{aligned} \frac{v_1^2}{\frac{ZkT_e}{M}} \left\{ \exp\left(\frac{e\phi}{kT_e}\right) - 1 - \frac{e\phi}{kT_e} \right\} &= \frac{1}{2} \left\{ 1 - \exp\left(\frac{e\phi}{kT_e}\right) \right\}^2 \\ \frac{v_1^2}{\frac{ZkT_e}{M}} &= \frac{\frac{1}{2} \left\{ 1 - \exp\left(\frac{e\phi}{kT_e}\right) \right\}^2}{\left\{ \exp\left(\frac{e\phi}{kT_e}\right) - 1 - \frac{e\phi}{kT_e} \right\}} \\ \therefore \frac{v_1}{\sqrt{\frac{ZkT_e}{M}}} &= \frac{1}{\sqrt{2}} \frac{\exp\left(\frac{e\phi}{kT_e}\right) - 1}{\sqrt{\exp\left(\frac{e\phi}{kT_e}\right) - 1 - \frac{e\phi}{kT_e}}} \end{aligned} \quad (3.16)$$

Here, the Mach number is defined as  $\mathcal{M} = v_1/c_s = v_1/\sqrt{ZkT_e/M}$ , where  $c_s = \sqrt{ZkT_e/M}$  is the well-known ion acoustic velocity. In the unit of eV for  $T_e$ ,  $k = 1$ . When we consider the ion is proton,  $Z = 1$ . Then, Eq. (3.16) is simplified by

$$\mathcal{M} = \frac{1}{\sqrt{2}} \frac{\exp\left(\frac{e\phi}{T_e}\right) - 1}{\sqrt{\exp\left(\frac{e\phi}{T_e}\right) - 1 - \frac{e\phi}{T_e}}} \quad (3.17)$$

### 3.1.4 Collisionless shock acceleration in 1D case

In order to understand the structure of collisionless shock and the mechanism of CSA, firstly, we show the typical one-dimensional (1D) simulation results concerning the interaction between solid hydrogen target and a high power laser. The system size is  $L_x \times L_y = 0.04 \mu\text{m} \times 20.48 \mu\text{m}$  containing  $4 \times 2048$  cells. A cell size of 10 nm is employed to resolve the shock ( $\sim 0.40 \mu\text{m}$ ) and the associated electric field structures. The plane

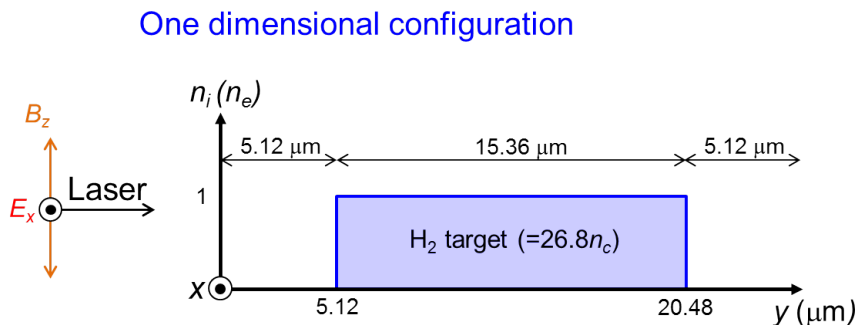


Figure 3.5: One dimensional configurations of simulation setup. The solid hydrogen target is located at  $5.12 \leq y \leq 20.48 \mu\text{m}$ . Laser irradiation occurs at  $t = 0$  fs and the laser pulse propagates in the  $+y$  direction.

solid hydrogen target with an electron density of  $4.6 \times 10^{22} \text{ cm}^{-3} = 26.8n_c$ , where  $n_c$  is the critical density of the plasma corresponding to the laser wavelength  $\lambda = 0.81 \mu\text{m}$ , is placed at  $5.12 \leq y \leq 20.48 \mu\text{m}$ . The number of PIC particles used for the protons are 33 per mesh, and a fully ionized plasma is employed as the initial condition. A linearly polarized laser pulse in the  $x$  direction with a wavelength of  $\lambda = 0.81 \mu\text{m}$  is generated from an antenna located at  $y = 0.02 \mu\text{m}$  and propagates in the  $+y$  direction. Here, we utilize a continuous laser having a pulse duration of  $\tau = 33$  fs (FWHM) on the leading edge of pulse. The peak intensity of the laser pulse is set to  $I = 1.0 \times 10^{22} \text{ W/cm}^2$ , which corresponds to the normalized amplitude of a laser  $a_0 = 69$ , where  $a_0 = eE/m_e\omega_{LC}$ . For the fields and particles, a periodic boundary condition is employed in the  $x$  direction, and a transparent boundary condition is employed in the  $y$  direction.

Figure 3.3(a) shows density distributions for ions and electrons, and electric field  $E_y$  at different times. The electrostatic collisionless shock is launched at the laser-irradiated surface [see  $y = 6 \mu\text{m}$  in Fig. 3.3(a1)]. The density of the shock structure is  $\sim 4$  times larger than the initial density. The laser propagates in the  $+y$  direction with pushing the shock structure. Then, the shock structure also propagates in the  $+y$  direction with taking upstream protons inside the shock structure and with keeping the density almost constant value. It is noted that the shock surface [indicated by the arrow “shock” in Fig.3.3(a)] propagates with the larger velocity than the velocity of the push surface [indicated by the arrow “push” in Fig.3.3(a)], which leads to that the distance between the push surface and the shock surface becomes wide over time as seen in Fig.3.3(a). Figure 3.3(b) shows phase space distributions of protons at different times. The times at (a1), (a2) and (a3) correspond to those at (b1), (b2) and (b3), respectively. At  $t = 60.0$  fs, the shock electric field starts to reflect the upstream protons. Namely, the collisionless shock acceleration starts to occur as seen in Fig.3.3(b1). Then, reflected upstream protons forms quasimonoenergetic component ( $\sim 50$  MeV) in the energy spectrum as seen in black line in Fig.3.4. As seen in Figs. 3.3(b2) and (b3), the thermal region (between the push surface and the shock surface) grows with time and the energy of quasimonoenergetic component reaches  $\sim 130$  MeV (see red and blue lines in Fig. 3.4). The series of process is

Table 3.1: System parameters

species	values
$x$	$0 \leq x \leq 0.04 \mu\text{m}$
$y$	$0 \leq y \leq 25.60 \mu\text{m}$
Mesh numbers $N_x$	4
Mesh numbers $N_y$	2560
Grid size $\Delta_x$	10 nm
Grid size $\Delta_y$	10 nm
Time step $\Delta t$	$6.67 \times 10^{-18}$ fs
Boundary conditions	periodic in $x$ direction and transparent in $y$ direction for both particles and fields

Table 3.2: Solid hydrogen

species	values
Ion species	Hydrogen
Target size	$l_x \times l_y = 0.04 \times 15.36 \mu\text{m}$
Ion density	$4.6 \times 10^{22} \text{ cm}^{-3}$
Electron density	$4.6 \times 10^{22} \text{ cm}^{-3}$
Particle numbers (ions)	204800 (33 per mesh)

Table 3.3: Laser parameters

species	values
Laser type	continuous laser (Gaussian on the leading edge of pulse)
Peak intensity	$1.0 \times 10^{22} \text{ W cm}^{-2}$
Normalized amplitude	$a_0 = 69$
Wavelength	$0.81 \mu\text{m}$
Critical density	$1.7 \times 10^{21} \text{ cm}^{-3}$
Pulse width	33 fs (Full Width at Half Maximum on the leading edge of pulse)
Antenna position	$y=0.02 \mu\text{m}$
Polarization	Linearly polarized (P)
Propagation	$+y$ direction
Electric field	$x$ direction
Magnetic field	$z$ direction

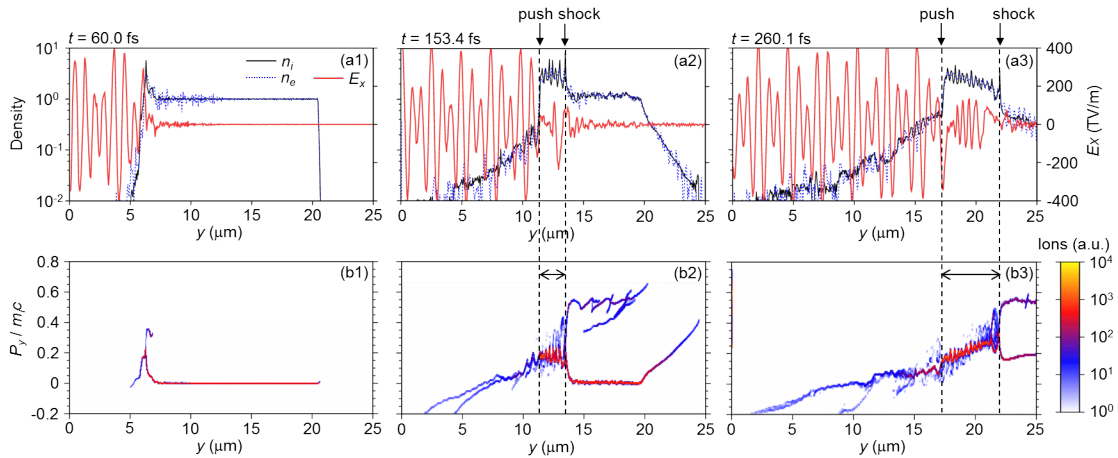


Figure 3.6: One dimensional configurations of (a) density (ions and electrons) and electric field  $E_y$ , and (b) phase space distributions of ions at (a1), (b1)  $t = 60.0$  fs, (a2), (b2)  $t = 153.4$  fs, and (a3), (b3)  $t = 260.1$  fs. The solid hydrogen target is initially located at  $5.12 \leq y \leq 20.48 \mu\text{m}$ . Laser irradiation occurs at  $t = 0$  fs and the laser pulse propagates in the  $+y$  direction.

typical mechanism of short-pulse laser induced collisionless shock acceleration. In the next section, we show the new acceleration mechanism combined with the shock acceleration and the characteristics of spherical shape of the hydrogen cluster in the relativistically induced transparency regime.

## 3.2 Collisionless shocks in laser-irradiated cluster medium

Due to a high power laser irradiation to the cluster medium, two kinds of collisionless shock is formed in the inside and outside of the cluster. One is an *external collisionless shock*, which propagates in the radial direction outside the cluster. The other is an *internal collisionless shock*, which propagates into the cluster center. The external collisionless shock is universally formed at an interface between the cluster and the ambient gas by the Coulomb explosion of the cluster in the ambient gas. On the other hand, the onset of the internal collisionless shock requires conditions concerning the intensity of the laser and the density of the target. In the following, we overview these collisionless shocks related to Chapter 4 and 5, which are microscopic structure and dynamics concerning individual cluster in the cluster medium.

### 3.2.1 External collisionless shock

An *external collisionless shock* is formed by the Coulomb explosion of the cluster in the ambient gas, leading to the compression of the ambient gas as shown in Fig. 3.8. The

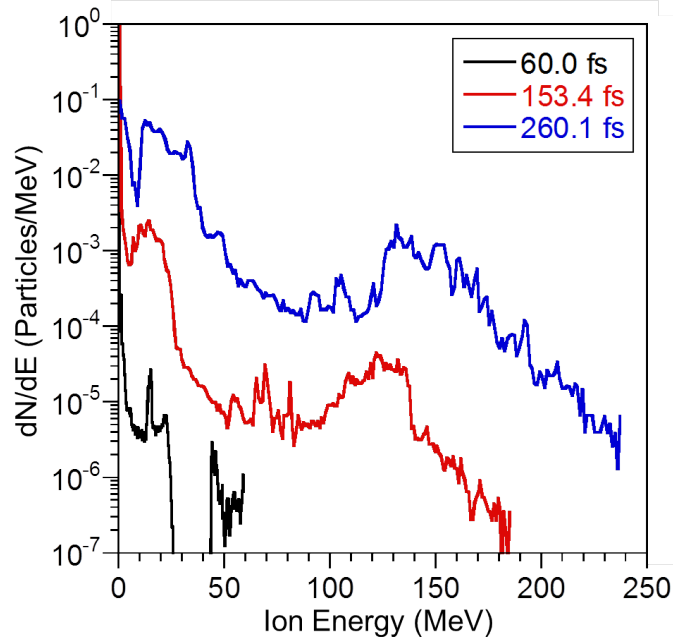


Figure 3.7: Proton energy spectra at  $t = 60.0$  fs (black),  $153.4$  fs (red), and  $260.1$  fs (blue).

compression of the ambient gas ions corresponds to the collisionless shock acceleration. Here, the electrostatic potential created by the electric field of the Coulomb explosion reflects upstream ambient gas ions as a shock potential in the *shock rest frame* [see Fig. 3.3]. The collisionless shock acceleration takes place under the condition that the shock potential is high enough to reflect all upstream ambient gas ions and the Mach number is exceed 1.6 [116]. As we discuss in Chapter 4, the intensity of the electric field of the Coulomb explosion decays quickly with the time scale of  $\sim 19$  fs due to the significant expansion of the cluster. Resultantly, the upstream ambient gas ions start to pass over the shock potential [see Fig. 3.4], leading to the termination of the shock acceleration.

Such an external collisionless shock is considered to be universally formed around the interface between two distinct collisionless plasmas with different characteristics. Namely, not restricted to the case with the laser-irradiated cluster medium, external collisionless shocks are widely observed not only in the laboratory condition but also in the space and universe, e.g., supernova explosion in the interstellar gas, which is considered to be the origin of high-energy ( $\sim 10^{15}$  eV) cosmic rays. We regard such external collisionless shocks as the characteristic which takes place in the boundary layer and discuss the structure and dynamics of the boundary layer in Chapter 4.

### 3.2.2 Internal collisionless shock

An *internal collisionless shock* is formed in the inside of the cluster by the irradiation of a high power laser pulse to the cluster as shown in Fig. 3.9. The onset of the internal collisionless shock depends on the relation between the intensity of the laser

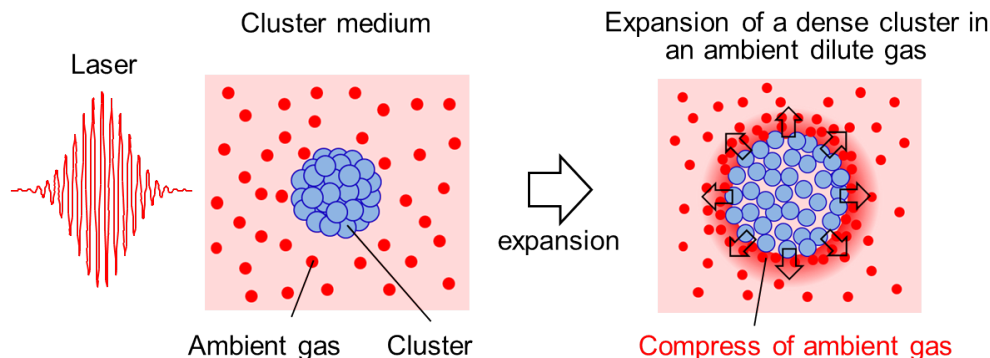


Figure 3.8: 2D schematic view of the external collisionless shock formed by the Coulomb explosion of the cluster in the ambient gas. The laser-irradiated cluster in the ambient gas undergoes Coulomb explosion, which leads to the compression of the ambient gas.

and the electron density of the cluster. When the laser intensity is relatively large, i.e., the relativistic effect is dominant, the electron skin depth  $\delta_e$  becomes large. Then, the large charge separation between the ions and electrons is induced, and a crescent-shaped collisionless shock is launched on the laser-irradiated hemisphere of the cluster as seen in Fig. 3.9(a). As time goes on, the shock propagates into the cluster center with converging, which is ascribed to the spherical structure of the cluster as seen in Figs. 3.9(b) and (c). The height of the shock potential becomes large due to the converging of the shock, leading to the shock acceleration of upstream ions.

On the other hand, when the laser intensity is relatively small, the electron skin depth  $\delta_e$  becomes small. Then, the charge separation also becomes small and the collisionless shock is not formed. Namely, ultra-high intensity laser, e.g., the peak intensity of the laser  $I \sim 10^{23-24}$  W/cm<sup>2</sup>, is required for high- $Z$  cluster with an electron density of  $\geq 10^{23}$  cm<sup>-3</sup>. At present, we can obtain the peak intensity of the laser  $I \sim 10^{21-22}$  W/cm<sup>2</sup>, which is suitable for the onset of the collisionless shock in the hydrogen cluster with an electron density of  $\sim 10^{22}$  cm<sup>-3</sup>, as we discuss in Chapter 5.

By utilizing such a hemispherically converging collisionless shock formed in the inside of the cluster, we can obtain quasimonoenergetic ions for medical applications, i.e., cancer therapy. From this viewpoint, we discuss the internal collisionless shock created in the hydrogen cluster in Chapter 5.

### 3.3 Summary

In this Chapter, we discussed two kinds of electrostatic collisionless shock structures produced in the laser-irradiated cluster medium, i.e., one is the external collisionless shock, which is formed in the ambient gas and propagates in the radial direction, and the other is the internal collisionless shock, which is formed on the laser-irradiated hemisphere of the cluster and propagates to the cluster center. The external shock structure is

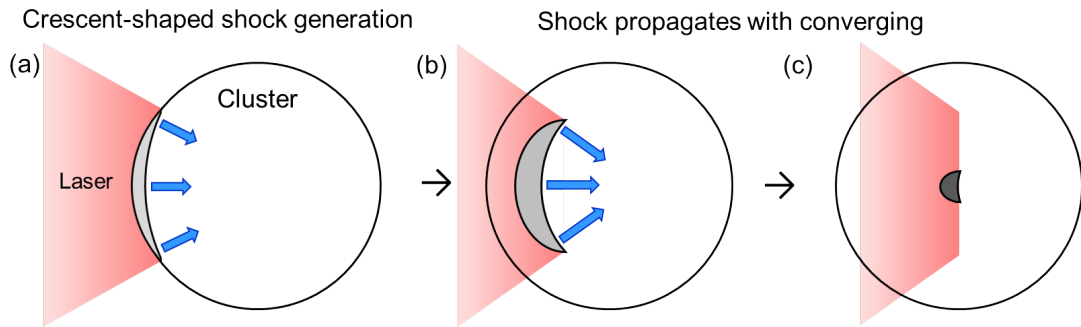


Figure 3.9: 2D schematic view of the internal collisionless shock formed by the laser irradiation into the cluster. The crescent-shaped collisionless shock launched on the laser-irradiated hemisphere of the cluster (a) is propagates into the cluster center with converging (b), (c) due to the spherical structure of the cluster.

similar to the shock structure formed by the supernova explosion in the interstellar gas. The internal shock produces the high-quality protons which are applicable to medical applications, e.g., cancer therapy. In the following Chapters, we discuss our important findings concerning the structure and dynamics of the external shock in terms of the microscale shock structure, which emerges around the micro-size individual clusters.

# Chapter 4

## Structure and dynamics of the collisionless plasma boundary layer

### 4.1 Overview

In this chapter, we discuss the dynamics of the boundary layer in between two distinct collisionless plasmas created by the interaction of a cluster medium with a short laser pulse in the presence of an ambient gas by using the results of two-dimensional particle-in-cell simulations. We found that the dynamics of the boundary layer is categorized into three successive processes, i.e., the phase 1 that a contact surface exists, the phase 2 that an overlapping region between two plasmas appears, and the phase 3 that a rarefaction wave is induced in the ambient gas ions. The details are as follows: In the first phase, laser-irradiated cluster expands with keeping a contact surface between the Coulomb expansion front of the cluster ions and the compressed surface of the ambient gas ions. At this phase, a collisionless electrostatic shock wave, launched near the cluster expansion front, reflects the ambient gas ions at a contact surface as a moving wall, which allows a particle acceleration with a narrower energy spread. In the second phase, the contact surface disappears and the compressed surface of the ambient gas ions passes over the shock potential, resulting in the formation of an overlapping region between the cluster expansion front and the compressed surface. At this phase, the shock structure is relaxed and the shock acceleration terminates, while another type of nonlinear wave having a bipolar electric field structure evolves at the compressed surface. Namely, a transition from the ambipolar electric field structure to the bipolar electric field structure occurs. Ambient gas ions are reflected by the potential associated with the nonlinear wave. The nonlinear wave exhibits a bipolar electric field structure which is sustained for a long time scale coupled with slowly evolving ion dynamics. This suggests that a Bernstein-Greene-Kruskal (BGK) type quasi-stationary kinetic equilibrium [117,118] dominated by electron vortices in the phase space consisting of trapped and passing electrons is established. Such a kinetic equilibrium has been a long-standing interest in wide-ranging plasma physics from natural plasmas to those in laboratory, since it is essentially different from the thermodynamic one, where the phase space is relaxed to a Maxwellian distribution to

the highest entropy state. In the third phase, a rarefaction wave, i.e., the destruction of the compressed surface, is triggered and evolves at the compressed surface due to that the ambient gas ions pass over the potential associated with the bipolar electric field. As a result, the reflection of ambient gas ions terminates. Simultaneously, a formation of a staircase structure, i.e., a kind of internal shock, takes place in the cluster due to the deceleration of cluster ions, leading to multiple ring-like and/or staircase structures in the cluster during the interaction. These phenomena are clearly observed when we increase the density of ambient gas. In terms of the entropy conservation derived from the nature of a collisionless plasma, the increase in entropy resulting from the destruction of the compressed surface is counterbalanced by the decrease in entropy resulting from the structure formation of the cluster. The formation of such ring structures can be seen in many places in the universe. Such structure formations and dynamics coupled with the kinetic equilibrium are considered to be a unique nature at the boundary layer created by an explosion of a dense plasma object in an ambient dilute plasma.

The rest of this chapter is organized as follows. In Section 4.2, we describe the dynamics of boundary layer in between cluster and ambient gas, which is divided into four subsections, i.e., subsection 4.2.1: Numerical modelings for the simulations using EPIC3D [112] together with the configuration and parameters of a laser and a cluster medium consisting of solid cluster and ambient gas, subsection 4.2.2: Overview of the structure and dynamics of boundary layer, subsection 4.2.3: Ion acceleration by nonlinear waves, and subsection 4.2.3: Formation of quasi-stationary kinetic equilibrium characterized by the electron vortices in the phase space. In Section 4.3, we discuss the dynamics of boundary layer for the different density of the ambient gas, which is divided into four subsections, i.e., subsection 4.3.1: The density dependence concerning the evolution of the structure at the boundary layer including the establishment of the equilibrium state, subsection 4.3.2: Density dependence for the time which the crossing between cluster and ambient gas occurs, and the time which the rarefaction wave is triggered, subsection 4.3.3: Numerical investigation of the crossing time, and subsection 4.3.4: Maximum kinetic energy of the ambient gas ions. Summary is given in Section 4.4.

## 4.2 Dynamics of boundary layer in between cluster and ambient gas

### 4.2.1 Numerical modeling

Simulations are performed using a 2D version of the particle based integrated code, EPIC3D [112]. The simulation parameters replicate the experimental works [110,111]: a cluster medium consists of a single carbon cluster with a radius of 125 nm, an electron density of  $3.8 \times 10^{23} \text{ cm}^{-3}$  ( $= 227n_c$ ), and a surrounding ambient hydrogen gas with an electron density of  $4.0 \times 10^{19} \text{ cm}^{-3}$  ( $= 0.024n_c$ ), where  $n_c = 1.7 \times 10^{21} \text{ cm}^{-3}$  is the critical density of the plasma corresponding to the laser wavelength  $\lambda = 0.81 \text{ }\mu\text{m}$ . Here,  $n_c$  is defined as

$$n_c = \frac{m_e \omega_L^2}{4\pi e^2} = 1.1 \times 10^{21} \times \frac{1}{\{\lambda(\mu\text{m})\}^2}. \quad (4.1)$$

The initial cluster radius of 125 nm is greater than the collisionless electron skin depth  $\delta_e = 11.6 \text{ nm}$ . The skin depth  $\delta_e$  is defined as

$$\delta_e = \frac{c}{\sqrt{\omega_p^2 - \omega_L^2}}, \quad (4.2)$$

where  $c$  is the speed of light and  $\omega_p = \sqrt{4\pi e^2 n_e / \gamma_e m_e}$  (the Lorentz factor  $\gamma_e$  is defined as  $\gamma_e = \sqrt{1 + a_0^2/2}$  for the linearly polarized laser pulse) is a relativistic plasma frequency.

The number of PIC particles used for carbon cluster ions and the ambient hydrogen gas ions are 2,453,000 and 7,334,000, respectively. The size of the simulation box is  $L_x = L_y = 25.60 \text{ }\mu\text{m}$ . A grid size of 10 nm is employed to resolve the cluster expansion dynamics and the associated electric field structures. The cluster center is located at the center of the box at  $(x, y) = (0, 0)$ . The ambient hydrogen gas occupies the region of  $-7.68 < (x, y) < +7.68 \text{ }\mu\text{m}$ , except for the cluster area. The vacuum region surrounds the ambient gas area to minimize the creation of artificial sheath fields at the boundary area. A linearly polarized laser pulse in the  $x$  direction with a wavelength  $\lambda = 0.81 \text{ }\mu\text{m}$  and a pulse duration (FWHM)  $\tau = 33 \text{ fs}$  is generated from an antenna located at  $y = -12.78 \text{ }\mu\text{m}$  and propagates in the  $+y$  direction. The peak intensity of the laser pulse is set to  $I = 1.0 \times 10^{19} \text{ W/cm}^2$ , which corresponds to the normalized amplitude of a laser  $a_0 = 2.19$ , where  $a_0 = eE/m_e \omega c$ . Here, the relation between  $I$  and  $a_0$  is described as

## 4.2. DYNAMICS OF BOUNDARY LAYER IN BETWEEN CLUSTER AND AMBIENT GAS

---

$$a_0 = 8.55 \times 10^{-10} \{I(\text{W cm}^{-2})\}^{\frac{1}{2}} \lambda(\mu\text{m}). \quad (4.3)$$

The pulse peak passes through the center of the cluster at  $t = 86.7$  fs. The simulation is carried out up to  $t = 600$  fs. Transparent boundary conditions are employed for the fields and the particles in the  $x$  and  $y$  directions.

The estimated laser intensity required to ionize carbon atoms and generate  $\text{C}^{6+}$  is  $I_a = 6.4 \times 10^{18}$  W/cm<sup>2</sup> [113]. Here,  $I_a$  is represented as

$$I_a = 4 \times 10^9 \times \left( \frac{E_{ion}}{eV} \right)^4 Z^{-2} (\text{W cm}^{-2}) \quad (4.4)$$

where  $E_{ion}$  ( $= 490.8$  eV for  $\text{C}^{6+}$  and  $13.6$  eV for  $\text{H}^+$ ) is the ionization energy and  $Z$  is the ion charge state.

Since the carbon atoms can be ionized not only by the field ionization but also by the electron impact ionization, carbon atoms in the cluster should be fully ionized at an early stage of laser irradiation. Similarly, since the laser intensity required to ionize hydrogen atoms and generate  $\text{H}^+$  is  $I_a = 1.4 \times 10^{14}$  W/cm<sup>2</sup>, the ambient hydrogen atoms should be fully ionized at an early stage of laser irradiation. Therefore, a fully ionized plasma is employed as the initial condition because it does not affect the entire interaction dynamics. Moreover, the collisional relaxation process is ignored and the plasma is treated as collisionless since the collision mean free path is quite large ( $\sim$ m), and the time scale of the collisional relaxation ( $\sim$ nanosecond) is much longer than that of the cluster expansion ( $\sim$ picosecond).

Here, we have studied the laser-cluster interaction using 2D simulation, because the three-dimensional (3D) dynamics of interaction between a laser pulse and a spherical cluster and related phenomena are nearly spherically symmetric. Therefore, they exhibit one-dimensional (1D) feature in the radial direction. However, when we use spherical-coordinate system as 1D simulations, it cannot represent an interaction process between a circularly or linearly polarized laser pulse and a cluster. On the other hand, when we use rectangular coordinate system as 1D simulations, the laser pulse cannot interact the rear side of the cluster because the laser pulse is prevented from coming around behind the cluster due to the boundary conditions in the perpendicular direction.

In both cases, laser-cluster interactions cannot be properly modeled. Namely, simulation results in 1D simulations are essentially different from those in 2D or 3D simulations. Accordingly, in order to represent laser-cluster interactions and resultant dynamics, we chose 2D simulations, which can reproduce essential ingredients of a 3D

## 4.2. DYNAMICS OF BOUNDARY LAYER IN BETWEEN CLUSTER AND AMBIENT GAS

### Two-dimensional configuration

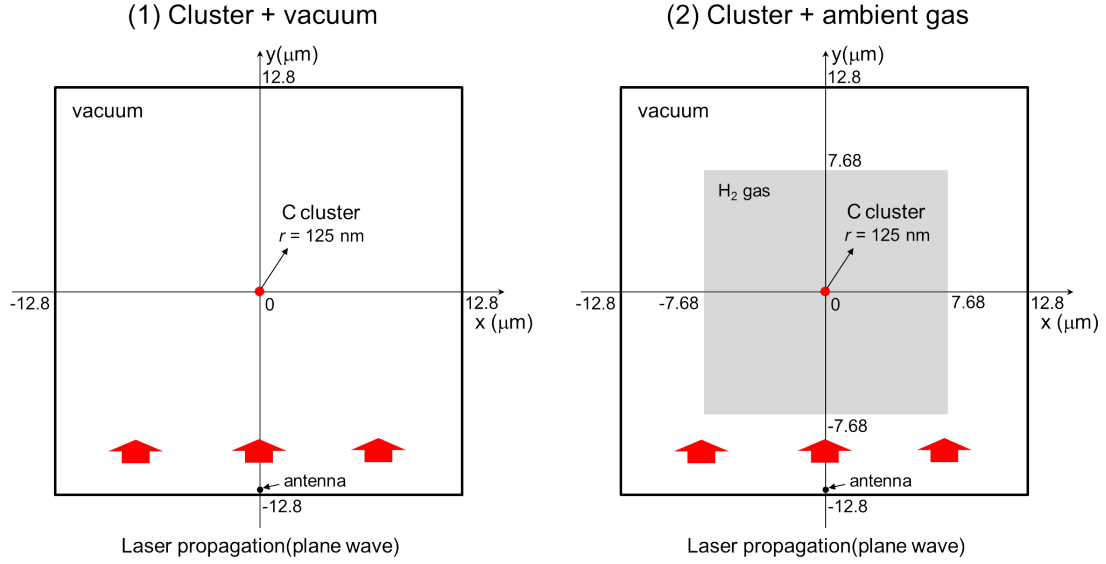


Figure 4.1: Two dimensional configurations for (1) cluster+vacuum case and (2) cluster+ambient gas case. A cluster is located at the center of the system. In case (2), ambient gas is initially removed from the cluster area. In both cases, laser irradiation occurs at  $t = 0$  fs and the laser pulse propagates in the  $+y$  direction.

Table 4.1: System parameters

species	values or conditions
$x$	$-12.8 \leq x \leq 12.8 \mu\text{m}$
$y$	$-12.8 \leq y \leq 12.8 \mu\text{m}$
Mesh numbers $N_x$	2560
Mesh numbers $N_y$	2560
Grid size $\Delta_x$	10 nm
Grid size $\Delta_y$	10 nm
Time step $\Delta t$	$6.67 \times 10^{-18}$ fs
Boundary conditions	transparent in $x$ and $y$ directions for both particles and fields

## 4.2. DYNAMICS OF BOUNDARY LAYER IN BETWEEN CLUSTER AND AMBIENT GAS

---

Table 4.2: Cluster medium (Cluster+Ambient gas)

species	values
Cluster species	Carbon
Cluster radius	125nm
Cluster ion density	$6.3 \times 10^{22} \text{ cm}^{-3}$
Cluster electron density	$3.8 \times 10^{23} \text{ cm}^{-3}$
Particle numbers (Cluster ions)	2,453,000
Gas species	Hydrogen
Gas ion density	$4.0 \times 10^{19} \text{ cm}^{-3}$
Gas electron density	$4.0 \times 10^{19} \text{ cm}^{-3}$
Gas area	$-7.68 \leq (x, y) \leq 7.68 \mu\text{m}$
Particle numbers (Gas ions)	7,334,000

Table 4.3: Laser parameters

species	values
Laser type	pulse laser (Gaussian)
Peak intensity	$1.0 \times 10^{19} \text{ W cm}^{-2}$
Normalized amplitude	$a_0 = 2.19$
Wavelength	$0.81 \mu\text{m}$
Critical density	$1.7 \times 10^{21} \text{ cm}^{-3}$
Pulse width	33 fs (Full Width at Half Maximum)
Antenna position	$-12.78 \mu\text{m}$
Polarization	Linearly polarized (P)
Propagation	$+y$ direction
Electric field	$x$ direction
Magnetic field	$z$ direction

simulation. However, it is noted that the electrostatic potential energy contained in the system is finite in the 3D case, while in the 2D case, as discussed in refs. [13, 119], it shows a logarithmic divergence. Therefore, for instance, the accelerated ion energy is found to become slightly higher in the 2D case than that in the 3D case.

### 4.2.2 Overview of the dynamics of boundary layer

Here, we present the overall dynamics of the boundary layer generated by the interaction between cluster and ambient gas. The simulation system is shown in Fig. 4.1(2). Simulation parameters are shown in Table 4.1 (system parameters), Table 4.2 (target parameters) and Table 4.3 (laser parameters). Figures 4.2(a)-4.2(d) show the 2D images for the charge density distributions of the cluster electrons  $\rho_{e,cl}$ , the cluster ions  $\rho_{i,cl}$  ( $C^{6+}$ ), the ambient gas electrons  $\rho_{e,ag}$ , and the ambient gas ions  $\rho_{i,ag}$  ( $H^+$ ) at  $t = 86.7$  fs, which is the time that the peak of the laser pulse reaches the center of the cluster. Note that prior to this time the interaction between the laser pulse and the cluster has taken place approximately from  $t = 40$  fs, which is the time that the leading edge of the laser pulse reaches the center of the cluster. A significant amount of electrons are found to be expelled from the peripheral region of the cluster and moves forward ( $+y$  direction) with a figure eight motion by the Lorenz force,  $\mathbf{v} \times \mathbf{B}$  as seen in Fig. 4.2(a). Here, the radius of the figure eight motion is represented by the electron excursion length  $\xi_e = 147$  nm at the peak of the laser pulse ( $a_0 = 2.19$ ). Note that the peripheral region is determined by the collisionless electron skin depth  $\delta_e \sim 25$  nm. Consequently, an electric field is produced outward around the contact surface between the cluster ions and those of the ambient gas. Therefore, the front of cluster ions and that of ambient gas ions are suffered from the same electric field, and are accelerated outward, i.e., the expansion of the cluster and the compression of the ambient gas, with keeping the contact surface. This feature can be seen in Figs. 4.2(c) and 4.2(d). Note that the process is similar to the cluster expansion into a vacuum by the irradiation of the laser field [13]. However, due to the presence of ambient gas electrons, the intensity of the electric field is weakened, so that the velocity of the cluster expansion in the ambient gas is smaller than that in the vacuum as we explain in Figs. 4.6 and 4.20. In the following, we describe the dynamics around the contact surface, which is a kind of *boundary layer* in between two distinct media, i.e., two distinct collisionless plasmas in the present case, after the laser pulse passes through the cluster.

Figures 4.3(a)-4.3(o) show the 2D images for  $\rho_{e,cl}$ ,  $\rho_{e,ag}$ , and  $\rho_{i,cl}$ ,  $\rho_{i,ag}$  at  $t = 133$  fs, 200 fs, 300 fs and 500 fs, respectively. In order to clearly see the dynamics of the boundary layer, we also show 1D cross sectional views for the charge density distributions of ions ( $\rho_{i,cl}$  and  $\rho_{i,ag}$ ) and electrons ( $\rho_{e,cl}$  and  $\rho_{e,ag}$ ) for the cluster and the ambient gas, and the resulting electric field  $E_y$  along the  $+y$  direction from the cluster center in Figs. 4.4(a)-4.4(d). This is due to the fact that the dynamics of the cluster and the ambient gas are approximately spherically symmetric as seen in Figs. 4.3(h)-4.3(o). Here, we found that the dynamics of the boundary layer can be categorized into three successive phases. Namely, the phase 1 that a contact surface exists, the phase 2 that an overlapping region between two plasmas appears, and the phase 3 that a rarefaction wave is induced in the

## 4.2. DYNAMICS OF BOUNDARY LAYER IN BETWEEN CLUSTER AND AMBIENT GAS

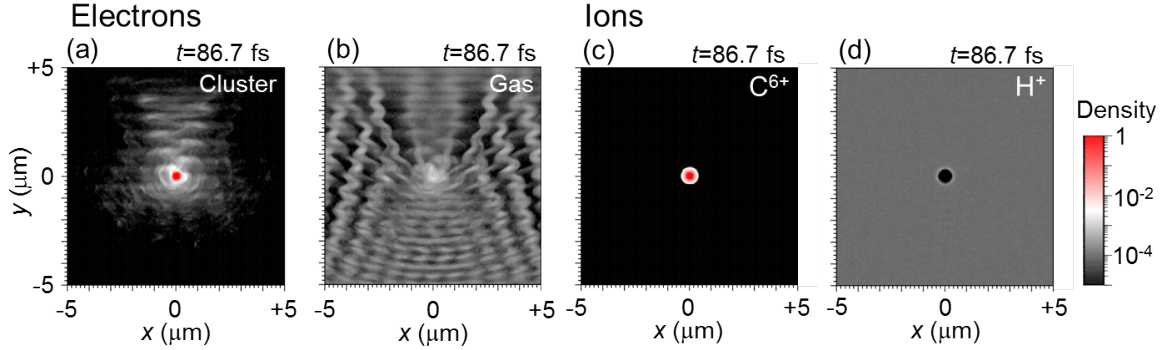


Figure 4.2: The 2D images for the charge density distributions of (a) the cluster electrons  $\rho_{e,cl}$ , (b) the ambient gas electrons  $\rho_{e,ag}$ , (c) the cluster ions  $\rho_{i,cl}$  and (d) the ambient gas ions  $\rho_{i,ag}$  at  $t = 86.7$  fs. Densities are normalized by the initial charge density of the cluster ions and displayed on a log scale.

ambient gas ions.

### (1) Phase 1 ( $86.7 \text{ fs} \leq t \leq 150 \text{ fs}$ ):

This is the phase that the contact surface exists during the dynamics of the expansion of the cluster ions and the compression of the ambient gas ions as shown in Figs. 4.3(h) and 4.3(l), which exhibits essentially the same structure as that established in earlier time, i.e.,  $t = 86.7$  fs, as discussed in Figs. 4.2(c) and 4.2(d). From the 1D cross sectional view, this feature can be clearly seen in Fig. 4.4(a). The ambipolar electric field  $E_{y1}$ , which is similar to the field produced by the cluster expansion into the vacuum, is produced around the contact surface. The detailed data analysis confirms that the peak intensity of the field  $E_{y1}$  in the present case with the ambient gas becomes slightly small compared with that in the case without the ambient gas. From the electron density  $\rho_{e,ag}$ , we found that the electrons of the ambient gas flow into the cluster, which weakens the charge separation around the peripheral region of the cluster as shown in Fig. 4.2(b) and blue dotted line in Fig. 4.4(a). The decrease in the field  $E_{y1}$  leads to the decrease in the cluster expansion velocity as seen in Fig. 4.6, which represents the cluster front in the case without ambient gas (black dotted line) and in the case with ambient gas (black solid line). In high density cases of the ambient gas, the effect of the ambient gas density becomes clearer, as discussed later. Moreover, it is interesting that a small gap exist in between the cluster expansion front and the compressed surface (at  $y = 1.1 \mu\text{m}$ ) as shown in Fig. 4.4(a). This is because the ambient gas ions  $\text{H}^+$  are more accelerated by the field  $E_{y1}$  than the cluster ions  $\text{C}^{6+}$  due to the difference of the charge to mass ratio, i.e., 1 for  $\text{H}^+$  and  $1/2$  for cluster ions  $\text{C}^{6+}$ .

### (2) Phase 2 ( $150 \text{ fs} \leq t \leq 340 \text{ fs}$ ):

This is the phase that the crossing between the cluster expansion front and the compressed surface takes place and an overlapping region evolves. Initially, the charge density of the cluster ions at the contact surface is higher than that of the ambient gas

## 4.2. DYNAMICS OF BOUNDARY LAYER IN BETWEEN CLUSTER AND AMBIENT GAS

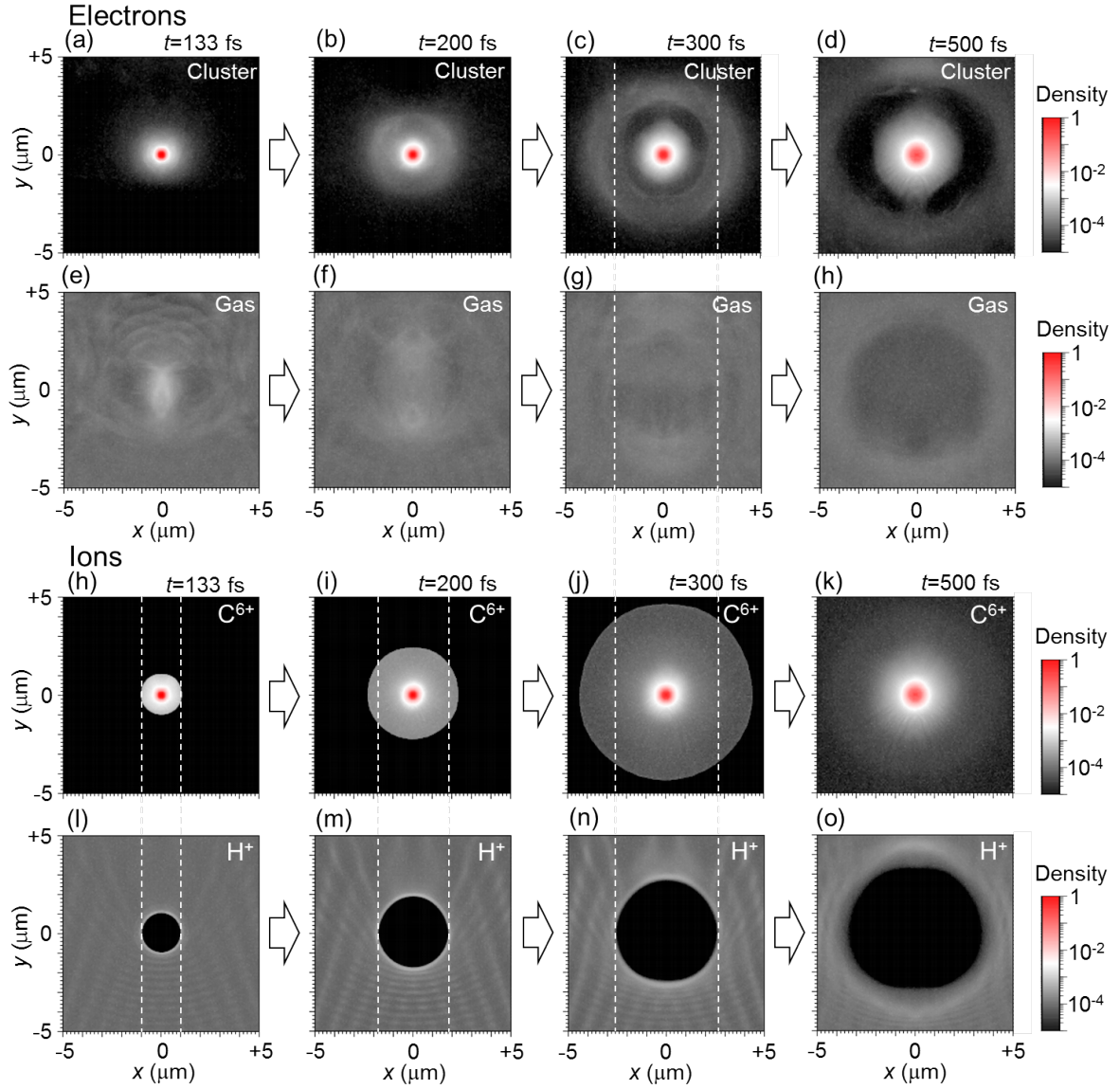


Figure 4.3: The 2D images for the charge density distributions of (a), (b), (c), (d) the cluster electrons  $\rho_{e,cl}$ , (e), (f), (g), (h) the ambient gas electrons  $\rho_{e,ag}$ , (i), (j), (k) the cluster ions  $\rho_{i,cl}$  and (l), (m), (n), (o) the ambient gas ions  $\rho_{i,ag}$  at (a), (e), (h), (l)  $t = 133$  fs, (b), (f), (i), (m)  $t = 200$  fs, (c), (g), (j), (n)  $t = 300$  fs and (d), (h), (k), (o)  $t = 500$  fs. Densities are normalized by the initial charge density of the cluster ions and displayed on a log scale. White dashed lines show positions of the compressed surface of the ambient gas ions in the  $x$  direction.

## 4.2. DYNAMICS OF BOUNDARY LAYER IN BETWEEN CLUSTER AND AMBIENT GAS

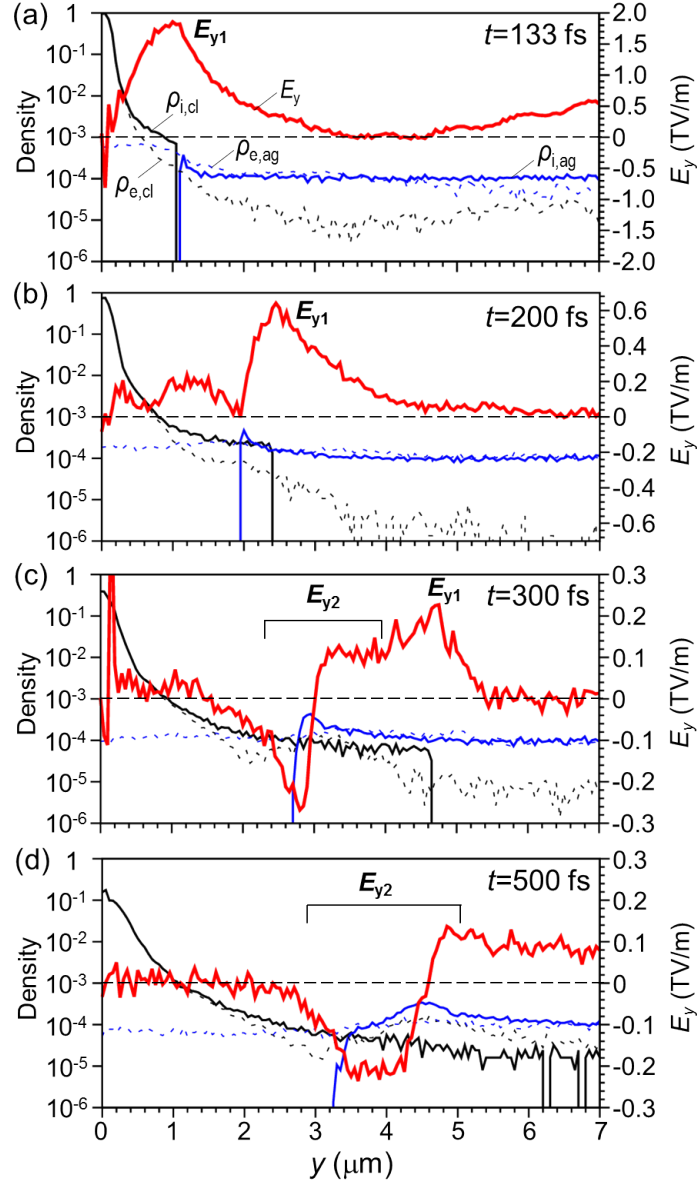


Figure 4.4: (a)-(d) 1D cross sectional views for the charge density distributions of cluster ions  $\rho_{i,cl}$  (black solid line), ambient gas ions  $\rho_{i,ag}$  (blue solid line), cluster electrons  $\rho_{e,cl}$  (black dotted line), ambient gas electrons  $\rho_{e,ag}$  (blue dotted line), and the resulting electric field  $E_y$  (red solid line) along the  $+y$  direction from the center of the cluster at (a)  $t = 133$  fs, (b)  $t = 200$  fs, (c)  $t = 300$  fs and (d)  $t = 500$  fs. Densities are normalized by the initial density of the cluster ions.

## 4.2. DYNAMICS OF BOUNDARY LAYER IN BETWEEN CLUSTER AND AMBIENT GAS

---

ions in phase 1. Since electron temperature is relatively high, the density distribution of electrons around the contact surface is not localized but approximately uniform [see Figs. 4.4(a) and 4.4(b)]. Therefore, the discontinuity of charge density between the cluster ions and the ambient gas ions always produces the field  $E_{y1}$ . However, as time goes on, the discontinuity gradually becomes flat due to the compression of the ambient gas. As a result, the field  $E_{y1}$  is reduced and ambient gas ions start to pass over the electrostatic potential hill associated with the field  $E_{y1}$ , leading to the overlapping region between cluster and ambient gas. Namely, it is considered that the crossing is triggered when the density of the cluster ions and that of the ambient gas ions roughly coincide. We found that this condition is fulfilled in the wide range of ambient gas density.

The overlapping region, which results from the crossing, is found to develop with time [see Figs. 4.3(i) and 4.3(m), 4.3(j) and 4.3(n)]. During the development process of the overlapping region, the structure of the electric field  $E_y$  also evolves in a qualitatively different manner: Namely, a dip structure in the electric field emerges at the left-hand side of the compressed surface ( $y = 2.0 \mu\text{m}$ ), which results from the net positive charge of the compressed surface as seen in Fig. 4.4(b). Subsequently, in addition to the ambipolar electric field  $E_{y1}$ , a bipolar electric field  $E_{y2}$  is established around the compressed surface as seen in Fig. 4.4(c). Note that the sharp gradient in the field  $E_{y2}$  exhibits a nature of the boundary layer. Moreover, as the result of such an evolution of the electric field structure [Figs. 4.4(a)-4.4(c)], electrons accumulate around the compressed surface and a ring-like structure, which corresponds to the density hump at around  $y = 3.0 \mu\text{m}$  in Fig. 4.4(c), is formed as seen in Figs. 4.3(c) and 4.3(d). The structure is considered to be connected to the establishment of kinetic equilibrium, which we discuss the details in later.

### **(3)Phase 3 ( $340 \text{ fs} \leq t$ ):**

This is the phase that the sharp structure of the compressed surface tends to be relaxed [Fig. 4.3(o)] and evolve as a *rarefaction wave*. This feature can be confirmed by the structure of the compressed surface at around  $3.4 \leq y \leq 4.6 \mu\text{m}$  in Fig. 4.4(d). We also show the time evolution of the density profile of ambient gas ions in Fig. 4.5. The sharp structure of the compressed surface (before  $t = 300 \text{ fs}$ ) starts to be relaxed as the rarefaction wave from  $t = 340 \text{ fs}$ . During the propagation of the rarefaction wave, generally, a high density part and a low density part are connected with a point of constant density (see Fig. 4.18,  $y = 1.3 \mu\text{m}$ ). In the present case, it is noted that the point of constant density is moving in the  $+y$  direction. The high density part propagates in the  $+y$  direction with a velocity of  $0.026c = 1.35c_s$ , where  $c_s$  is the ion-acoustic velocity. The onset of the rarefaction wave is defined by the end of acceleration of ambient gas ions at the compressed surface from phase space distribution of ambient gas ions, which is discussed later. Simultaneously, a staircase structure emerges gradually in the density profile of the expanding cluster [see around  $y = 4.5 \mu\text{m}$  in Fig. 4.4(d)].

These results indicate that the formation of structure in the cluster ions and the destruction of the ambient gas structure occur in pairs. In terms of the entropy conservation derived from the nature of a collisionless plasma, the increase in entropy resulting from the destruction of the compressed surface is counterbalanced by the

## 4.2. DYNAMICS OF BOUNDARY LAYER IN BETWEEN CLUSTER AND AMBIENT GAS

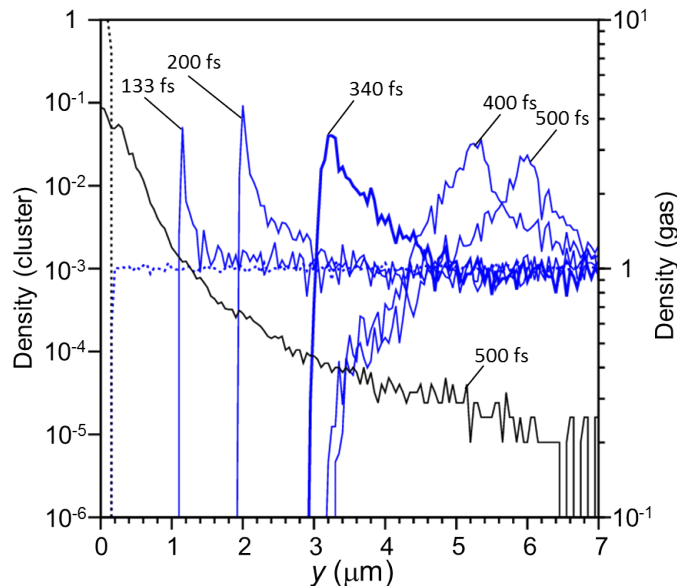


Figure 4.5: The time evolution of charge density distributions of cluster ions (black solid line) and ambient gas ions (blue solid line). Dotted lines show the initial charge density distributions of cluster ions (black) and ambient gas ions (blue).

decrease in entropy resulting from the structure formation in the cluster. This phenomenon is clearly observed when we increase the density of the ambient gas.

Here, in order to grasp the positional relation between the cluster expansion front and the compressed surface, we show the schematic views concerning spatial evolutions of the charge densities of cluster ions ( $\rho_i^{cl}$ ) and ambient gas ions ( $\rho_i^{ag}$ ), and the phase space distributions of cluster ions and ambient gas ions at representative times in Fig. 4.7. Figures 4.7(a1)-4.7(f1) show the density of cluster ions (black solid lines) and ambient gas ions (blue solid lines) as a function of  $y$  in the  $+y$  direction from the cluster center. The phase space distributions of cluster ions (green heavy lines) and ambient gas ions (red heavy lines) corresponding to 4.7(a1)-4.7(f1) are shown in 4.7(a2)-4.7(f2).

Figures 4.7(a1), 4.7(b1) and 4.7(c1) correspond to *Phase 1*. In this phase, cluster ions expand and compress ambient gas ions with keeping the contact surface. In the laboratory frame, the compressed surface of ambient gas moves in the  $+y$  direction [see Figs. 4.7(a1)-4.7(c1)]. However, the velocities of ambient gas ions which compose the compressed surface are not same. Namely, the ambient gas ions on the compressed surface continuously switch places [see Figs. 4.7(a2)-4.7(c2)]. It is noted that a small gap between the cluster expansion front and the compressed surface of the ambient gas exists due to the difference of the charge to mass ratio  $q/m_i$ , i.e., 1 for ambient gas ions  $H^+$  and  $1/2$  for cluster ions  $C^{6+}$  [see Fig. 4.7(b1)].

Figure 4.7(d1) corresponds to *Phase 2*. In this phase, the cluster expansion front overtakes the compressed surface and the mixing between cluster ions and ambient gas ions [see Fig. 4.7(d1)]. Figures 4.7(e1) and 4.7(f1) correspond to *Phase 3*. In this phase,

## 4.2. DYNAMICS OF BOUNDARY LAYER IN BETWEEN CLUSTER AND AMBIENT GAS

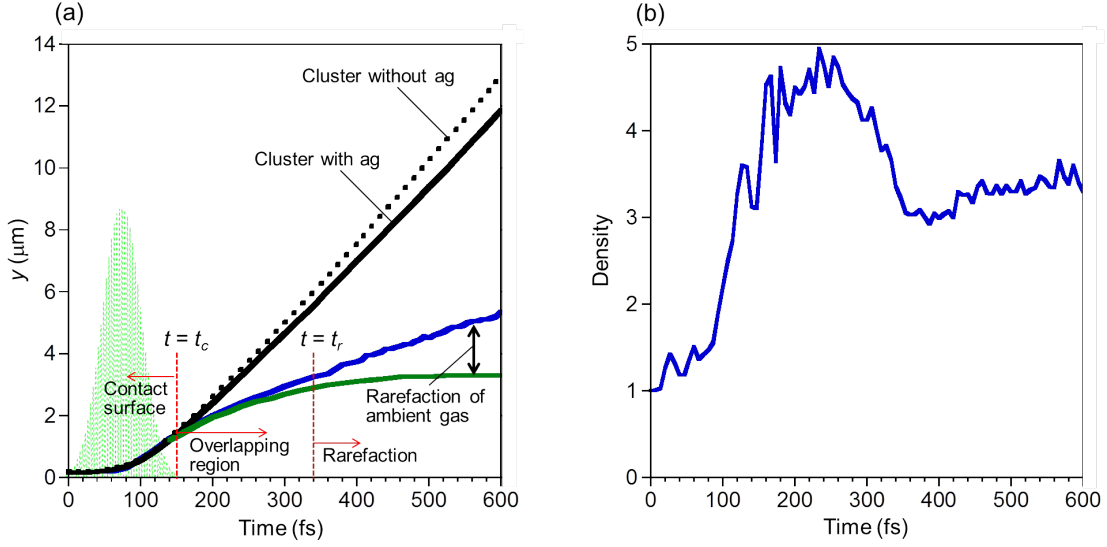


Figure 4.6: (a) Temporal evolutions for the Coulomb expansion front of the cluster ions (black solid line), the compressed surface of the ambient gas ions (blue and green solid lines). The black dashed line represents the temporal evolution for the Coulomb explosion front of the cluster ions in a vacuum as a reference. The green dotted line represents the intensity of the laser pulse. The pulse peak passes through the center of the cluster at  $t = 86.7$  fs. (b) The maximum value of the charge density of the ambient gas ions around the compressed surface  $\rho_{i,ag}^{max}$  along the  $+y$  direction from the center of the cluster. Note that the sharp structure of the compressed surface evolves after  $t = 200$  fs, i.e., the peak density part (blue solid line) and the low density surface (green solid line). The density is normalized by the initial charge density of the ambient gas ions.

the compressed surface collapses as a rarefaction wave. As the rarefaction wave evolves, the distance between the position exhibiting the peak intensity ( $r_{f(B)}^{ag}$ ) and the front ( $r_{f(D)}^{ag}$ ) becomes large [see Figs. 4.7(e1)-4.7(f1)]. Simultaneously, cluster ions inside the rarefaction wave decrease the speed [see Figs. 4.7(e2) and 4.7(f2)] and a staircase structure is formed in the density distribution of the cluster ions [see Fig. 4.7(f1)].

Temporal evolutions for the cluster expansion front and the compressed surface are shown in Fig. 4.6(a). The position of the cluster expansion front in a vacuum, i.e., a single carbon cluster without ambient gas, is also shown as a reference. As discussed in the above, the interaction process between the cluster and the ambient gas is categorized into three phases: (1) In phase 1 ( $86.7 \text{ fs} \leq t \leq t_c \sim 150 \text{ fs}$ ), the cluster expansion front with the velocity  $v_{ce}$  and the compressed surface with the velocity  $v_{ag}$  move outward together, i.e.,  $v_{ce} \simeq v_{ag}$ . (2) In phase 2 ( $t_c \leq t \leq t_r \sim 340 \text{ fs}$ ), the cluster expansion front moves ahead of the compressed surface, i.e.,  $v_{ce} > v_{ag}$ . The overlapping region develops with the relative velocity,  $v_{ce} - v_{ag}$ . (3) In phase 3 ( $t_r \leq t$ ), the compressed surface starts to evolve as the rarefaction wave. That is, a steep structure of the compressed surface gradually tends to be relaxed, exhibiting a convex structure, i.e.,  $d^2 \rho_{i,ag} / dy^2 < 0$  and starts to slowly

## 4.2. DYNAMICS OF BOUNDARY LAYER IN BETWEEN CLUSTER AND AMBIENT GAS

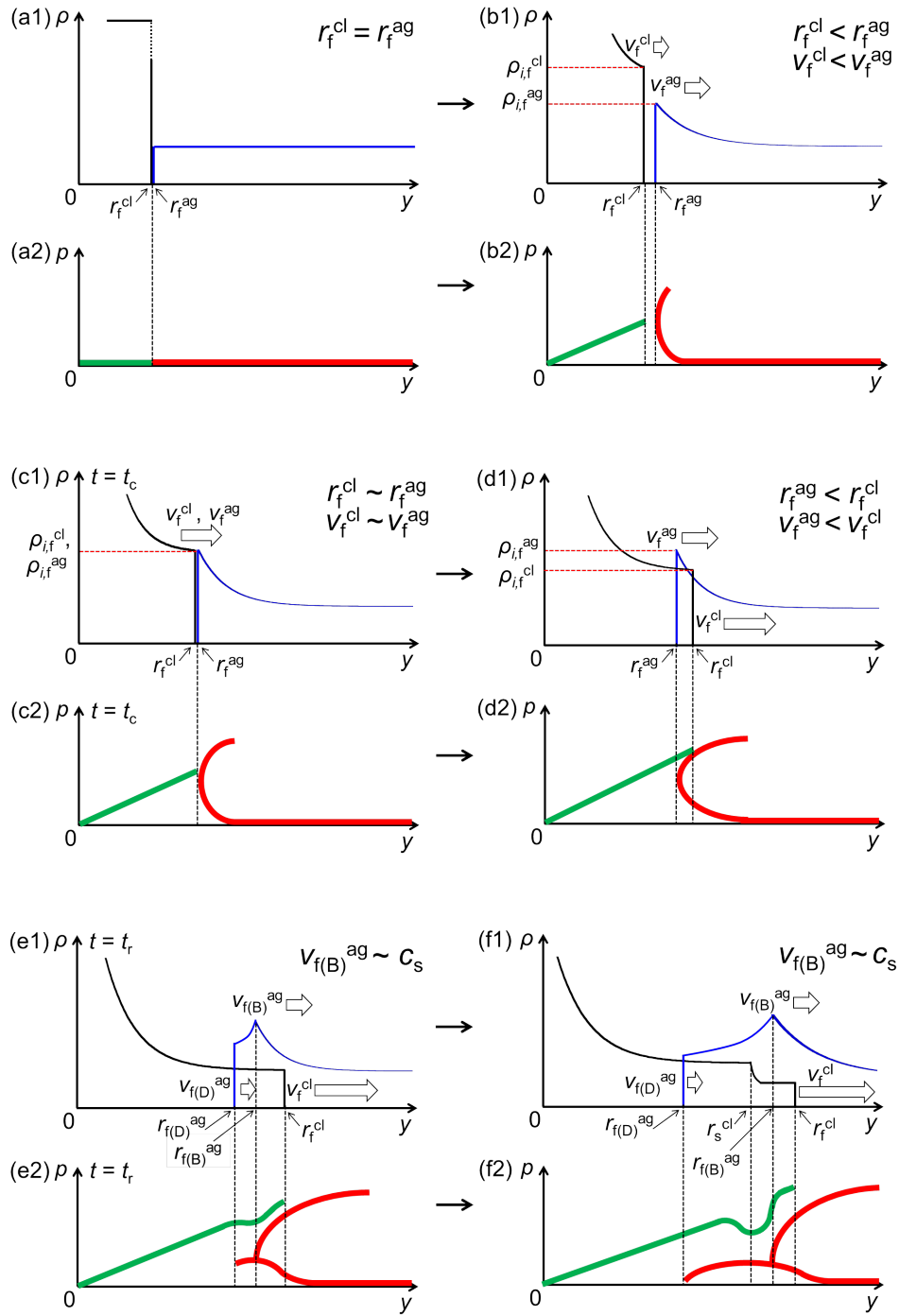


Figure 4.7: (a1)-(f1) Schematic views of the density distribution of cluster ions (black solid lines) and ambient gas ions (red solid lines). Schematic views of the phase space distributions of cluster ions (green thick lines) and ambient gas ions (red thick lines) correspond to (a1)-(f1) are also shown in (a2)-(f2).

## 4.2. DYNAMICS OF BOUNDARY LAYER IN BETWEEN CLUSTER AND AMBIENT GAS

---

collapse with time. In this phase, the distance between the peak density part (blue solid line) and the lowest density part (green solid line) becomes large with time.

Figure 4.6(b) shows the maximum value of the charge density of the ambient gas ions around the compressed surface  $\rho_{i,ag}^{max}$ . Here, the density  $\rho_{i,ag}^{max}$  keeps increasing even at around  $t = t_c$ , reaches a maximum value at around  $t = 250$  fs, and then gradually decreases, reaching a constant value at around  $t = 360$  fs. The evolution of the density  $\rho_{i,ag}^{max}$  and the associated formations of the nonlinear wave play an important role in triggering the transition and the subsequent dynamics of the boundary layer leading to a quasi-steady state with a kinetic equilibrium, which cannot be seen in the exploding cluster dynamics in a vacuum.

### 4.2.3 Ion acceleration by nonlinear waves

In this subsection, we discuss the acceleration mechanisms of ambient gas ions using phase space distributions. Figures 4.8-4.10 show the 1D cross sectional views for the electric field  $E_y$  and the electrostatic potential for ions (a), the charge density and the phase space distributions of the cluster ions (b) and the ambient gas ions (c). The phase space distributions of ions are also shown in (b) and (c).

#### (1) Acceleration by a collisionless shock:

In phase 1 ( $t \leq t_c$ ), as shown in Figs. 4.8(a)-4.8(c), a collisionless shock (electron-ion collisional mean free path  $\gg$  shock thickness) is launched near the contact surface. The ambient gas ions are compressed and reflected back by the shock potential associated with the ambipolar electric field  $E_{y1}$  at the contact surface:

At  $t = 133$  fs, the propagation velocity of the shock front is  $v_{sh} = 0.060c$  ( $1.8 \times 10^7$  m/s), while the ion-acoustic velocity, defined as

$$c_s = \sqrt{\frac{\gamma(ZT_e + T_i)}{m_i}}, \quad (4.5)$$

is calculated as  $c_s = 0.029c$  ( $8.7 \times 10^6$  m/s) at  $y = 7 \mu\text{m}$ , where  $\gamma$  is  $(N + 2)/N$  and  $N$  is degrees of freedom,  $Z$  is the ion charge state,  $T_e$  and  $T_i$  are the temperatures of electrons and cluster ions, respectively, and  $m_i$  is the mass of ion. In this case,  $N = 2$  (for two dimension),  $Z = 1$  (for proton) and  $m_i = 938$  (MeV/ $c^2$ ) (for proton). Then, the calculated shock Mach number is  $M_{sh} = 2.1$ , which exceeds the critical value for the collisionless shock acceleration [116]. In principle, the shock front can accelerate upstream ions, i.e., the ambient gas ions in the present case, by reflecting them to double the shock velocity when the kinetic energy of the incoming ambient gas ions is less than the shock potential in the shock-rest frame, and generates ion beams with a narrow energy spread [55, 56]. Indeed, since the kinetic energy of the incoming ions  $K_{ion} = 1/2m_i(v_{sh} - v_{exp})^2 = 0.96m_e c^2 = 0.51$  MeV, where  $v_{exp}$  is the expansion velocity of the upstream ambient gas ions accelerated by the TNSA space-charge field created in front of the shock [58], is smaller than the potential of the shock  $e\Phi = 1.6m_e c^2 = 0.78$  MeV, the ambient gas ions should be reflected. As the shock propagates, the ambient gas ions are reflected back and gain the velocity corresponds to  $v_{ion} = 2v_{sh} - v_{exp} = 0.092c$  ( $2.7 \times 10^7$  m/s) [Fig. 4.8(c)]. Detailed data analysis confirms that the shock structure survives up to  $t = t_c$ , so that the shock acceleration of the ambient gas ions continues up to  $t = t_c$ . Until this time, the intensity of the field  $E_{y1}$ , and therefore, the potential height associated with the shock, rapidly decrease with the time scale of around 19 fs due to the significant expansion of the plasma, while the kinetic energy of incoming ions is still less than the shock potential, i.e.,  $e\Phi > K_{ion}$ .

Figure 4.12(a) shows the resulting energy spectrum of the reflected ions at  $t = 133$  fs

## 4.2. DYNAMICS OF BOUNDARY LAYER IN BETWEEN CLUSTER AND AMBIENT GAS

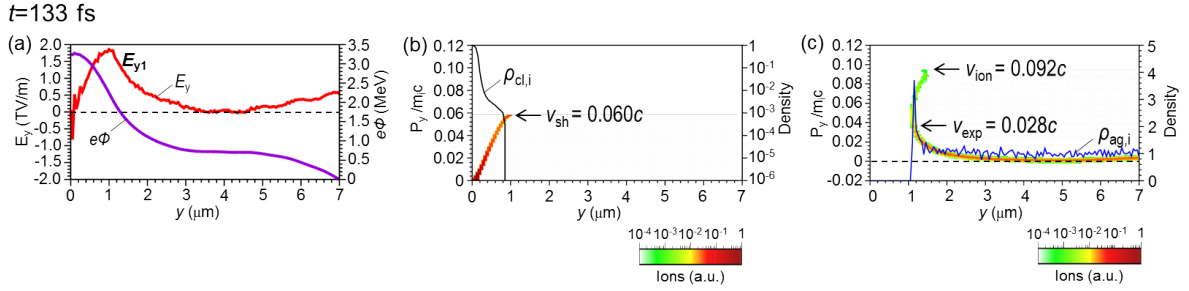


Figure 4.8: The 1D cross sectional views for (a) the electric field  $E_y$  (red solid line) and the electrostatic potential for ions  $e\Phi$  (purple solid line), (b) the charge density  $\rho_{i,cl}$  (black solid line) and the phase space distributions of the cluster ions, (c) the charge density  $\rho_{i,ag}$  (blue solid line) along the  $+y$  direction from the center of the cluster at  $t = 133$  fs. Electrostatic potentials are set to zero at  $y = 7 \mu\text{m}$ . Charge densities are normalized by the initial density of ions. Phase space distributions consist of ions in the region of  $y \geq 0$  and  $-0.15 \leq x \leq +0.15 \mu\text{m}$ , and are normalized by the initial charge density of the cluster ions and displayed on a log scale.

when the shock acceleration is dominant. The reflected ion energies exceed the maximum energy of the Coulomb exploded ions. Although  $v_{sh}$  keeps almost a constant value [Fig. 4.6(a)], the broad energy spectrum is produced. This is because the reflected ions are further accelerated in the rear side sheath field, i.e., the front part of the ambipolar electric field  $E_{y1}$ , introducing a chirp in  $v_{ion}$  [58].

### (2) Acceleration by a nonlinear wave:

In phase 2 ( $t_c \leq t \leq t_r$ ), the ambient gas ions start to pass over the potential created by the field  $E_{y1}$  because the intensity of the field  $E_{y1}$  associated with the shock continues to decrease with time. Indeed, at  $t = 153$  fs, the kinetic energy of the incoming ions  $K_{ion} = 1/2m_i(v_{sh} - v_{exp})^2 = 0.96m_e c^2 = 0.48$  MeV becomes larger than the potential  $e\Phi = 0.94m_e c^2 = 0.47$  MeV. Consequently, shock acceleration terminates. Instead, the compressed surface propagates in the  $+y$  direction as a *nonlinear wave*, which also causes a similar ion acceleration as that of the shock. Namely, an additional potential wall is formed by the bipolar electric field  $E_{y2}$  associated with the nonlinear wave [Fig. 4.9(a)], which reflects back part of the incoming ambient gas ions [Fig. 4.9(c)].

Indeed, at  $t = 300$  fs, the velocity of the nonlinear wave is  $v_{nw} = 0.022c$  ( $6.6 \times 10^6$  m/s), while the calculated ion-acoustic velocity is  $c_s = 0.020c$  ( $6.0 \times 10^6$  m/s) at  $y = 7 \mu\text{m}$ , leading to a Mach number of the nonlinear wave  $M_{nw} = 1.1$ , which falls below the critical value for shock acceleration [116] [Figs. 4.9(a)-4.9(c)]. Since the kinetic energy of the incoming ions  $K_{ion} = 1/2m_i(v_{nw} - v_{exp})^2 = 0.132m_e c^2 = 0.066$  MeV is larger than the potential of the nonlinear wave  $e\Phi = 0.088m_e c^2 = 0.044$  MeV, part of ambient gas ions pass over the potential wall associated with the field  $E_{y2}$ , while the rest of ions are reflected back and gain the velocity corresponds to  $v_{ion} = 2v_{nw} - v_{exp} = 0.034c$  ( $9.8 \times 10^6$  m/s) [Fig. 4.9(c)].

## 4.2. DYNAMICS OF BOUNDARY LAYER IN BETWEEN CLUSTER AND AMBIENT GAS

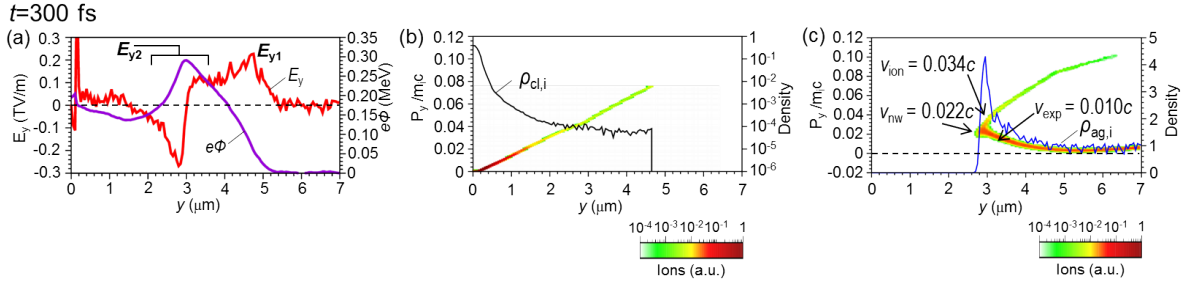


Figure 4.9: The 1D cross sectional views for (a) the electric field  $E_y$  (red solid line) and the electrostatic potential for ions  $e\Phi$  (purple solid line), (b) the charge density  $\rho_{cl,i}$  (black solid line) and the phase space distributions of the cluster ions, (c) the charge density  $\rho_{ag,i}$  (blue solid line) along the  $+y$  direction from the center of the cluster at  $t = 300$  fs. Electrostatic potentials are set to zero at  $y = 7 \mu\text{m}$ . Charge densities are normalized by the initial density of ions. Phase space distributions consist of ions in the region of  $y \geq 0$  and  $-0.15 \leq x \leq +0.15 \mu\text{m}$ , and are normalized by the initial charge density of the cluster ions and displayed on a log scale.

Figure 4.12(b) shows the resulting energy spectrum of the reflected ions at  $t = 300$  fs. Because  $v_{nw}$  slows down with time [Fig. 4.6(a)] while keeping the intensity of the field  $E_{y2}$  almost constant, the spectrum spans a wide energy range having a small hump at the higher energy side, which is a remnant of the early-stage limited energy spread spectrum due to the shock acceleration. This spectrum shape is consistent with that observed in the experiment [111].

### (3) Termination of acceleration:

In phase 3 ( $t_r \leq t$ ), the evolution of the compressed surface to the rarefaction wave is connected with the termination of acceleration of ambient gas ions. That is, a change of the ion orbit from the reflection phase to the pass over phase occurs at  $t = t_r$ . Indeed, at  $t = 500$  fs, the potential height associated with the field  $E_{y2}$  in Fig. 4.10(a) becomes low compared with that in Fig. 4.9(a). Resultantly, all incoming ambient gas ions pass over the potential wall [at  $y = 5.3 \mu\text{m}$ , Fig. 4.10(c)].

The change from the acceleration phase to the phase which the acceleration terminates is clearly observed in Fig. 4.11. At around  $t = t_r \sim 340$  fs, reflection of the upstream ambient gas ions at the compressed surface terminates. Moreover, in the cluster phase space distributions, the cluster ions at around the compressed surface are start to be decelerated from  $t = 340$  fs, which leads to the structure formation in the cluster density distribution.

Figure 4.12(c) shows the resulting energy spectrum of the reflected ions at  $t = 500$  fs. At this time, acceleration by nonlinear waves does not occur, while the spectrum spans a wide energy range having a small hump at the higher energy side, which is a remnant of the early-stage limited energy spread spectrum due to the shock acceleration. Not that the energy spectrum of the cluster ions has a step-like structure at around  $0.5 \text{ MeV/u}$ , which

## 4.2. DYNAMICS OF BOUNDARY LAYER IN BETWEEN CLUSTER AND AMBIENT GAS

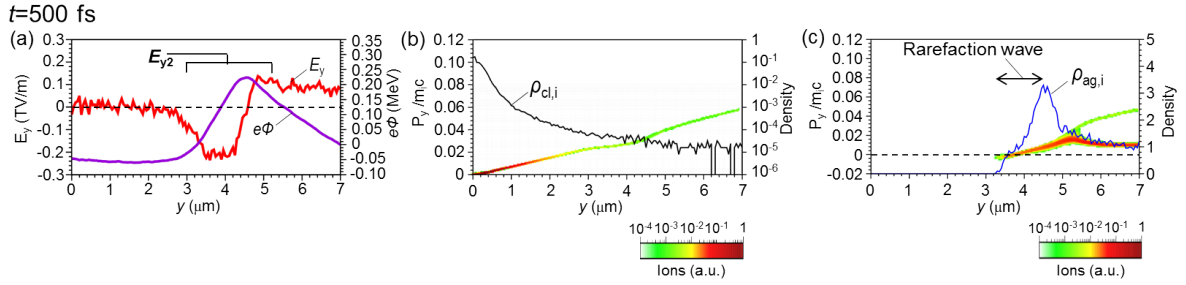


Figure 4.10: The 1D cross sectional views for (a) the electric field  $E_y$  (red solid line) and the electrostatic potential for ions  $e\Phi$  (purple solid line), (b) the charge density  $\rho_{i,cl}$  (black solid line) and the phase space distributions of the cluster ions, (c) the charge density  $\rho_{i,ag}$  (blue solid line) along the  $+y$  direction from the center of the cluster at (c)  $t = 500$  fs. Electrostatic potentials are set to zero at  $y = 7 \mu\text{m}$ . Charge densities are normalized by the initial density of ions. Phase space distributions consist of ions in the region of  $y \geq 0$  and  $-0.15 \leq x \leq +0.15 \mu\text{m}$ , and are normalized by the initial charge density of the cluster ions and displayed on a log scale.

results from the deceleration by the field  $E_{y2}$  in the process of the structure formation of the cluster.

## 4.2. DYNAMICS OF BOUNDARY LAYER IN BETWEEN CLUSTER AND AMBIENT GAS

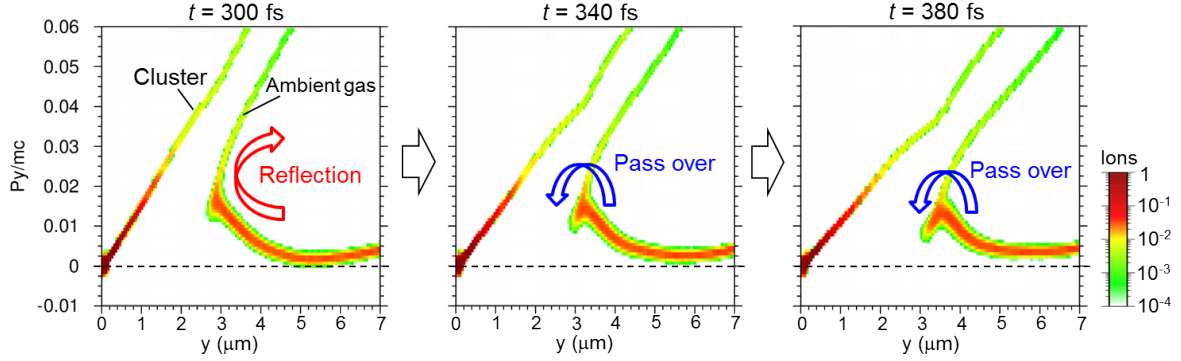


Figure 4.11: The phase space distributions of the cluster and ambient gas ions along the  $+y$  direction from the center of the cluster at (a)  $t = 300$  fs, (b)  $t = 340$  fs, and (c)  $t = 380$  fs. Charge densities are normalized by the initial density of ions. Phase space distributions consist of ions in the region of  $y \geq 0$  and  $-0.15 \leq x \leq +0.15 \mu\text{m}$ , and are normalized by the initial charge density of the cluster ions and displayed on a log scale.

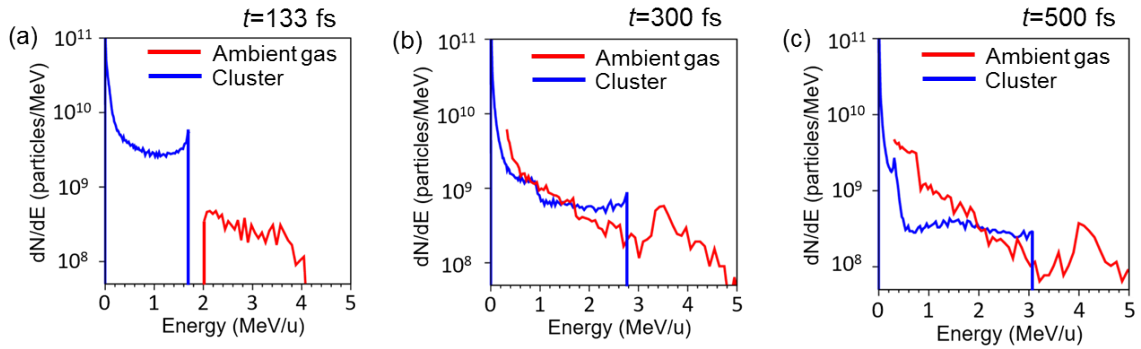


Figure 4.12: Energy spectra of the Coulomb expanding cluster ions (black solid line) and the reflected ambient gas ions (blue solid line) at (a)  $t = 133$  fs, (b)  $t = 300$  fs and (c)  $t = 500$  fs. The ion number is evaluated in real value by multiplying the particle weight to the PIC particle. Spectra consist of ions in the region of  $y \geq 0$  and  $-0.15 \leq x \leq +0.15 \mu\text{m}$ .

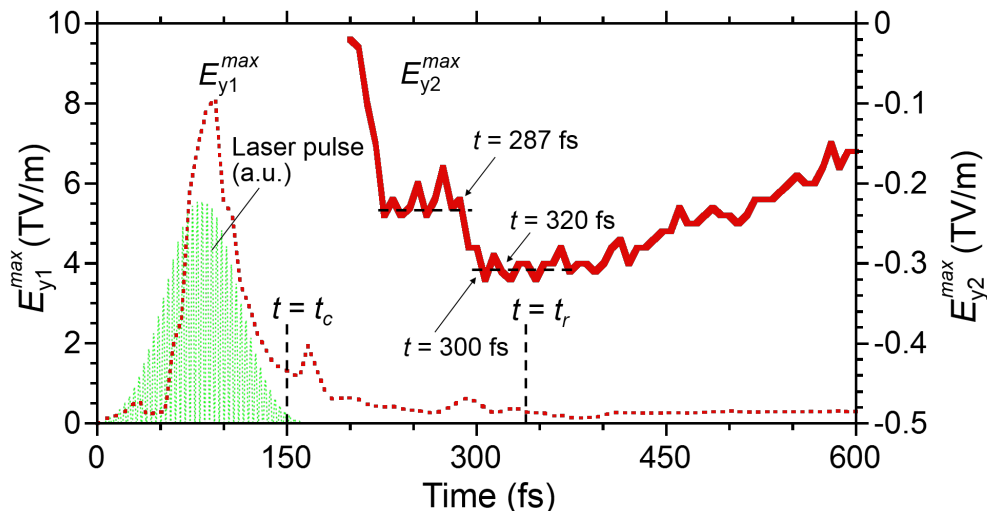


Figure 4.13: Temporal evolutions for the maximum value of the ambipolar electric field  $E_{y1}^{max}$  (red dotted line) associated with the shock wave and that of the bipolar electric field  $E_{y2}^{max}$  (red solid line) associated with the nonlinear wave including the kinetic equilibrium. The green solid line represents the intensity of the laser pulse. The pulse peak passes through the center of the cluster at  $t = 86.7$  fs.

#### 4.2.4 Formation of quasi-stationary kinetic equilibrium

In this section, we study the role of electron dynamics as shown in Figs. 4.14(a) and 4.14(b) at  $t = 133$  fs, 200 fs and 300 fs, which is a key leading to the bipolar electric field structure. At earlier times ( $t = 133$  fs and 200 fs), the potential  $-e\Phi$  (gray solid line) in Figs. 4.14(a1) and 4.14(a2) monotonically increases from  $y = 0 \mu\text{m}$ , resulting in the formation of the electron vortex which O-point is located at  $y = 0 \mu\text{m}$  as seen in Figs. 4.14(b1) and 4.14(b2).

Then, the potential  $-e\Phi$  evolves slowly and tends to have a deep well at  $y = \pm 2.9 \mu\text{m}$ , resulting in the formation of two electron vortices embedded in high energy passing electrons while keeping the vortex at  $y = 0 \mu\text{m}$  as seen in Fig. 4.14(b3). Note that only the region  $y \geq 0 \mu\text{m}$  is illustrated in Fig. 4.14. Namely, during the evolution from  $t = 200$  fs to  $t = 300$  fs, a separatrix which X-point is located at around  $y = \pm 1.6 \mu\text{m}$  is formed, exhibiting a topological change of electron trajectories as shown in Figs. 4.14(b2) and 4.14(b3).

Here, it is worthwhile to study the time scale that the topology of the electron trajectory changes. For this purpose, in Fig. 4.13, we show the time histories for the maximum value of the ambipolar field  $E_{y1}^{max}$  and the maximum negative value of the bipolar field  $E_{y2}^{max}$  which develops from the dip structure in the field  $E_y$ .

The value  $E_{y1}^{max}$  rapidly decreases until  $t \sim t_c$  during the shock wave survives, while it gradually decreases after  $t \sim t_c$ . On the other hand, the value  $E_{y2}^{max}$  starts to develop after  $t \sim 200$  fs. As the overlapping region between the Coulomb expansion front and

## 4.2. DYNAMICS OF BOUNDARY LAYER IN BETWEEN CLUSTER AND AMBIENT GAS

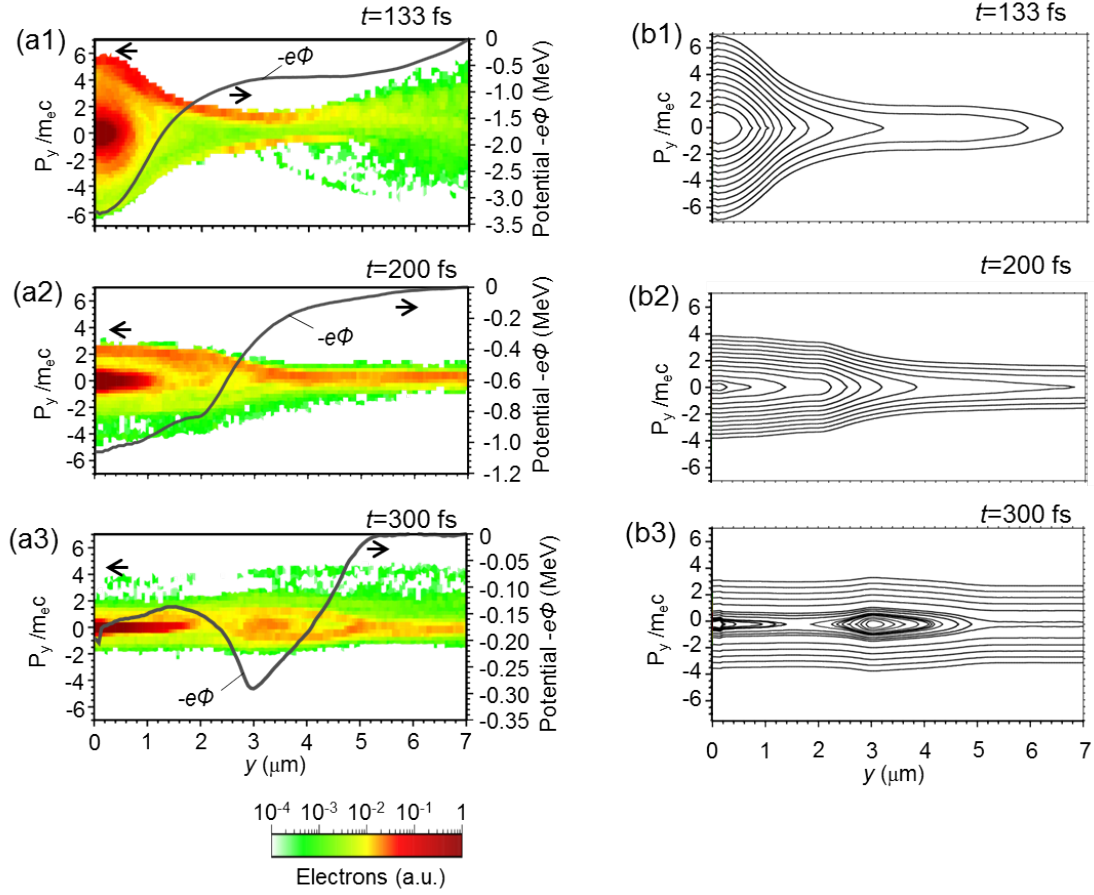


Figure 4.14: The 1D cross sectional views for (a1)-(a3) the phase space distributions of electrons and the electrostatic potential for electrons  $-e\Phi$  (gray solid line), and (b1)-(b3) the contour plots of electron trajectories along the  $+y$  direction from the center of the cluster at (a1), (b1)  $t = 133$  fs, (a2), (b2)  $t = 200$  fs, and (a3), (b3)  $t = 300$  fs. The electrostatic potential is set to zero at  $y = 7 \mu\text{m}$ . Phase space distributions consist of electrons in the region of  $y \geq 0$  and  $-0.15 \leq x \leq +0.15 \mu\text{m}$ , and are normalized by the initial charge density of the cluster ions and displayed on a log scale.

## 4.2. DYNAMICS OF BOUNDARY LAYER IN BETWEEN CLUSTER AND AMBIENT GAS

---

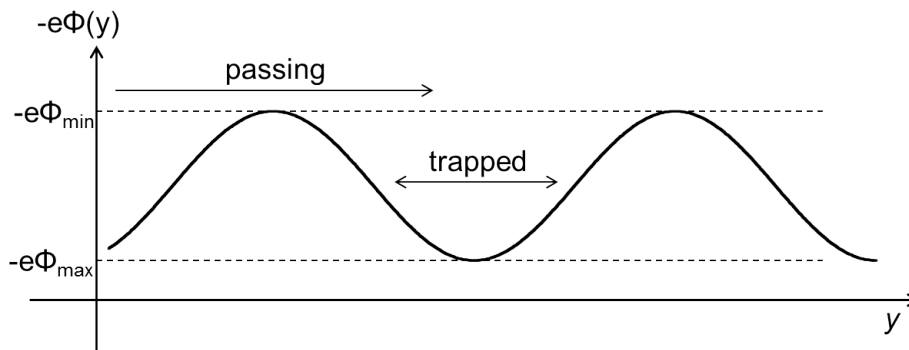


Figure 4.15: The 1D image of the electrostatic potential for electrons  $-e\Phi$ , where electrons having an energy of  $H_e$  are trapped by or passing  $-e\Phi$ .

the compressed surface broadens [Fig. 4.6(a)], the value  $E_{y2}^{max}$  reaches a constant value of around  $-0.23$  TV/m, establishing a quasi-steady state. Interestingly, at  $t \sim 300$  fs, the value  $E_{y2}^{max}$  again develops to another quasi-steady state having a constant value of around  $-0.31$  TV/m. After 400 fs, the value  $E_{y2}^{max}$  is gradually relaxed to a value of  $-0.16$  TV/m.

All these processes happen after the passage of the laser pulse, suggesting that the free energy delivered to electrons by the laser pulse causes a long time scale ion dynamics coupled with the evolution of the field  $E_y$ , which exhibits the formations of specific structures, i.e., the ambipolar field  $E_{y1}$  and the bipolar field  $E_{y2}$ . Specifically, the value  $E_{y2}^{max}$  is found to keep a constant value or even evolve to the another constant value, which creates a potential well for electrons around  $y = 3.1 \mu\text{m}$  [see Fig. 4.14(a3)]. On the other hand, a weak positive electric field, the remnant of the ambipolar electric field  $E_{y1}$  associated with the hydrodynamic expansion of the cluster, is discernible near the cluster center ( $0 \leq y \leq 1.5 \mu\text{m}$ ) [see Fig. 4.14(a3)], which creates a small potential hill for electrons around  $y = 1.5 \mu\text{m}$  [see Fig. 4.14(a3)].

The phase space distribution of electrons which travel in such electric fields and corresponding potentials is investigated. Here, the electron trajectories are calculated from the energy  $H_e = (\gamma_e - 1)m_e c^2 - e\Phi$ , where  $H_e$  is the total energy of an electron and the electrostatic potential for electrons  $-e\Phi(y)$  is defined by a function of  $y$  ( $-e\Phi_{max} < -e\Phi(y) < -e\Phi_{min}$ ). From  $H_e$ , we can decide the electron velocity for a given  $-e\Phi(y)$ . As shown in Fig. 4.15, whether an electron having the energy  $H_e$  is trapped by or passing the potential  $-e\Phi(y)$  is decided as follows:

$$\begin{cases} -e\Phi_{max} < H_e < -e\Phi_{min} & : \textit{trapped} \\ -e\Phi_{min} < H_e & : \textit{passing} \end{cases} \quad (4.6)$$

## 4.2. DYNAMICS OF BOUNDARY LAYER IN BETWEEN CLUSTER AND AMBIENT GAS

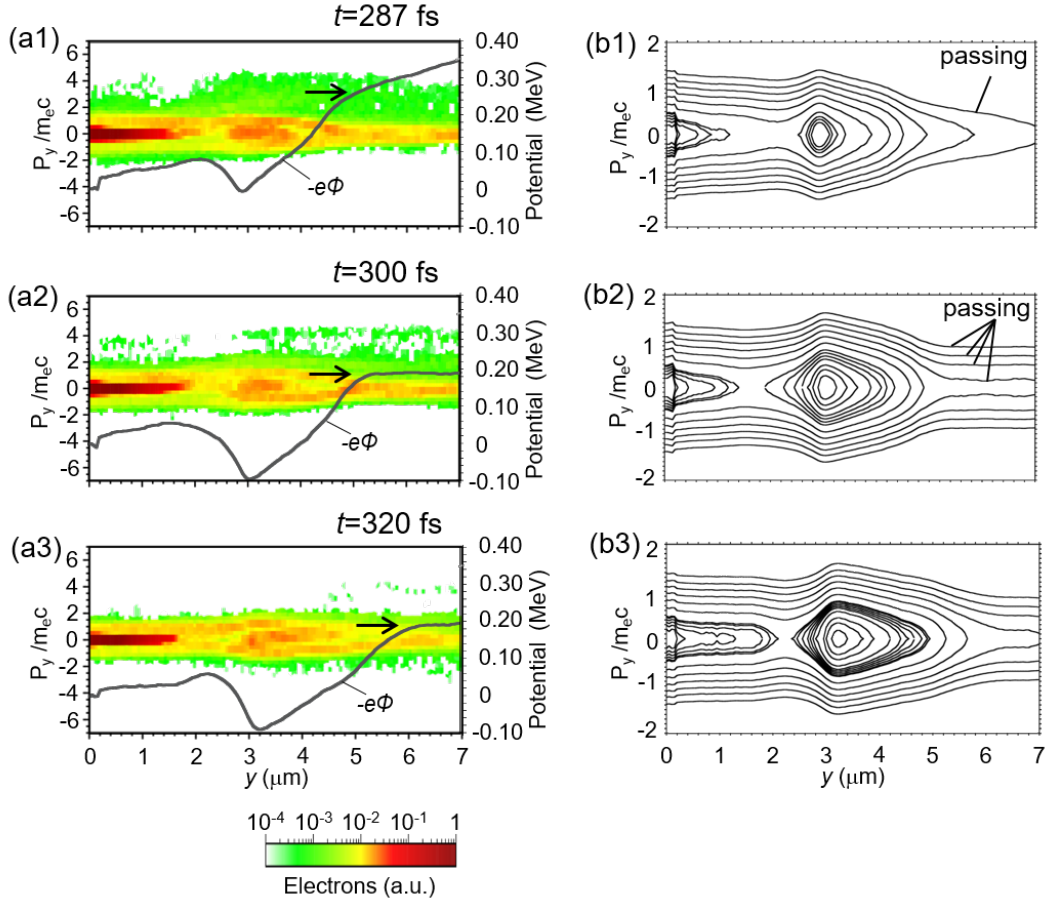


Figure 4.16: The 1D cross sectional views for (a1)-(a3) the phase space distributions of electrons and the electrostatic potential for electrons  $-e\Phi$  (gray solid line), and (b1)-(b3) the contour plots of electron trajectories along the  $+y$  direction from the center of the cluster at (a1), (b1)  $t = 287$  fs, (a2), (b2)  $t = 300$  fs, and (a3), (b3)  $t = 320$  fs. Arrows indicate the height of each potential at the position of the Coulomb explosion front. The electrostatic potential is set to zero at  $y = 0 \mu\text{m}$ . Phase space distributions consist of electrons in the region of  $y \geq 0$  and  $-0.15 \leq x \leq +0.15 \mu\text{m}$ , and are normalized by the initial charge density of the cluster ions and displayed on a log scale.

## 4.2. DYNAMICS OF BOUNDARY LAYER IN BETWEEN CLUSTER AND AMBIENT GAS

---

As shown in Fig. 4.14(b3) [also in Fig. 4.16(b2)], at  $t = 300$  fs, two potential wells, a relatively shallow one around  $y = 0 \mu\text{m}$  and a deep one around  $y = 3.1 \mu\text{m}$ , and a small potential hill around  $y = 1.5 \mu\text{m}$  are created, where a separatrix with an X-point is formed. These two potential wells are then embedded in a global potential well ranging from  $y = 0 \mu\text{m}$  to  $y = 5 \mu\text{m}$ , which is surrounded by the passing electron trajectories. As a result, the phase space structure and the bipolar structure of  $E_{y2}$  are sustained by the trapped electrons in three potential wells and the passing electrons. From these facts, we interpret them as an establishment of a quasi-stationary kinetic equilibrium.

For both the trapped and passing electrons, it is worth noting that they are distributed in an asymmetrical way in the phase space. This could be the reason why the value  $E_{y2}^{max}$  shows a temporally corrugated structure with a time interval of  $\sim 15$  fs (see Fig. 4.13). This time scale is close to that of the inverse bounce frequency  $\omega_b$  trapped in the potential well around  $y = 3.1 \mu\text{m}$ . When we assume 1D motion of electrons (in the  $x$  direction) and  $\Phi(x) = \Phi_0 \cos kx$ , the frequency  $\omega_b$  is derived as follows

$$\begin{aligned} m_e \frac{d^2x}{dt^2} &= -e \left( -\frac{\partial \Phi}{\partial x} \right) \\ &= -ek\Phi_0 \sin kx \\ &\simeq -ek^2\Phi_0 x \end{aligned}$$

$$\therefore \omega_b = k \sqrt{\frac{m_e}{e\Phi_0}} \left( k = \frac{2\pi}{\lambda} \right), \quad (4.7)$$

where  $k$  is the wave number,  $m_e$  is the electron mass,  $e$  is the elementary charge and  $\Phi$  is the electrostatic potential. Thus,  $T_b$  is estimated as

$$T_b = \frac{2\pi}{\omega_b} = \frac{2\pi}{k \sqrt{\frac{m_e}{e\Phi_0}}} \sim 12 \text{ fs} \quad (4.8)$$

## 4.2. DYNAMICS OF BOUNDARY LAYER IN BETWEEN CLUSTER AND AMBIENT GAS

---

Here, we used  $\lambda = 2.0 \mu\text{m}$ ,  $\Phi_0 = 0.16 \text{ MeV}$  at around  $y = 3.0 \mu\text{m}$  at  $t = 300 \text{ fs}$  [Fig. 4.14(a3)]. Similar corrugated structure due to bunched electrons trapped in a potential is observed in ref. [120].

Another interesting point is that the field  $E_{y2}$  develops to the higher negative value at around  $t = 300 \text{ fs}$  (see Fig. 4.13). The mechanism is explained as follows: Due to the development of the field  $E_{y2}$  after  $t \sim 200 \text{ fs}$ , electrons moving in the  $+y$  direction are accelerated in the negative region of the field  $E_{y2}$ , while decelerated in the positive region of the field  $E_{y2}$ . As time goes on, due to the decrease in the field  $E_{y1}$ , the potential height in the outside of the Coulomb explosion front ( $5 \leq y \leq 7 \mu\text{m}$ ) becomes small as shown in Figs. 4.16(a1)-4.16(a3). Consequently, a part of trapped electrons in the global potential well become passing ones as seen in Figs. 4.16(b1) and 4.16(b2), leading to the decrease of the net negative charge around the deep potential well and the resultant enhancement of the field  $E_{y2}$ . After that, the field  $E_{y2}$  becomes a quasi-steady state without changing the topology of the potential structure in the phase space as seen in Figs. 4.16(a2) and 4.16(a3). These dynamics are considered to be the process that the system evolves toward another kinetic equilibrium state which is energetically more stable. The lifetime of such a kinetic equilibrium structure in the phase space is the concern in relation to whether the state is observable in laboratory experiments. A vortex in a quasi-equilibrium state in phase space is well known to be suffered from a dissipation that intrinsically takes place around the separatrix between passing and trapped particles. A classical collision [121] and also an effective collision such as a thermal fluctuation could be candidates for the dissipation, which is one of the future interesting subjects.

## 4.3 The effect of the ambient gas density on the transition dynamics of the boundary layer

### 4.3.1 The structure of boundary layer for different ambient gas densities

In order to confirm density dependence on the kinetic equilibrium characterized by the bipolar electric field, we performed a series of simulations using different densities of the ambient gas and the same values for other parameters. Figures 4.17(a)-4.17(d) show the 1D cross sectional views for the charge density distributions of ions and electrons for the cluster and the ambient gas, and the resulting electric field  $E_y$  along the  $+y$  direction at  $t = 380$  fs. The densities of ambient gas electrons ( $= n_{gas}$ ) are (a)  $0.012n_c$ , (b)  $0.024n_c$ , (c)  $0.096n_c$  and (d)  $0.192n_c$ . Note that the case (b) is same as the case in Fig. 4.4, while the time is different. When the ambient gas density becomes higher, more electrons of the ambient gas flow into the expansion front of the cluster, which weakens the intensity of the field  $E_{y1}$ . Resultantly, the expansion velocity of the cluster, which is equivalent to the shock velocity  $v_{sh}$ , decreases as seen in Figs. 4.17(a)-4.17(d). On the other hand, the density of the compressed surface increases roughly in proportion to the ambient gas density. As a result, the intensity of the field  $E_{y2}$ , which is created around the compressed surface, also becomes large. Therefore, in high density cases, as seen in Figs. 4.17(c) and 4.17(d), a part of the cluster ions is decelerated by the large field  $E_{y2}$  and the staircase structure is clearly observed at  $y = 2.8 \mu\text{m}$  in Fig. 4.17(c) and at  $y = 2.5 \mu\text{m}$  in Fig. 4.17(d).

It is noted that though the expansion velocity of the cluster and the intensity of the field  $E_{y2}$  are different according to the ambient gas density, the field  $E_{y2}$  shows the same bipolar structure as the original case [ $n_{gas} = 0.024n_c$ , Fig. 4.17(b)] and the intensity of the field  $E_{y2}$  is also sustained for a long time, resulting in the establishment of the same type of the kinetic equilibrium.

Figure 4.18 shows the time history of 1D cross sectional views for the charge density distributions of the ambient gas and cluster ions at various times at  $n_{gas} = 0.192n_c$ . At  $t = 200$  fs, the compressed surface starts to slowly collapse with time as the rarefaction wave. That is, the density gradient around the compressed surface decreases with time. Then, it can be seen that a high density part of the rarefaction wave and a low density part are connected with a point of constant density (at  $y = 1.3 \mu\text{m}$ , Fig. 4.18). At  $t = 380$  fs, a spatially extended structure of the ambient gas ions in the region of  $0.8 \leq y \leq 2.8 \mu\text{m}$  in Fig. 4.17(d) represents the rarefaction wave, which propagates in both  $\pm y$  directions (see also Fig. 4.18). The incoming ambient gas ions are not reflected by the potential wall formed by the field  $E_{y2}$  and pass over it [ $y = 3.2 \mu\text{m}$ , in Figs. 4.17(d1) and 4.17(d2)].

The change from the acceleration phase to the phase which the acceleration terminates is clearly observed in Fig. 4.19. In the case  $n_{gas} = 0.024n_c$ , at around  $t = 200$  fs, reflection of the upstream ambient gas ions at the compressed surface terminates. In this case, the

### 4.3. THE EFFECT OF THE AMBIENT GAS DENSITY ON THE TRANSITION DYNAMICS OF THE BOUNDARY LAYER

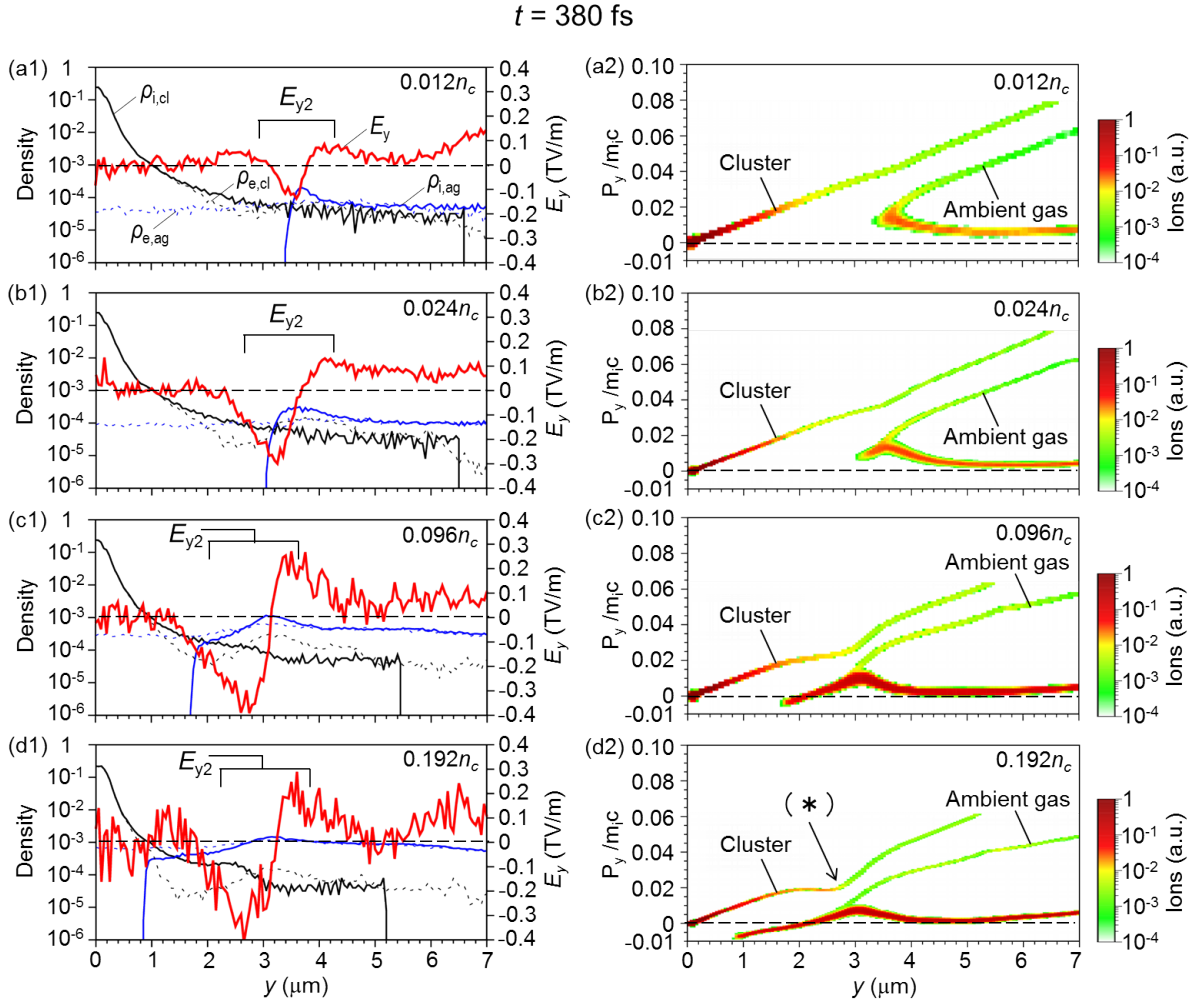


Figure 4.17: (a1)-(d1) 1D cross sectional views for the charge density distributions of cluster ions  $\rho_{i,cl}$  (black solid line), ambient gas ions  $\rho_{i,ag}$  (blue solid line), cluster electrons  $\rho_{e,cl}$  (black dotted line), ambient gas electrons  $\rho_{e,ag}$  (blue dotted line), and the resulting electric field  $E_y$  (red solid line) along the  $+y$  direction from the center of the cluster at  $t = 380$  fs with the ambient gas density of (a)  $0.012n_c$ , (b)  $0.024n_c$ , (c)  $0.096n_c$  and (d)  $0.192n_c$ . Densities are normalized by the initial density of the cluster ions. (a2)-(d2) The phase space distributions of ions (cluster and ambient gas) at  $t = 380$  fs with the ambient gas density of (a)  $0.012n_c$ , (b)  $0.024n_c$ , (c)  $0.096n_c$  and (d)  $0.192n_c$ . The phase space distributions consists of ions in the region of  $y \geq 0$  and  $-0.15 \leq x \leq +0.15 \mu\text{m}$ , and are normalized by the initial charge density of the cluster ions and displayed on a log scale.

### 4.3. THE EFFECT OF THE AMBIENT GAS DENSITY ON THE TRANSITION DYNAMICS OF THE BOUNDARY LAYER

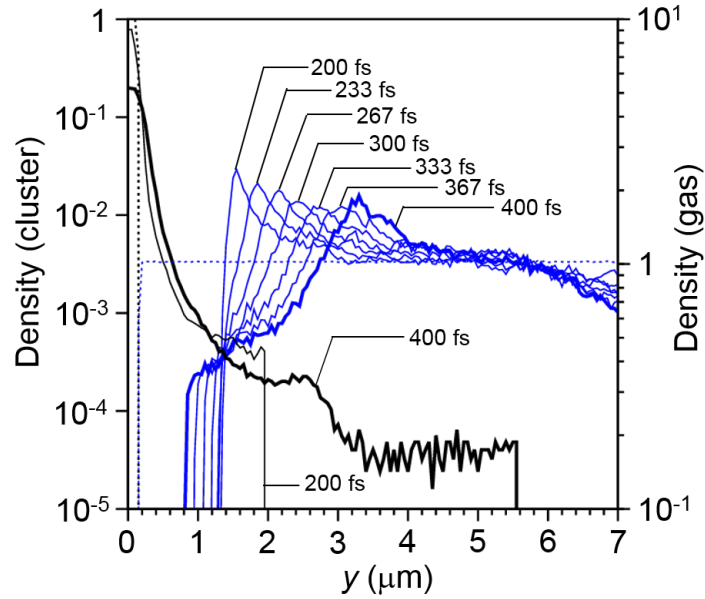


Figure 4.18: 1D cross sectional views for the density distributions of ambient gas ions (blue lines) and cluster ions (black lines) at  $n_{gas} = 0.192n_c$  along the  $+y$  direction from the center of the cluster at various times. The initial density distributions of the ambient gas (blue dotted line) and cluster (black dotted line) ions are also shown. Densities are normalized by the initial density of the ambient gas or cluster ions.

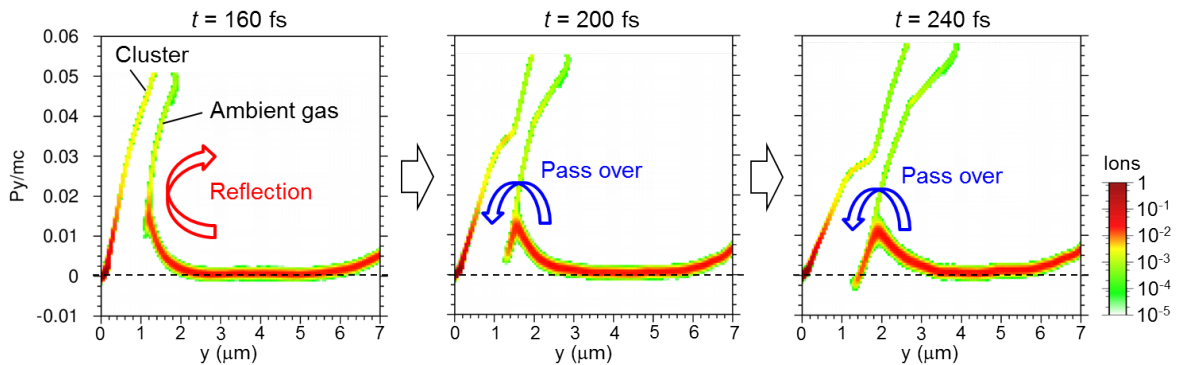


Figure 4.19: The phase space distributions of the cluster and ambient gas ions along the  $+y$  direction from the center of the cluster at  $n_{gas} = 0.192n_c$  at (a)  $t = 160$  fs, (b)  $t = 200$  fs, and (c)  $t = 240$  fs. Charge densities are normalized by the initial density of ions. Phase space distributions consist of ions in the region of  $y \geq 0$  and  $-0.15 \leq x \leq +0.15$   $\mu\text{m}$ , and are normalized by the initial charge density of the cluster ions and displayed on a log scale.

### 4.3. THE EFFECT OF THE AMBIENT GAS DENSITY ON THE TRANSITION DYNAMICS OF THE BOUNDARY LAYER

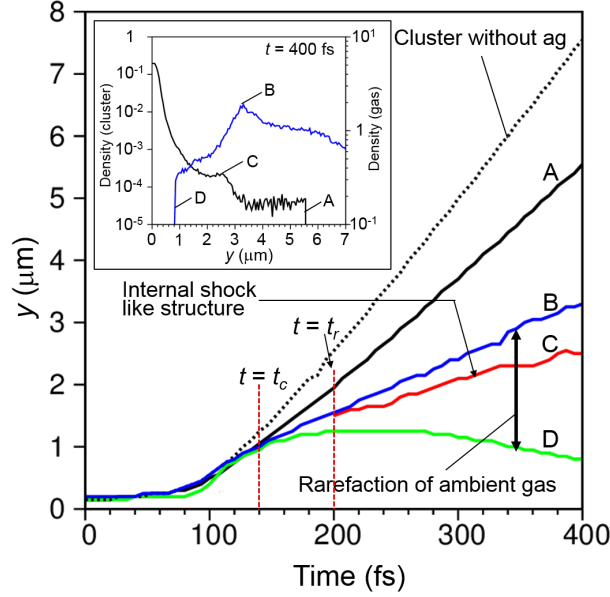


Figure 4.20: Temporal evolutions for the Coulomb explosion front of the cluster ions (black solid line, A), the rarefaction wave fronts of the ambient gas ions (blue and green solid lines, B and D), and the position of the staircase structure in the cluster (red solid line, C) along the  $+y$  direction from the center of the cluster at  $n_{gas} = 0.192n_c$ . The inset shows a 1D cross sectional view for the density distributions of ambient gas ions (blue solid line) and cluster ions (black solid line) at  $t = 400$  fs. Positions A, B, C and D in the inset correspond to those in the figure. The black dotted line represents the temporal evolution for the Coulomb expansion front of the cluster ions in a vacuum as a reference.

deceleration of cluster ions at around the compressed surface clearly starts from  $t = 200$  fs.

Figure 4.20 shows temporal evolutions for the Coulomb expansion front of the cluster ions, the rarefaction wave fronts of the ambient gas ions, and the position of the staircase structure in the cluster ions at  $n_{gas} = 0.192n_c$ . The distance between the cluster expansion front (A) and the staircase structure (C), which appears after  $t = 200$  fs, becomes large with time. This is because the staircase structure is decelerated by the negative component of the field  $E_{y2}$ . After  $t = t_c$ , the contact surface disappears and the overlapping region is formed. At  $t = t_r$ , the structure of the compressed surface tends to evolve and leads to the rarefaction wave. The higher density part of the rarefaction wave (B) propagates in the  $+y$  direction, while the lower one (D) moves initially in the  $+y$  direction and finally in the  $-y$  direction, leading to the decrease in the density gradient and to the collapse of the ambient gas structure.

In the density distribution of the cluster ions, the staircase structure, which corresponds to a dip structure of the cluster ions at  $y = 2.5 \mu\text{m}$  [marked by (\*) in Fig. 4.17(d2)], resulting from the deceleration of cluster ions by the negative component of the field  $E_{y2}$ , is clearly formed at  $y = 2.5 \mu\text{m}$  in Fig. 4.17(d1). It can be seen that

### 4.3. THE EFFECT OF THE AMBIENT GAS DENSITY ON THE TRANSITION DYNAMICS OF THE BOUNDARY LAYER

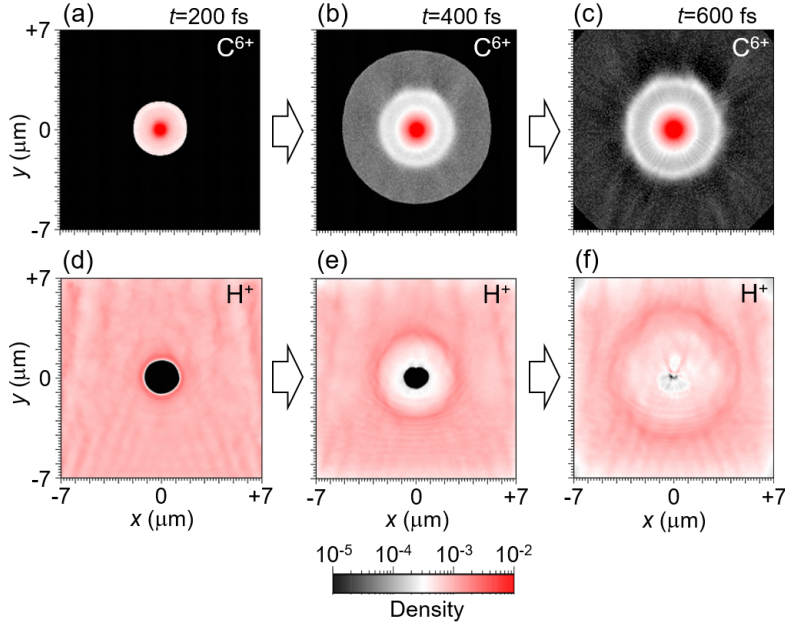


Figure 4.21: The 2D images for the charge density distributions of (a), (b), (c) the cluster ions  $\rho_{i,cl}$  and (d), (e), (f) the ambient gas ions  $\rho_{i,ag}$  at (a), (d)  $t = 200$  fs, (b), (e) 400 fs and (c), (f) 600 fs at  $n_{gas} = 0.192n_c$ . Densities are normalized by the initial charge density of the cluster ions and displayed on a log scale.

the compressed surface collapses through the rarefaction wave [see also Figs. 4.21(e) and 4.21(f)], while the cluster ions around  $y = 2.5 \mu\text{m}$  is steepened, leading to the staircase structure. This staircase structure corresponds to a ring structure in the 2D cluster density distribution as seen in Fig. 4.21(b). In later time, at  $t = 600$  fs, the staircase structure is emphasized, so that the density gap between the ring structure and both inside and outside of the ring increases, as seen in Fig. 4.21(c). That is, the formation of structure in the cluster ions and the destruction of the ambient gas structure clearly occur in pairs. Two evolutions corresponding to ambient gas ions and cluster ions are linked with each other through the evolutions of the electric field. It is worthwhile to consider the relationship between such ring structures observed in the present simulation and those observed in the universe, e.g., rings after supernova explosion in interstellar gas.

These results indicate that the kinetic equilibrium characterized by the field  $E_{y2}$  also exists in high density cases [see Figs. 4.17(c1) and 4.17(d1)], while the compressed surface evolves into the rarefaction wave with a fast time scale compared with that of low density cases. The time scale that the structures associated with ion dynamics evolve into the rarefaction wave is much slower than that of motion of electrons ( $T_b \sim 12$  fs). That is, such an equilibrium we reported in this paper seems to be a common physics process, which is formed at the boundary layer during the interaction process of two distinct collisionless plasmas.

### 4.3. THE EFFECT OF THE AMBIENT GAS DENSITY ON THE TRANSITION DYNAMICS OF THE BOUNDARY LAYER

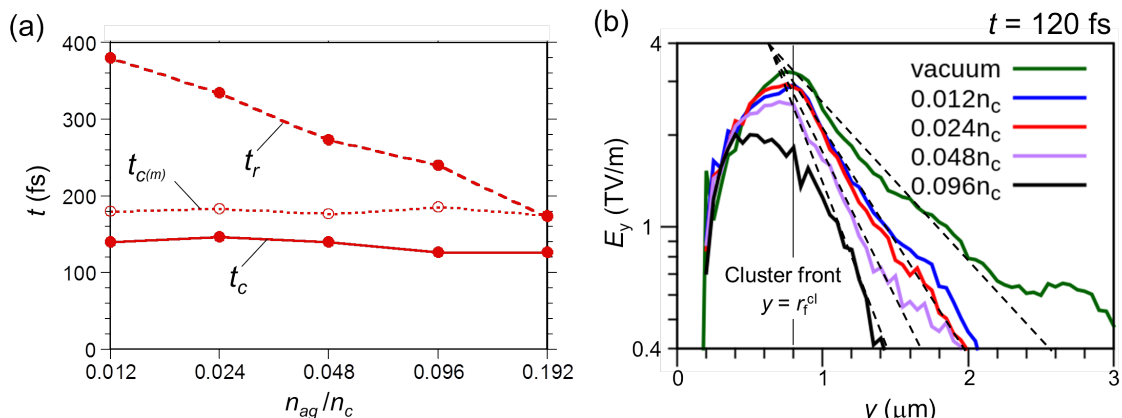


Figure 4.22: (a) The time that the crossing between the cluster expansion front and the compressed surface of ambient gas ions takes place ( $= t_c$ , the red solid line) and the time that the rarefaction wave is triggered ( $= t_r$ , the red dashed line) at the density  $n_{ag} = 0.012n_c, 0.024n_c, 0.048n_c, 0.096n_c$  and  $0.192n_c$ . The time  $t_{c(m)}$ , which is calculated by modeling the field  $E_y$ , is shown as the red dotted line. (b) The 1D cross sectional views for the ambipolar electric field  $E_y$  for the different ambient gas density  $n_{ag}$  along the  $+y$  direction from the center of the cluster at  $t = 120$  fs. The field  $E_y$  outside the cluster is approximately fit by the exponential function, which is represented by the black dashed line.

#### 4.3.2 Density dependence for transition times

The dynamics of the boundary layer evolves in three successive phases characterized by typical transition times, i.e., the crossing time  $t_c$  that the crossing between the cluster expansion front and the compressed surface of ambient gas ions takes place and the rarefaction time  $t_r$  that the rarefaction wave is triggered. In this subsection, we discuss how the initial ambient gas density  $n_{ag}$  affects these transition times.

Figure 4.22(a) shows  $t_c$  and  $t_r$  as a function of the density  $n_{ag}$ . The crossing time  $t_c$  weakly depends on the initial ambient gas density  $n_{ag}$ , which is explained as follows. The contact surface disappears when the upstream ambient gas ions pass over the shock potential associated with the ambipolar electric field and then the crossing takes place, leading to  $r_f^{ag} < r_f^{cl}$  and  $v_f^{ag} < v_f^{cl}$ . As the density  $n_{ag}$  increases in phase 1, i.e.,  $t < t_c$ , the shock velocity  $v_c$ , which satisfies  $v_c \simeq v_f^{cl} \simeq v_f^{ag}$ , becomes small due to the decrease of the ambipolar electric field  $E_{y1}$  around the contact surface. Then, the kinetic energy of upstream ambient gas ions  $K^{ag}$  in the shock rest frame also becomes small, which is the factor to increase  $t_c$ . On the other hand, as the density  $n_{ag}$  increases, not only the field  $E_{y1}$  becomes weaker but also the scale length of  $E_{y1}$ , i.e.,  $|\partial(\ln E_{y1})/\partial y|^{-1}$ , around the upstream region for the shock front  $r_c$ , i.e.,  $r_c < r$ , becomes shorter. Then, the height of the shock potential  $e\Phi_{max}$ , which is represented as

### 4.3. THE EFFECT OF THE AMBIENT GAS DENSITY ON THE TRANSITION DYNAMICS OF THE BOUNDARY LAYER

---

$$e\Phi_{max} \simeq \int_{r_\infty}^{r_c} (-eE_y)dy, \quad (4.9)$$

where  $r_\infty$  represents the location of the boundary, i.e.,  $y = 7.68 \mu\text{m}$  in the present case also becomes small, which is the factor to decrease  $t_c$ . These two opposite effects are considered to keep  $t_c$  almost constant. We also study the crossing time  $t_{c(m)}$  observed in Fig. 4.22(a) from the viewpoint of particle motions in the laboratory frame, which we discuss in the next subsection.

On the other hand, the time  $t_r$  is found to strongly depend on the density  $n_{ag}$ . That is,  $t_r$  becomes short as the density  $n_{ag}$  increases, which is explained as follows. The propagation velocity of the location exhibiting the peak density of ambient gas ions, i.e.,  $v_{f(B)}^{ag}$ , weakly depends on the density  $n_{ag}$ . Namely, the energy  $K^{ag}$  in the  $r_{f(B)}^{ag}$  rest frame also weakly depends on the density  $n_{ag}$ , which is the factor to keep  $t_r$ . On the other hand, as the density  $n_{ag}$  increases, the ambipolar electric field  $E_{y1}$  becomes weak and the scale length of the field  $E_{y1}$  around the nonlinear wave becomes short. Accordingly, the height of the electrostatic potential  $e\Phi_{max}$ , which is represented as

$$e\Phi_{max} \simeq \int_{r_\infty}^{r_{f(B)}^{ag}} (-eE_y)dy \quad (4.10)$$

also becomes small. As a result, in high density cases, upstream ambient gas ions can pass over the potential in earlier time than that in low density cases, leading to shorten  $t_r$ .

#### 4.3.3 Numerical investigation of transition time

In the laboratory frame, the crossing occurs at the moment when cluster ions ( $\text{C}^{6+}$ ) located at the cluster expansion front overtake ambient gas ions ( $\text{H}^+$ ) located in front of  $\text{C}^{6+}$ . Here, we show the procedure in deriving the crossing time  $t_c^{(m)}$  in Fig. 4.22(a) by modeling the ambipolar electric field  $E_y$  shown in Fig. 4.22(b) based on the observation of the simulation results.

As seen in Fig. 4.22(b), it can be seen that the ambipolar electric field  $E_y$  outside the cluster, i.e.,  $r_f^{cl} \leq y$ , is fit by an exponential function  $\tilde{E}(y)$  as

$$\tilde{E}(y) = E_0 \exp\left(-\frac{y - r_f^{cl}}{L_e}\right), \quad (4.11)$$

### 4.3. THE EFFECT OF THE AMBIENT GAS DENSITY ON THE TRANSITION DYNAMICS OF THE BOUNDARY LAYER

---

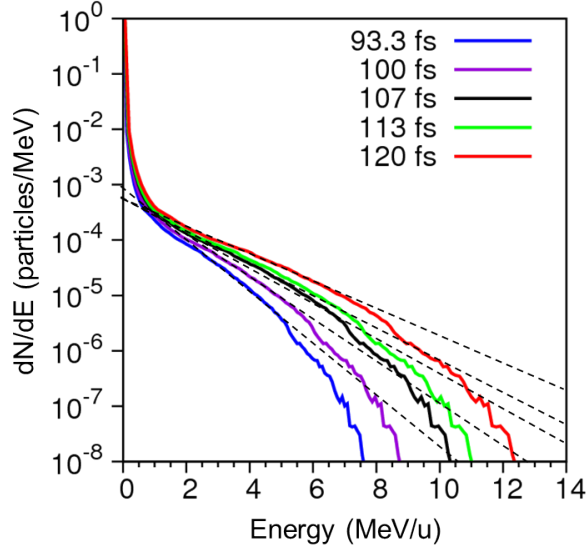


Figure 4.23: Energy distribution of the cluster electrons at  $t = 93.3$  fs, 100 fs, 107 fs, 113 fs and 120 fs. Black dashed lines show the exponential.

where  $E_0$  is the intensity of the field at the cluster surface ( $y = r_f^{cl}$ ) and  $L_e$  is the scale length of the field. Here, we assume that the intensity  $E_0$  and the scale length  $L_e$  in Eq. (4.11) depend on the ambient gas density  $n_{ag}$  while maintaining the exponential function form [see Fig. 4.22(b)].

Figure 4.23 shows the energy distributions of the cluster electrons at different times for the early stage of the cluster expansion. As seen in Fig. 4.23, electrons show a Maxwellian distribution (black dashed lines in Fig. 4.23), while the distribution is truncated exhibiting the maximum energy. It is noted that the maximum energy of electrons is considered to be determined by the heating process.

Here, we apply the model in ref. [122] to the cluster expansion dynamics in a 1D configuration. The model describes the plasma expansion into the vacuum using a BGK type distribution function for the electron under the condition that the electron velocity distribution is truncated. Under the condition that the electron velocity distribution is truncated at  $|v_y| = v_0$  and electrons have the maximum energy  $1/2m_e v_0^2$  ( $= \varepsilon_{max}$ ), the BGK solution for the electron distribution is represented by

$$f(v_y, y) = \begin{cases} N_0 \left( \frac{m_e}{2\pi T_e} \right)^{\frac{3}{2}} \exp \left( -\frac{m_e v_y^2}{2T_e} + \Phi \right) & (|v_y| \leq v_0) \\ 0 & (|v_y| \geq v_0) \end{cases} \quad (4.12)$$

### 4.3. THE EFFECT OF THE AMBIENT GAS DENSITY ON THE TRANSITION DYNAMICS OF THE BOUNDARY LAYER

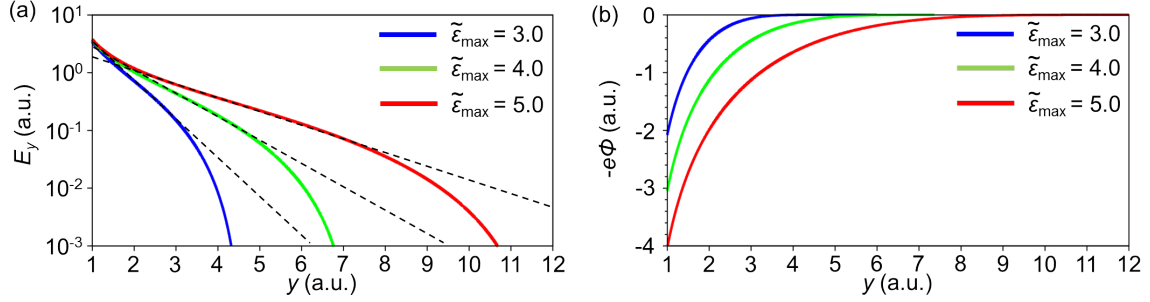


Figure 4.24: The 1D distributions of (a) the electric field and (b) the electrostatic potential for electrons calculated by the scheme introduced in ref. [122] for three cases, i.e.,  $\tilde{\epsilon}_{max} = 3, 4,$  and  $5$ . Here,  $\tilde{\epsilon}_{max}$  represents the maximum energy of electrons which is normalized by the temperature of electrons. The ion front is set to  $y = 1$  and the outer region of ions is shown. The black dashed lines represent the exponential fitting function for the each energy  $\tilde{\epsilon}_{max}$ .

where  $N_0$  and  $T_e$  are the normalization factor related to the electron density and the electron temperature, respectively. By integrating Eq. (4.12) for  $-v_0 \leq v_y \leq v_0$ , we obtain the following Poisson equation,

$$\frac{d^2\Phi}{dy^2} = \begin{cases} \delta \left[ N_0 \exp(\Phi) \operatorname{erf}(\sqrt{\Phi}) - N_i \right] & (0 \leq y \leq r_f^{cl}) \\ \delta N_0 \exp(\Phi) \operatorname{erf}(\sqrt{\Phi}) & (r_f^{cl} \leq y \leq r_{f,e}^{cl}) \end{cases} \quad (4.13)$$

where

$$\operatorname{erf}(x) = \frac{2}{\sqrt{\pi}} \int_0^x \exp(-t^2) dt$$

is the error function. Here,  $\delta$  is the normalization factor related to the Debye length. Here,  $r_{f,e}^{cl}$  represents the location of the electron front, which is equal to the front edge of the potential for electrons  $-e\Phi$ , i.e.,  $-e\Phi(r_{f,e}^{cl}) = 0$ . Here, we solve the Eq. (4.13) as a boundary value problem including eigenvalues of  $N_0$ ,  $\Phi(r_f^{cl})$  and  $d\Phi(r_f^{cl})/dy$  under the initial value of  $\Phi(0) = \tilde{\epsilon}_{max}$ . Then, we obtain the following relation concerning the potential  $\Phi$  outside the cluster ion front by integrating Eq. (4.13) under the initial values of  $N_0$ ,  $\Phi(r_f^{cl})$  and  $d\Phi(r_f^{cl})/dy$  in the vacuum region, i.e.,  $r_f^{cl} \leq y \leq r_{f,e}^{cl}$ :

### 4.3. THE EFFECT OF THE AMBIENT GAS DENSITY ON THE TRANSITION DYNAMICS OF THE BOUNDARY LAYER

---

$$\frac{1}{2} \left( \frac{d\Phi}{dy} \right)^2 = \delta N_0 \left[ \exp(\Phi) \operatorname{erf}(\sqrt{\Phi}) - 2\sqrt{\frac{\Phi}{\pi}} \right]. \quad (4.14)$$

Figure 4.24 shows the field  $E_y = -(\partial\Phi/\partial y)$  and the potential for electrons  $-e\Phi$ , which are calculated from Eq. (4.14) for different  $\tilde{\varepsilon}_{max}$ . Here,  $\tilde{\varepsilon}_{max}$  represents the maximum energy of electrons which is normalized by the electron temperature  $T_e$ . It is noted that the outer region of the ions ( $y \geq 1$ ) is shown. As seen in Fig. 4.24(a), the field  $E_y$  is found to fit by the exponential function (black dashed lines) in a limited region. The region becomes wider for larger  $\tilde{\varepsilon}_{max}$  [see Fig. 4.24(a)], indicating that the field  $E_y$  is approximately fit by the exponential function of Eq. (4.11) in the limited region under the condition that the maximum energy of electrons is enough high compared with the temperature  $T_e$ . It is noted that the spatial distribution of the potential for electrons  $-e\Phi$  [Fig. 4.24(b)] is consistent with the electron trajectory in Fig. 4.14(b1), where high energy electrons around the cluster expansion front ( $y \sim 1 \mu\text{m}$ ) lose their energy during their motion in the  $+y$  direction and are reflected around the boundary ( $y = 7 \mu\text{m}$ ).

Figure 4.25 shows the spatial distribution of the field  $E_y$  at different times for two densities  $n_{ag} =$  (a)  $0.024n_c$  and (b)  $0.048n_c$ . In both cases, the spatial distribution of the field  $E_y$  for  $r_f^{cl} \leq y$  is found to weakly depend on time. This indicates that we can approximate the field  $E_y$  as the static electric field. We have also confirmed this tendency for densities  $n_{ag} = 0.012n_c, 0.096n_c$  and  $0.192n_c$ .

Figures 4.26(a1) and 4.26(a2) show the function  $\tilde{E}(y)$  (red dashed line) and the field  $E_y$  (red solid line), which is obtained from the simulation result at  $t = 93.3$  fs for the density  $n_{ag} =$  (a1)  $0.024n_c$  and (a2)  $0.048n_c$ . As shown in Figs. 4.26(a1) and 4.26(a2), the function  $\tilde{E}(y)$  is in good agreement with the field  $E_y$ .

Here, we study trajectories of ions ( $\text{C}^{6+}$  and  $\text{H}^+$ ) by using the function  $\tilde{E}(y)$ . Figures 4.26(b1) and (b2) show the location of the cluster ion (black solid line), which corresponds to the cluster expansion front  $r_f^{cl}$ , and the location of the ambient gas ions (blue lines) in the  $+y$  direction as a function of  $t$ . The cluster ion is initially located at  $y = R_0$  and the ambient gas ions are initially located at  $y = R_0, 2R_0, 4R_0, 6R_0, 8R_0, 10R_0$ , or  $12R_0$ . These ions start to move by the function  $\tilde{E}(y)$  as shown in Figs. 4.26(b1) and (b2).

The velocity of the cluster ion, i.e., the gradient of black solid lines in Figs. 4.26(b1) and (b2), initially increases and finally reaches almost the constant value, which is consistent with the simulation results [see black solid line in Fig. 4.6(a)]. The velocity of the ambient gas ions, i.e., the gradient of blue lines in Figs. 4.26(b1) and (b2), shows the same tendency as the velocity of the cluster ion. However, the velocity of the ambient gas ions decreases with distance from the initial cluster location, i.e.,  $y = R_0$ . Resultantly, as time goes on, the cluster ion catches up with and overtakes the ambient gas ions which are initially located at  $y \geq 8R_0$  at  $t \sim \tilde{t}_c$  as seen in Figs. 4.26(b1) and (b2). We calculated the trajectories of ions ( $\text{C}^{6+}$  and  $\text{H}^+$ ) for the each density  $n_{ag}$  and confirmed that the

### 4.3. THE EFFECT OF THE AMBIENT GAS DENSITY ON THE TRANSITION DYNAMICS OF THE BOUNDARY LAYER

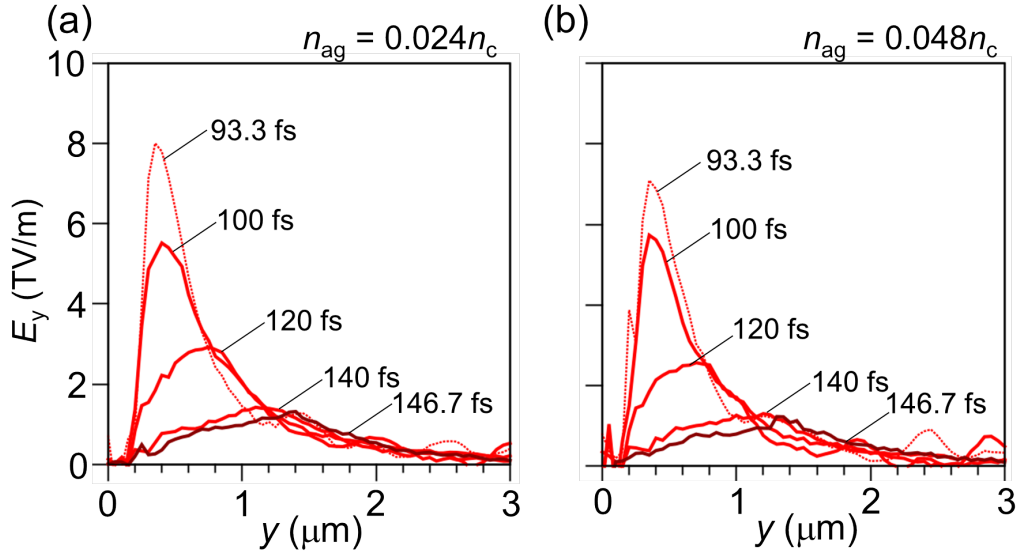


Figure 4.25: The spatial distribution of the field  $E_y$  at different times for the density (a)  $n_{ag} = 0.024n_c$  and (b)  $n_{ag} = 0.048n_c$ .

crossing time  $\tilde{t}_c$  is almost the same value.

Here, the crossing time  $\tilde{t}_c$  observed in Figs. 4.26(b1) and (b2) can be converted into the real value by using the relation between the velocity of cluster expansion front obtained from simulation results and the location  $y$  in Figs. 4.26(b1) and (b2), which is normalized by the cluster initial radius  $R_0$ . Then, the crossing time  $t_c^{(m)}$  observed in Fig. 4.22(a) is estimated by  $t_c^{(m)} = \tilde{t}_c + t_{laser}$ , where  $t_{laser} = 66.7$  fs is the time that the laser pulse having the half value of the laser peak intensity reaches the cluster center. The time  $t_c^{(m)}$  shows the same tendency as the time  $t_c$  as seen in Fig. 4.22(a), indicating the adequacy of the model introduced in this subsection.

#### 4.3.4 Maximum kinetic energy of the ambient gas ions

Finally, we summarize the difference of the maximum energy of the ambient gas ions. The ambient gas ions are accelerated by two mechanisms: In phase 1 ( $t < t_c$ ), ambient gas ions are accelerated by the ambipolar electric field structure  $E_{y1}$  while the contact surface is sustained. In phase 2 ( $t_c < t_r$ ), after the contact surface disappears and the overlapping region is formed, ambient gas ions are continuously accelerated by the bipolar electric field structure  $E_{y2}$  before the onset of the rarefaction wave. Figure 4.27 shows the maximum energy of ambient gas ions at the time which the contact surface disappears ( $K_{max1}$  at  $t = t_c$ ) and at the time which the compressed surface starts to evolve into the rarefaction wave ( $K_{max2}$  at  $t = t_r$ ) at different ambient gas densities. It can be seen that both maximum energies  $K_{max1}$  and  $K_{max2}$  tend to become small when the ambient gas density increases. This is because the shock velocity  $v_{sh}$  becomes small in high density

### 4.3. THE EFFECT OF THE AMBIENT GAS DENSITY ON THE TRANSITION DYNAMICS OF THE BOUNDARY LAYER

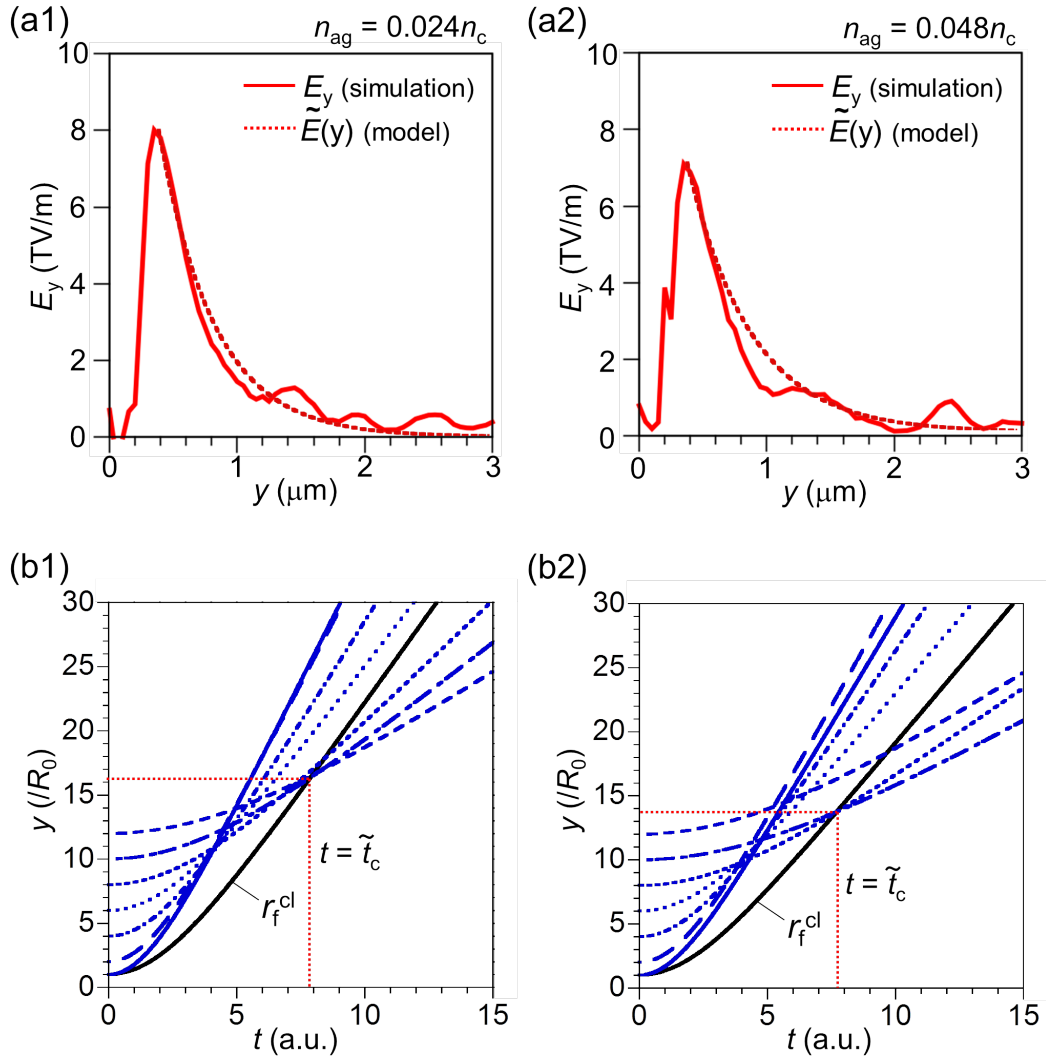


Figure 4.26: (a) The spatial distribution of the field  $E_y$  (red solid line) at  $t = 93.3$  fs for the density  $n_{ag} =$  (a1)  $0.024n_c$  and (a2)  $0.048n_c$ . The exponential function  $\tilde{E}(y)$  (red dashed line) is also shown. (b) Temporal evolutions for the location of the cluster ion (black solid line), which is initially located at  $y = R_0$ , and that of the ambient gas ions (blue lines), which are initially located at  $y = R_0, 2R_0, 4R_0, 6R_0, 8R_0, 10R_0$ , or  $12R_0$ . Note that (b1) and (b2) correspond to (a1)  $0.024n_c$  and (a2)  $0.048n_c$ , respectively. The location  $y$  is calculated by the function  $\tilde{E}(y)$  and is normalized by the initial cluster radius  $R_0$ . Red dashed line represent the time  $\tilde{t}_c$  that the crossing takes place.

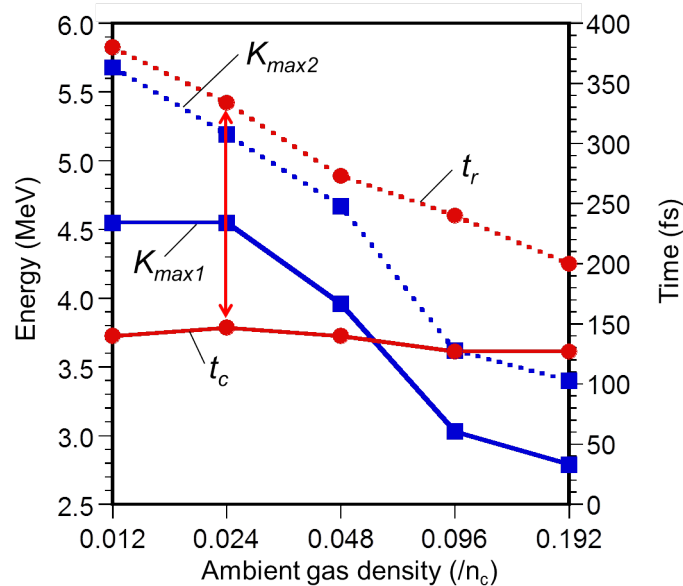


Figure 4.27: The maximum energy of ambient gas ions (blue squares) at the time which the contact surface disappears ( $= K_{max1}$ ) and at the time which the compressed surface starts to evolve into the rarefaction wave ( $= K_{max2}$ ) at different ambient gas densities. The times which the contact surface disappears ( $= t_c$ ) and the compressed surface starts to evolve into the rarefaction wave ( $= t_r$ ) are also shown as red circles.

cases, which leads to the decrease in the velocity of reflected ambient gas ions. In high density cases, the duration of the ambient gas acceleration by the field  $E_{y2}$ , i.e.,  $t_r - t_c$  becomes short, resulting from the early onset of the rarefaction wave. Namely, it is found that the maximum energy of the ambient gas ions and the duration of the ambient gas acceleration are strongly depend on the ambient gas density.

## 4.4 Summary

In summary, we have investigated the microscopic dynamics of the boundary layer, created in between two distinct collisionless plasmas by the Coulomb expansion of the femtosecond laser-irradiated cluster medium, and the associated acceleration of the ambient gas ions with the 2D PIC simulations. We revealed that the dynamics of the collisionless plasma boundary layer is categorized into three phases: (1) cluster expansion with keeping the contact surface between the Coulomb expansion front of cluster ions and the compressed surface of ambient gas ions, (2) the formation of the overlapping region between the Coulomb expansion front and the compressed surface and (3) the onset of the rarefaction wave triggered by the termination of the acceleration of ambient gas ions. The overlapping between the Coulomb expanding cluster ions and the ambient gas ions at the boundary layer occurs when the kinetic energy of ambient gas ions exceeds the potential of the shock created by the Coulomb expansion of the cluster. The interpenetration of the

#### 4.4. SUMMARY

---

Coulomb expanding ions into the ambient gas ions creates two different electric fields, the ambipolar electric field  $E_{y1}$  associated with the Coulomb expansion front and the bipolar electric field  $E_{y2}$  around the compressed surface, in the boundary layer on different time scales and locations.

The ambient gas ions are accelerated by two mechanisms: In phase 1 (before  $t = 150$  fs), the ambient gas ions are accelerated by the field  $E_{y1}$ , associated with the collisionless shock launched at the contact surface. In phase 2 (after  $t = 150$  fs), the contact surface disappears and the overlapping region is formed. In this phase, the ambient gas ions are accelerated by the field  $E_{y2}$ , associated with the nonlinear wave created at the compressed surface of the ambient gas ions. In phase 3 (after  $t = 340$  fs), acceleration of ambient gas ions at the compressed surface terminates, which leads to the onset of the rarefaction wave. The narrow energy spectral feature of the accelerated ambient gas ions, which is typical for the collisionless shock ion acceleration, becomes less pronounced due to the acceleration by the front part of the ambipolar electric field  $E_{y1}$  and the temporal velocity change of the moving structures.

We found that the ambipolar field  $E_{y1}$  decays quickly, while the bipolar field  $E_{y2}$  persists for a long time even after the passage of the laser pulse. This is because the nonlinear wave structure associated with the field  $E_{y2}$  is sustained as a quasi-stationary kinetic equilibrium established via the dynamics of the trapped and the passing electrons on the electrostatic potential created by the superposition of the field  $E_{y1}$  and the field  $E_{y2}$ . The equilibrium we reported in this paper is considered to be related to Bernstein-Greene-Kruskal (BGK) type kinetic equilibrium [117, 118]. The analytical model describing such a quasi-stationary kinetic equilibrium coupled with slowly evolving ion dynamics is a future problem. In addition, we studied the establishment of the equilibrium in a wide range of densities of the ambient gas. We found that the kinetic equilibrium also exists in low and/or high density cases, while in high density cases the transition from the contact surface through the overlapping region to the rarefaction wave occurs with a fast time scale compared with that of low density cases. In the case of the higher ambient gas density, the ring-like and/or staircase structure in the cluster ions is clearly observed during the destruction process of the compressed surface of ambient gas ions. The formation of such ring structures can be seen in many place in the universe.

The formation of such an equilibrium has been reported in space plasmas such as the plasma sheet boundary layer in the Earth's magnetotail [123] and the downward-current regions of the auroral zone [124]. The future observation of such nonlinear waves under laboratory conditions may help understand behaviors of nonlinear electrostatic waves and related particle accelerations in space and astrophysical plasmas.

Here, we consider the 2D case while it is valuable to discuss the effect of the dimension of the system on the dynamics and structure, specifically on the formation of the kinetic equilibrium. Since the phenomena after the laser irradiation is spherically symmetric, so that 1D simulation assuming electron distribution functions is possible, which would have an advantage in parametrizing the phenomena and/or deriving a scaling law. This is a future work. On the other hand, in terms of the 3D effect, the establishment of the kinetic equilibrium observed in the 2D simulation is also expected to take place because it

#### 4.4. SUMMARY

---

is driven by the 1D motion of electrons in the radial direction of the cluster. In future, we will perform the 3D simulation and confirm the adequacy of the 2D simulation. Moreover, it is worthwhile to study the critical condition for the formation of kinetic equilibrium where not only the ambient gas density but also other parameters are considered to play a role. For this purpose, it is necessary to investigate the parametric dependence of the phenomena, which is a next step work.

# Chapter 5

## Proton acceleration driven by hemispherically converging collisionless shock

### 5.1 Overview

We present a series of three-dimensional (3D) particle-in-cell (PIC) simulations that demonstrate a new approach for producing a quasimonoenergetic proton bunch based on the use of hemispherically converging collisionless shock created in laser-cluster interactions at the relativistically induced transparency regime.

By the action of focusing an ultrashort, petawatt (PW) class laser pulse onto a micron-size spherical cluster target composed of solid-density  $\sim 10^{10}$  hydrogen molecules, a crescent-shaped collisionless shock, launched at the laser-irradiated hemisphere, propagates inward and converges at the sphere center by piling up the upstream protons, where significant enhancement of the proton density and the shock electric field are induced, triggering collisionless shock acceleration (CSA) of the upstream protons. The new finding here is that when the shock reaches at the sphere center, combined with the onset of relativistic induced transparency (RIT) in dense plasma at the same moment, the bunch of quasimonoenergetic protons is shot out from the shock surface like a *bullet*, leading to the enhancement of the monochromaticity of the quasimonoenergetic proton bunch. The proton bunch is further accelerated by the remnant electric fields in the inside of the cluster, and again further accelerated by the sheath electric field in the outside of the cluster. Finally, the kinetic energy of the proton bunch reaches  $\sim 300$  MeV energy with  $\sim 10\%$  energy spread and  $\sim 5^\circ$  half-divergence angle via the effect of the RIT. The present mechanism works for finite ranges of parameters with threshold values concerning the laser peak intensity ( $I > 2 \times 10^{21}$  W/cm<sup>2</sup>) and the cluster radius ( $R_0 > 0.6 \mu\text{m}$ ), resulting from the synchronization of the multiple processes, i.e., shock acceleration and propagation, collisionless shock acceleration, onset of relativistically induced transparency, and sheath acceleration, in a self-consistent manner. The present scheme utilizing the internal and external degrees of freedom ascribed to the spherical cluster leads to the proton bunch

## 5.1. OVERVIEW

---

alternative to the plain target, which allows the operation with high repetition rate and impurity free. Combined with the future high-repetitive PW class lasers, the highly directional and impurity-free nature of such a quasimonoenergetic proton bunch opens a path to practical applications of the laser accelerated protons, e.g., hadron therapy.

## 5.2 Mechanisms for obtaining quasimonoenergetic protons

### 5.2.1 Ion acceleration mechanisms (TNSA, RPA, BOA and CSA)

Laser plasma ion acceleration is characterized by a very large accelerating electric field gradient and a short pulse length, and is extensively studied over the past decade [36, 99]. This is because resultant MeV/u-class ion beams have unique properties, such as ultrashort duration, high brilliance, and low emittance, that explore a broad range of applications, including proton radiography [100], hadron therapy [101, 103], nuclear science [104, 105], fast ignition [106, 107], isochoric heating of matter [108], and radiation-induced processes in matter [109].

The recent advancements in both laser and target fabrication techniques have led to the enhancement of the accelerated proton cutoff energies close to 100 MeV [27–29]. However, the exponential energy spectra have almost 100% energy spread, which reduces the effective beam current to be utilized. In addition, lower angular divergence of accelerated ions and also higher repetition rates, which are technological issues using solid thin film targets, are requested for the wider use of this scheme. Several schemes have so far been proposed to explain experimental results and to explore further efficient acceleration.

Most applications, such as a proton therapy [101], require a high energy ion beam with a narrow (monoenergetic) energy spread. Achieving narrower energy bandwidth and lower divergence are challenging tasks and thus have been less systematically investigated because they require an alternative to the most standard acceleration method, the so-called Target Normal Sheath Acceleration (TNSA) mechanism [32], where the accelerated ions intrinsically exhibit broad exponential energy spectra with wide angular divergence. To obtain a narrow energy spectrum, considerable progress has been achieved via the engineering of target structures [34, 35], the development of the isolated sphere target [125, 126] and the exploration of advanced acceleration mechanisms [42, 46, 48, 50, 54, 56, 61, 62, 127]. In most of these cases, the results are either preliminary or require further confirmation.

In opaque density plasma regime, TNSA [30–35] and radiation pressure acceleration (RPA) [37–49, 51–53] are major ion acceleration mechanisms in laser-driven ion acceleration method. TNSA mechanism typically produces a broad energy spread. In TNSA, by using solid target ( $\sim\mu\text{m}$ ), quasimonoenergetic ( $\delta E/E \sim 17\text{--}40\%$ ) ions were experimentally observed, but the ion energies were limited to a few MeV/u with low energy conversion efficiency ( $\sim 1\%$ ) [34, 35]. On the other hand, RPA mechanism is known to have a potential to produce quasimonoenergetic ions. In RPA, by using ultra-thin solid target ( $\sim\text{nm}$ ), 2.5 MeV/u quasimonoenergetic ( $\delta E/E \sim 35\%$ ) ions with high energy conversion efficiency (2.5%) [42] and 7 MeV/u quasimonoenergetic ( $\delta E/E \sim 60\%$ ) ions [48] were experimentally observed. However, the monochromaticity is rather weak because of the limited effect of RPA. Many theoretical and numerical studies (mainly

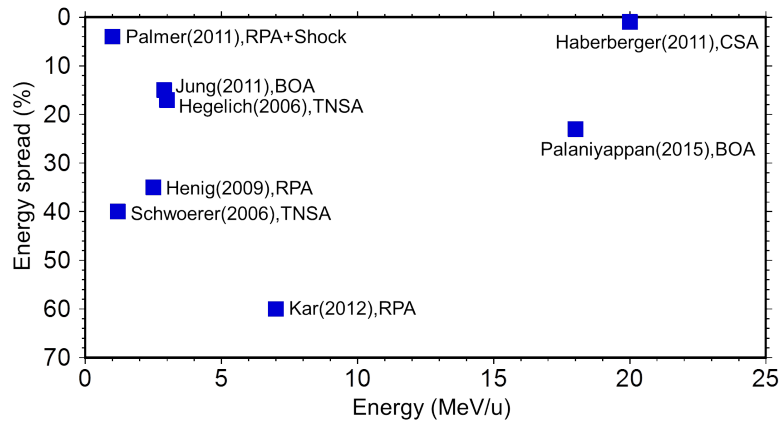


Figure 5.1: Recent experimental results concerning the generation of quasimonoenergetic ions.

one-dimensional or two-dimensional simulations) concerning RPA mechanism reported the generation of 100s MeV/u – GeV/u quasimonoenergetic ions. However, they require extremely high laser intensities ( $I > 10^{22}$  W/cm<sup>2</sup>) [37, 43, 44] or relatively complicated target fabrication [49, 52]. In addition, the onset of a relativistically induced transparency (RIT) [54, 128–130] restricts the application of the promising RPA mechanism.

On the other hand, in the RIT regime, breakout afterburner (BOA) is investigated theoretically [131–133] and experimentally [54, 127, 134]. In BOA, by using thin foil target and long laser pulse ( $\sim$ picosecond),  $2.9 \pm 0.4$  MeV/u monoenergetic ( $\delta E/E \sim 15\%$ ) ions was experimentally observed [127]. In particular, due to a self-organized magnetic field, 18 MeV/u monoenergetic ( $\delta E/E \sim 23\%$ ) ions with high conversion efficiency (5%) was experimentally observed [54].

Recently, collisionless shock acceleration (CSA) [55–60] has been considered a promising mechanism for generating quasimonoenergetic ions. In the CSA regime with near critical density hydrogen gas targets, quasimonoenergetic pure protons up to  $\sim 20$  MeV ( $\delta E/E \sim 1-4\%$ ) [46, 56] and  $\sim 1$  MeV ( $\delta E/E \sim 16-30\%$ ) [61] have been obtained with  $10.6\text{-}\mu\text{m}$  and  $1.054\text{-}\mu\text{m}$  wavelength laser irradiations, respectively. In the CSA experiment with exploded nanofoils irradiated by  $0.80\text{-}\mu\text{m}$  wavelength circularly polarized lasers, quasimonoenergetic protons up to 9 MeV ( $\delta E/E \sim 30\%$ ) have been demonstrated [62]. In CSA, a collisionless shock produced in the laser-irradiated medium propagates in the same direction as the laser propagation, with a velocity of  $v_{sh}$ . At the same time, the shock forms a large and steep electrostatic potential. Subsequently, upstream ions are reflected by the electrostatic potential in the same direction as the shock propagation and get the velocity of  $2v_{sh}$ . This mechanism remains a challenge concerning low emittance of ions, but offers promising prospects of a narrow energy spread. Here, we show the recent experimental results concerning the production of quasi-monoenergetic ions in Fig. 5.1.

### 5.2.2 Ion acceleration using cluster target

From a view point of obtaining high-purity protons at a high-repetition rate, in the proton acceleration using thin film targets, we utilize hydrogen atoms attached on the surface of the film as a contamination layer, which is hardly controlled. More seriously, the mixture with debris of high- $Z$  ions due to the element of the film is not avoidable. The debris reduces the quality of proton beams and also causes a serious damage to valuable optical components. These problems lead to conclude that it is almost hopeless to achieve high-repetition-rate, impurity-free proton beams on the extension of the conventional approaches with thin film targets from the view point of long term stability and cost effectiveness.

In order to widen the possibility for high energy proton acceleration which simultaneously satisfies the requirements mentioned in the above, here, we consider a different approach using micron-size and spherical hydrogen clusters, alternative to the approach using solid thin film targets. Namely, hydrogen cluster targets can substitute for solid targets. We utilize a hydrogen cluster target, composed of  $\sim 10^{11}$  hydrogen clusters and ambient hydrogen gas only, which has successfully generated impurity-free, multi-MeV protons at 0.1 Hz in the preliminary experiment [70]. Although the repetition rate is now limited by that of the laser system, the repetition rate of producing hydrogen clusters, developed by ourselves [70], can increase up to 600 Hz [135].

In this chapter, we propose a new way to produce highly-directional, highly-reproducible, impurity free, quasi-monoenergetic proton beams reaching 300 MeV using a micron-size hydrogen cluster target. Interaction processes of an ultrashort ( $\sim 33$  fs, FWHM), high power laser pulse ( $I = 1.0 \times 10^{22}$  W/cm<sup>2</sup> [136–138]) and a micron-size hydrogen cluster [69] are investigated using three-dimensional (3D) particle-in-cell (PIC) simulations. We found a special parameter regime that highly-directional (half-divergence angle  $\sim 5$  degree) and quasimonoenergetic ( $\delta E/E \sim 10\%$ ) proton beams with energies up to  $\sim 300$  MeV are generated by collisionless shocks propagating inside the cluster with a radius  $R = 0.8 \mu\text{m}$  in the relativistically induced transparency regime.

Moreover, we found that the RIT of hydrogen cluster effectively works for  $I > 2.0 \times 10^{21}$  W/cm<sup>2</sup> and the optimum laser peak intensity which gives the maximum monochromaticity exists at  $I \sim 1.0\text{--}1.5 \times 10^{22}$  W/cm<sup>2</sup>. Moreover, we also found that the threshold value concerning the cluster radius for the quasimonoenergetic proton bunch formation exists around  $0.6 < R_0 < 0.8 \mu\text{m}$ .

## 5.3 Proton acceleration by intra-cluster collisionless shock ( $R=0.8 \mu\text{m}$ )

### 5.3.1 Numerical modeling

Simulations are performed using a 3D version of the particle-based integrated code EPIC3D [112]. The system size is  $L_x \times L_y \times L_z = 10.24 \mu\text{m} \times 20.48 \mu\text{m} \times 10.24 \mu\text{m}$  containing  $128 \times 256 \times 128$  cells. A cell size of 80 nm is employed to resolve the shock ( $\sim 0.40 \mu\text{m}$ ) and the associated electric field structures. The spherical hydrogen cluster target is placed at the center of the box  $(x, y, z) = (0, 0, 0)$ , which consists of solid-density  $\sim 10^{10} - 10^{11}$  hydrogen molecules with a radius of  $R_0 = 0.6, 0.8$  or  $1.0 \mu\text{m}$  and an electron density of  $4.6 \times 10^{22} \text{ cm}^{-3} = 26.8n_c$ , where  $n_c$  is the critical density of the plasma corresponding to the laser wavelength  $\lambda = 0.81 \mu\text{m}$ . Ambient hydrogen gas with an electron density of  $4.0 \times 10^{19} \text{ cm}^{-3} = 0.024n_c$  occupies the simulation box. The number of PIC particles used for the cluster ions and the ambient gas ions are 28,180,000 and 24,690,000 (for  $R_0=0.8 \mu\text{m}$ ), respectively, and a fully ionized plasma is employed as the initial condition. Here, the cluster is reproduced by PIC particles using 6,730 per cell. A linearly polarized laser pulse in the  $x$  direction with a wavelength of  $\lambda = 0.81 \mu\text{m}$  and a pulse duration of  $\tau = 33$  fs (FWHM) is generated from an antenna located at  $y = -4.96 \mu\text{m}$ ,  $x = z = 0 \mu\text{m}$  and propagates in the  $+y$  direction. The peak intensity of the laser pulse is set to  $I = 1.0 \times 10^{22} \text{ W/cm}^2$ , which corresponds to the normalized amplitude of a laser  $a_0 = 69$ , where  $a_0 = eE/m_e\omega_L c$ . In our simulation, the conversion efficiency of the irradiated laser energy to kinetic energy of quasimonoenergetic protons is approximately 0.042%. Note that 8.3% of irradiated laser energy is converted into kinetic energy of protons. Here, we defined irradiated laser energy as laser energy irradiated into the cross-section of the  $0.8\text{-}\mu\text{m}$  radius cluster because we used the plane wave, which has an infinite energy.

In terms of the conversion efficiency, the total energy in the laser pulse is an important indication. When we assume a Gaussian type laser electric field  $E$ , which is represented as

$$E = E_0 \exp\left(-\frac{x^2 + y^2 + z^2}{L^2}\right) \sin \phi, \quad (5.1)$$

where  $E_0$  denotes the amplitude of the laser electric field and  $L$  is the scale length. Then, the time average of  $E^2$  becomes

$$\langle E^2 \rangle = \frac{1}{2} E_0^2 \exp\left(-\frac{2x^2 + 2y^2 + 2z^2}{L^2}\right). \quad (5.2)$$

### 5.3. PROTON ACCELERATION BY INTRA-CLUSTER COLLISIONLESS SHOCK ( $R=0.8 \mu\text{M}$ )

---

Therefore, the laser energy  $\tilde{E}_{in}$  is calculated by

$$\tilde{E}_{in} = \frac{1}{2}\varepsilon_0 \int_{-\infty}^{\infty} \int_{-\infty}^{\infty} \int_{-\infty}^{\infty} \langle E^2 \rangle dx dy dz = \frac{1}{4}\varepsilon_0 E_0^2 \left( \sqrt{\frac{\pi}{2}} L \right)^3 \quad (\text{J}). \quad (5.3)$$

When we assume the laser pulse propagates in the  $+y$  direction, the scale length of  $L$  in the  $+y$  direction is represented as  $L_y = c\tau$ , where  $\tau$  is the pulse width ( $1/e$ ). Then, the temporal integration of  $L_y$  becomes

$$L_y = \int_{-\infty}^{\infty} \exp\left(-\frac{2t^2}{\tau^2}\right) dt = c\tau \sqrt{\frac{\pi}{2}}. \quad (5.4)$$

Therefore, by using Eq. (5.4), Eq. (5.3) becomes as follows:

$$E_{in} = \frac{1}{4}\varepsilon_0 E_0^2 \left( \sqrt{\frac{\pi}{2}} \right)^3 L^2 L_y = \frac{\pi^2}{8} L^2 \tau I \quad (\text{J}). \quad (5.5)$$

For example, under the condition of  $I = 1.0 \times 10^{22}$  ( $\text{W}/\text{cm}^2$ ),  $\tau = 40 \times 10^{-15}$  (s) and  $L = \sqrt{2} \times 10^{-4}$  (cm),  $E_{in}$  is approximately 9.87 (J), which is consistent with the experimentally estimated value [138]. In the present case, we assume the plane wave in the  $x$  and  $z$  directions. Then,  $\tilde{E}_{in}$  in Eq. (5.3) is represented as

$$\tilde{E}_{in} = \frac{1}{4}\varepsilon_0 E_0^2 \left( \sqrt{\frac{\pi}{2}} \right) L_y dS \quad (\text{J}). \quad (5.6)$$

Here,  $dS$  denotes the cross-section of the cluster in the  $(x, z)$  plane. By using Eq. (5.4), Eq. (5.6) becomes as follows:

### Three dimensional configuration

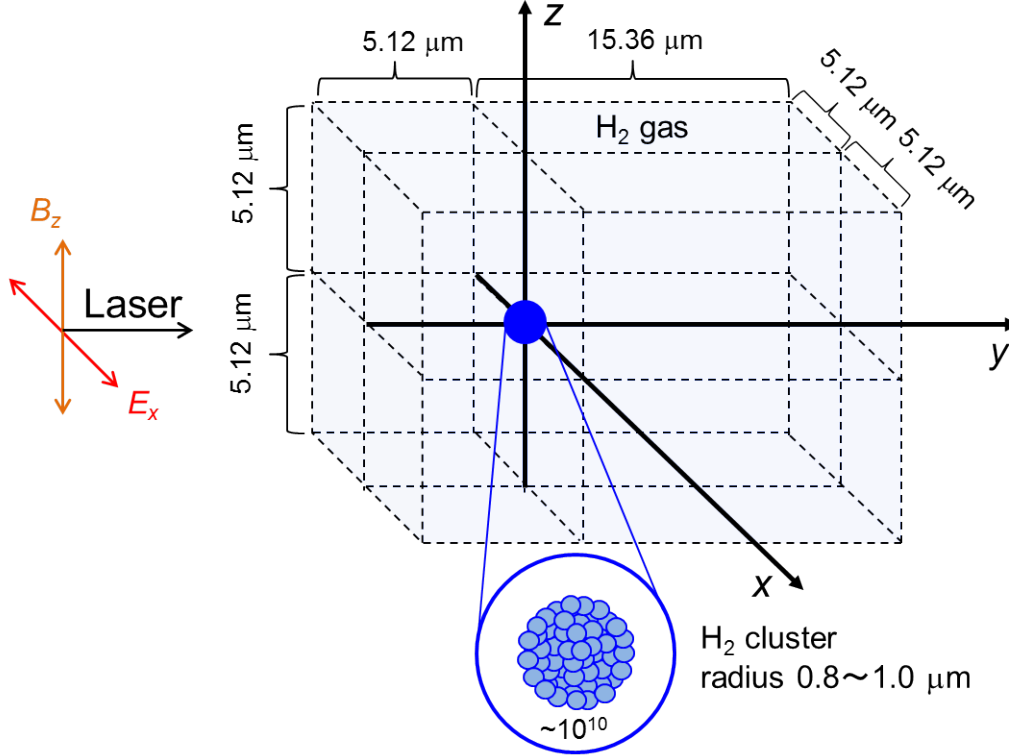


Figure 5.2: Three dimensional configurations of simulation setup. The hydrogen cluster is located at  $(x, y, z) = (0, 0, 0)$ . Ambient hydrogen gas is initially removed from the cluster area. Laser irradiation occurs at  $t = 0$  fs and the laser pulse propagates in the  $+y$  direction.

$$E_{in} = \frac{\pi}{4} dS \tau I \text{ (J)}. \quad (5.7)$$

In the present case,  $I$ ,  $\tau$  and  $dS$  are  $1.0 \times 10^{22}$  ( $\text{W}/\text{cm}^2$ ),  $40 \times 10^{-15}$  (s) and  $\pi \times (0.8 \times 10^{-4})^2$  ( $\text{cm}^2$ ), respectively. Then,  $E_{in}$  is approximately 6.3 (J).

The pulse peak passes through the cluster center at  $t = 56.3$  fs. For the fields and particles, a periodic boundary condition is employed in the  $x$  and  $z$  directions, and a transparent boundary condition is employed in the  $y$  direction. These parameters are employed based on the production of micron-size hydrogen clusters [69] and the achievement of  $10^{22}$   $\text{W}/\text{cm}^2$  focused laser intensity [137, 138].

5.3. PROTON ACCELERATION BY INTRA-CLUSTER COLLISIONLESS SHOCK  
( $R=0.8 \mu\text{M}$ )

---

Table 5.1: System parameters

species	values
$x$	$-5.12 \leq x \leq 5.12 \mu\text{m}$
$y$	$-5.12 \leq y \leq 15.36 \mu\text{m}$
$z$	$-5.12 \leq z \leq 5.12 \mu\text{m}$
Mesh numbers $N_x$	128
Mesh numbers $N_y$	256
Mesh numbers $N_z$	128
Grid size $\Delta_x$	80 nm
Grid size $\Delta_y$	80 nm
Grid size $\Delta_z$	80 nm
Time step $\Delta t$	$6.67 \times 10^{-18}$ fs
Boundary conditions	periodic in $x$ and $z$ directions and transparent in $y$ direction for both particles and fields

Table 5.2: Cluster medium (Cluster+Ambient gas)

species	values
Cluster species	Hydrogen
Cluster radius	$R_0=0.6, 0.8, 1.0 \mu\text{m}$
Cluster ion density	$4.6 \times 10^{22} \text{ cm}^{-3}$
Cluster electron density	$4.6 \times 10^{22} \text{ cm}^{-3}$
Particle numbers (Cluster ions)	28180000
Gas species	Hydrogen
Gas ion density	$4.0 \times 10^{19} \text{ cm}^{-3}$
Gas electron density	$4.0 \times 10^{19} \text{ cm}^{-3}$
Gas area ( $x, z$ )	$-5.12 \leq (x, z) \leq 5.12 \mu\text{m}$
Gas area $y$	$-5.12 \leq y \leq 15.36 \mu\text{m}$
Particle numbers (Gas ions)	24690000

5.3. PROTON ACCELERATION BY INTRA-CLUSTER COLLISIONLESS SHOCK  
( $R=0.8 \mu\text{M}$ )

---

Table 5.3: Laser parameters

species	values
Laser type	pulse laser (Gaussian)
Peak intensity	$1.0 \times 10^{22} \text{ W cm}^{-2}$
Normalized amplitude	$a_0 = 69$
Wavelength	$0.81 \mu\text{m}$
Critical density	$1.7 \times 10^{21} \text{ cm}^{-3}$
Pulse width	33 fs (Full Width at Half Maximum)
Antenna position	$-4.96 \mu\text{m}$
Polarization	Linearly polarized (P)
Propagation	$+y$ direction
Electric field	$x$ direction
Magnetic field	$z$ direction

### 5.3. PROTON ACCELERATION BY INTRA-CLUSTER COLLISIONLESS SHOCK ( $R=0.8 \mu\text{M}$ )

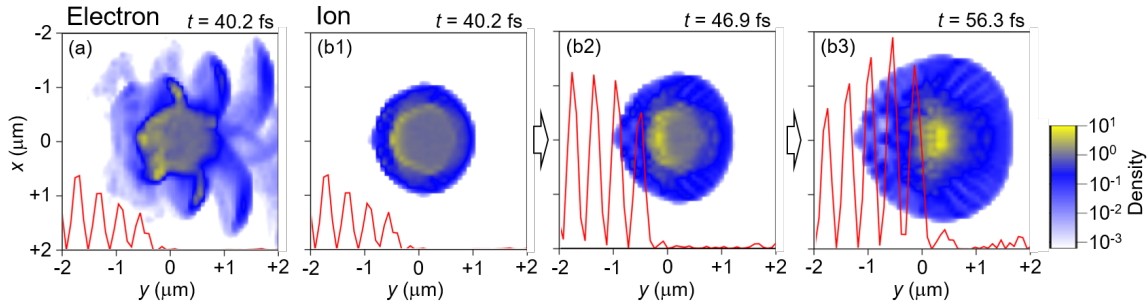


Figure 5.3: (a) Two-dimensional images of the density distributions of cluster electrons in the  $x - y$  plane at  $z = 0 \mu\text{m}$  at  $t = 40.2$  fs. (b) Two-dimensional images of the density distributions of cluster ions in the  $x-y$  plane at  $z = 0 \mu\text{m}$  at (b1)  $t = 40.2$  fs, (b2)  $t = 46.9$  fs and (b3)  $t = 56.3$  fs. Here, the densities are shown as an averaged value over  $z = 0 \pm 0.16 \mu\text{m}$  and are normalized by the initial density of the cluster ions. The laser pulse electric fields along the  $y$  axis are shown in red solid lines.

#### 5.3.2 Generation of quasimonoenergetic protons

Figure 5.3 shows the 2D images for electrons and ions density distributions for the case with  $R_0 = 0.8 \mu\text{m}$ . When a leading edge of the laser pulse reaches the spherical cluster target at  $t = 40.2$  fs, the laser field expels electrons from the peripheral region of the cluster, which corresponds to the initial electron skin depth  $\delta_e = 25$  nm, whereas most electrons remain inside the cluster core [Fig. 5.3(a)]. Here,  $\delta_e$  includes the relativistic effect and is defined as  $c/\sqrt{\omega_p^2 - \omega_L^2}$ , where  $c$  is the speed of light and  $\omega_p = \sqrt{4\pi e^2 n_e / \gamma_e m_e}$  (the Lorentz factor  $\gamma_e$  is defined as  $\gamma_e = \sqrt{1 + a_0^2/2}$  for a linearly polarized laser pulse).

The peripheral region of the cluster ( $R_0 - \delta_e \leq r \leq R_0$ ) is positively charged and undergoes the Coulomb explosion on a femtosecond-picosecond time scale, whereas the cluster core expands on a hydrodynamic time scale (picosecond-nanosecond).

As the laser intensity increases, a charge separation is induced at the surface of the laser-irradiated hemisphere via the action of the laser ponderomotive force on the remaining core electrons, and then a crescent-shaped collisionless shock is launched [see Fig. 5.3(b1)]. The shock propagates inward while maintaining the crescent shape [see Fig. 5.3(b2)] and converges at the sphere center at  $t = 56.3$  fs in accordance with the timing when the pulse peak reaches the cluster center [see Fig. 5.3(b3)]. Here, the shock Mach number is calculated as  $M_{sh} = 1.3$  using the shock velocity  $v_{sh} = 0.20c$  and the ion-acoustic velocity  $c_s = 0.15c$ , defined as  $c_s = \sqrt{\gamma k_B (T_e + T_i) / m_i}$ , where  $k_B$ ,  $T_e$ ,  $T_i$ , and  $m_i$  are the Boltzmann's constant, the electron temperature, the ion temperature, and the proton mass, respectively. Here,  $\gamma$  is  $(N + 2)/N$  and  $N$  is degrees of freedom. In the present case,  $N$  is 3 (three dimension).

Figure 5.4 shows the temporal evolution for the electron and ion densities inside the shock region and the electric field  $E_y$  associated with the shock. During the propagation of the shocks, both the electron and ion densities inside the shock gradually increase because

### 5.3. PROTON ACCELERATION BY INTRA-CLUSTER COLLISIONLESS SHOCK (R=0.8 $\mu\text{M}$ )

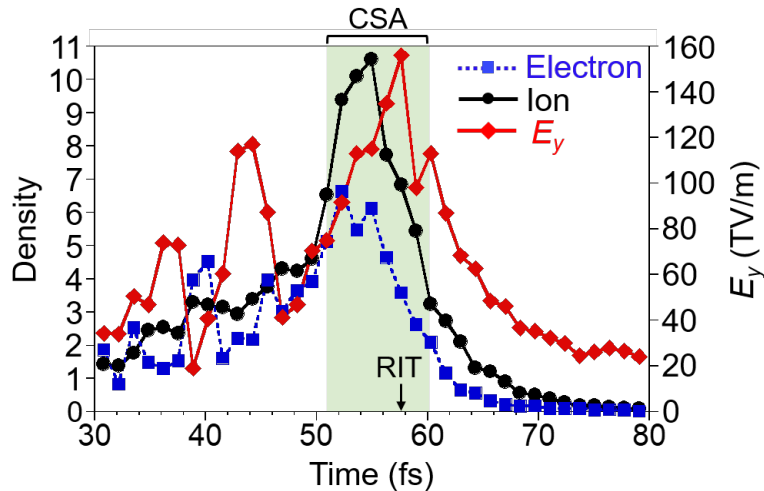


Figure 5.4: Time evolution of the electron density (blue square), the ion density (black circle), and the electric field intensity of  $E_y$  (red diamond) inside the shock along the  $y$  axis at  $x = z = 0 \mu\text{m}$ . The densities are normalized by the initial density of the cluster ions. The time region when the CSA occurs is colored green. The arrow indicates the time when the quasimonoenergetic proton bunch is pushed out via the effect of the RIT.

of the accumulation of the charged particle by the converging effect. Notably, after  $t = 50.9$  fs, the ion density inside the shock sharply increases and well exceeds the electron density. In principle, when the shock potential is larger than the kinetic energy of the upstream ions in the shock-rest frame, a so-called CSA process begins. The shock front can produce a quasimonoenergetic ion bunch by accelerating the upstream ions by reflecting them to double the shock velocity [55]. Indeed, at  $t = 50.9$  fs, the potential of the shock  $e\Phi = 10$  MeV becomes larger than the kinetic energy of the upstream protons  $(\gamma_i - 1)m_i c^2 = 6.7$  MeV in the shock-rest frame, thereby enabling the CSA of upstream protons. The reflected upstream protons have the maximum velocity of  $v_{ion} = 2v_{sh} - v_{exp} = 0.27c$ , corresponding to the proton energy of 33 MeV [see Fig. 5.5(b1)].

At  $t = 56.3$  fs, the pulse peak and the shock front reach the cluster center at the same time. After this moment, the effect of a so-called RIT [54,129,130] becomes dominant: The laser fields start to penetrate into the shock structure because the skin depth  $\delta_e$  becomes comparable to the thickness of the shock because of the relativistic effect, whereas the peak electron density inside the shock remains larger than a relativistic critical density  $\gamma_e n_c$  (see Fig. 5.6). As a result, a number of electrons inside the shock are rapidly heated and expelled in the longitudinal direction via the laser ponderomotive force. Therefore, the electric field associated with the shock reaches a maximum and quickly decreases as shown in Fig. 5.4: Indeed, the shock velocity  $v_{sh}$  temporarily increases from  $0.20c$  ( $t = 56.3$  fs) up to  $0.41c$  ( $t = 57.6$  fs) and then recovers to  $0.20c$  ( $t = 58.9$  fs). During this process, a quasimonoenergetic proton bunch is pushed out from the shock surface in a manner similar to the firing of a *bullet* (see Fig. 5.8).

### 5.3. PROTON ACCELERATION BY INTRA-CLUSTER COLLISIONLESS SHOCK (R=0.8 $\mu\text{M}$ )

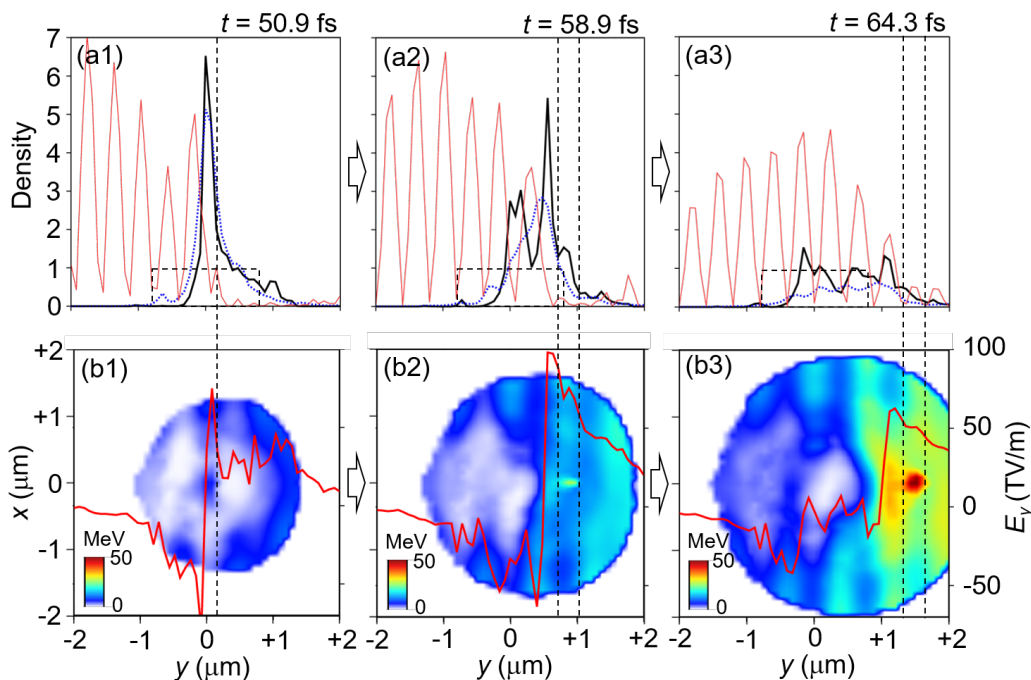


Figure 5.5: One-dimensional cross-sectional views for the charge density distributions of the cluster ions (black solid line) and cluster electrons (blue line) and the intensity of the laser electric field  $E_x^2$  (red solid line) along the  $+y$  direction at  $x = z = 0 \mu\text{m}$ , at (a1)  $t = 50.9$  fs, (a2)  $t = 58.9$  fs and (a3)  $t = 64.3$  fs. The densities are normalized by an initial density of the cluster ions, and the laser electric fields are normalized by the peak laser intensity of  $E_{x,max}^2 [= 7.6 \times 10^{24} (\text{V/m})^2]$ . Two-dimensional images of the kinetic energy distributions of cluster ions in the  $x$ - $y$  plane at  $z = 0 \mu\text{m}$  at (b1)  $t = 50.9$  fs, (b2)  $t = 58.9$  fs and (b3)  $t = 64.3$  fs. The ion energies are shown as an averaged value over  $z = 0 \pm 0.16 \mu\text{m}$ . The electric fields  $E_y$  are also shown as red solid lines. Rectangular broken lines in (a1)-(a3) represent the initial density of cluster ions. The vertical broken lines in (a1)-(a3) and (b1)-(b3) represent the location of the proton bunch.

Figure 5.7 shows the phase space distribution of cluster ions at different times. The released quasimonoenergetic proton bunch located at  $y = +0.9 \mu\text{m}$  [Fig. 5.7(b)] has the maximum velocity of  $v_{ion} = 2v_{sh} - v_{exp} = 0.42c$ , corresponding to the proton energy of 95 MeV.

Another important role of the RIT is its ability to enhance the monochromaticity of the bunch, which we define as  $1/\sigma_E$  ( $\sigma_E = \delta E/E$ : energy spread), because the pushed-out protons having a higher velocity chase the leading protons, thereby causing the compression of the proton bunch. As will be discussed later, without the effect of the RIT, the monochromaticity of the proton bunch becomes worse.

After the onset of the RIT as shown in Fig. 5.4, the electron density inside the shock decreases drastically. The shock structure collapses and the intensity of  $E_y$  rapidly decreases with time (see Fig. 5.4), leading to the end of the CSA at  $t = 60.3$  fs. At

### 5.3. PROTON ACCELERATION BY INTRA-CLUSTER COLLISIONLESS SHOCK ( $R=0.8 \mu\text{M}$ )

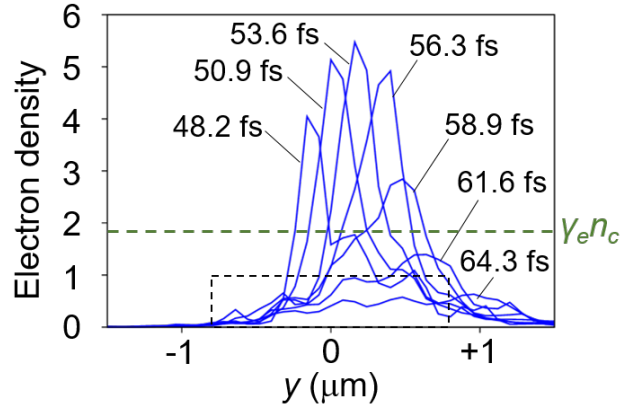


Figure 5.6: One-dimensional cross-sectional views for the charge density distributions of cluster electrons along the  $+y$  direction at  $x = z = 0 \mu\text{m}$  at different times. Rectangular broken line represents the initial density of cluster electrons.

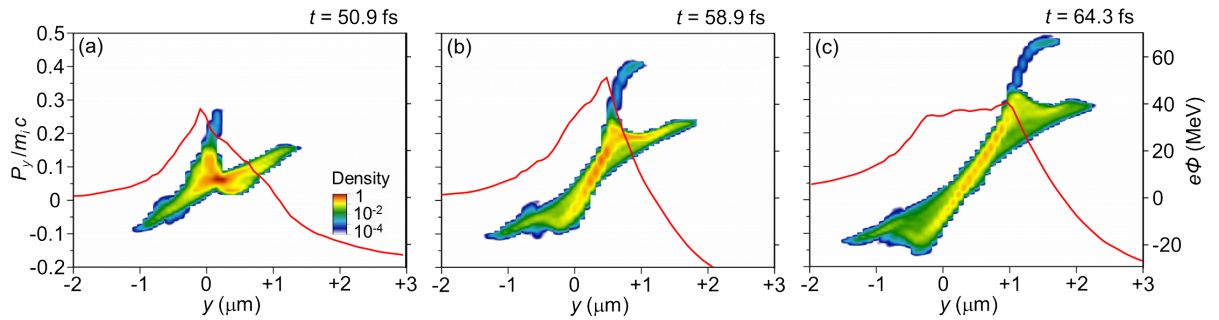


Figure 5.7: The phase space distribution of the cluster ions on the  $y$  axis at  $x = z = 0 \mu\text{m}$  at (a)  $t = 50.9 \text{ fs}$ , (b)  $t = 58.9 \text{ fs}$  and (c)  $t = 64.3 \text{ fs}$ , which is normalized by the initial density of cluster ions and displayed on a log scale. The electrostatic potential is also shown as red solid lines.

this moment, the proton bunch is accelerated up to  $0.45c$ , corresponding to the proton energy of 108 MeV. After the CSA as shown in Fig. 5.5(b3), the proton bunch is further accelerated by the remnant electric field of the shock inside the cluster. Over time, at  $t = 75.8 \text{ fs}$ , the proton bunch reaches the cluster exploding front with  $v_{ion} = 0.60c$ , corresponding to the proton energy of 211 MeV. At this moment, the velocity of the cluster exploding front in the  $+y$  direction is  $0.40c$ ; thus, the proton *bunch* flies out from the cluster at a  $4.3^\circ$  half-divergence angle (see Fig. 5.8).

After leaving the cluster, the proton *bunch* is again further accelerated by the sheath electric field created by the Coulomb explosion of the cluster. At this acceleration stage, the maximum attainable energy of the bunch can be estimated as  $K_{max} = 300 \text{ MeV}$ , using the relation

5.3. PROTON ACCELERATION BY INTRA-CLUSTER COLLISIONLESS SHOCK  
( $R=0.8 \mu\text{M}$ )

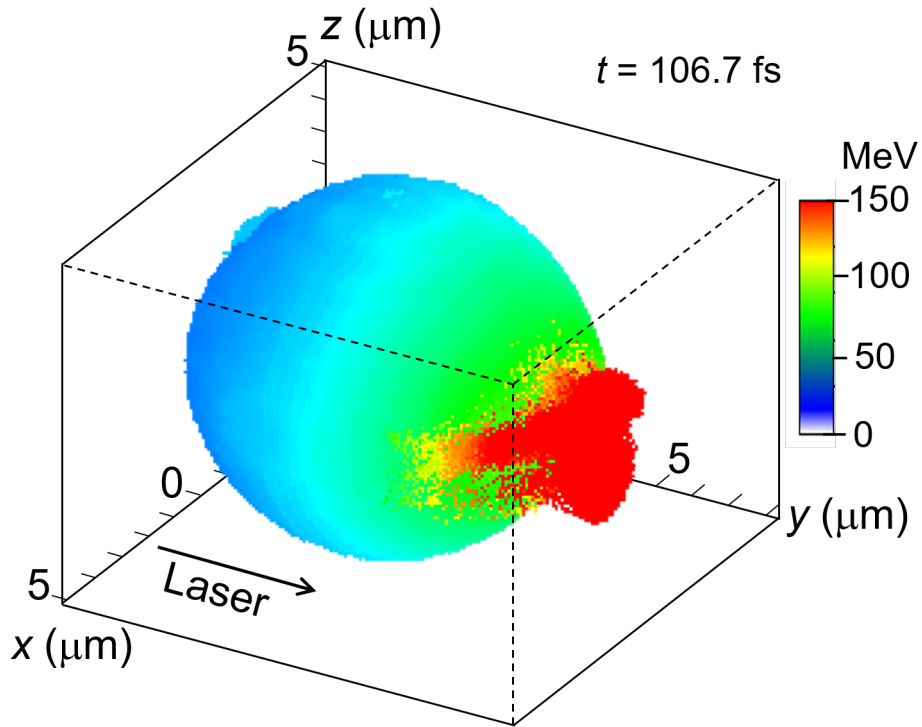


Figure 5.8: Kinetic energy spatial distribution of cluster ions at  $t = 106.7$  fs.

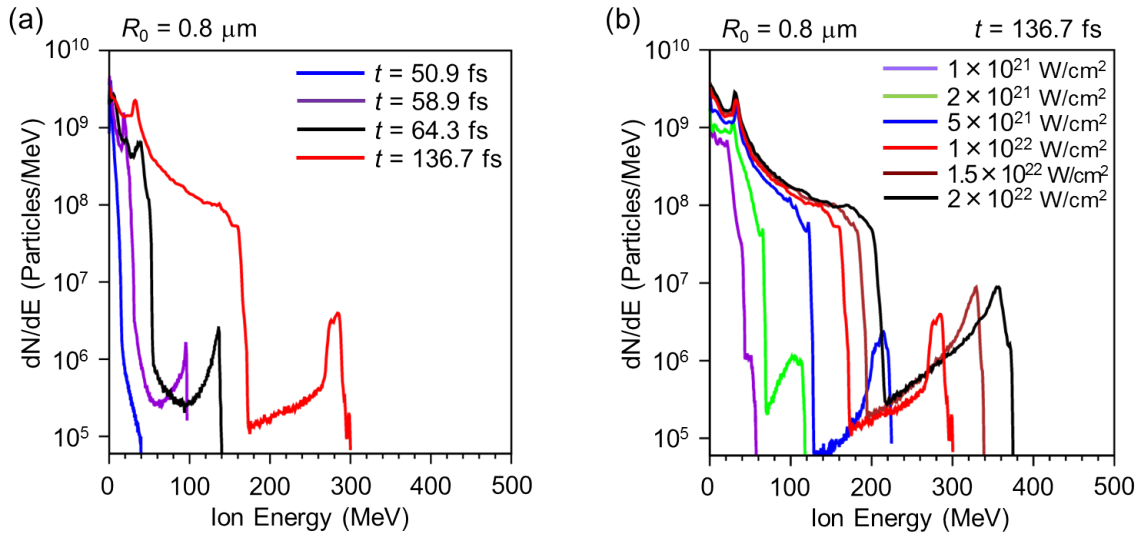


Figure 5.9: (a) Proton energy spectra for clusters with  $R_0 = 0.8 \mu\text{m}$  at different times. (b) Proton energy spectra for clusters with  $R_0 = 0.8 \mu\text{m}$  for different laser peak intensity  $I$ . The proton number is evaluated using a real value by multiplying the particle weight to the PIC particle.

$$K_{max} = K_0 + \int_{r_0}^{\infty} eE(r) dr, \quad (5.8)$$

where  $K_0 = 211$  MeV is the kinetic energy of the bunch at the cluster exploding front,  $r_0$  is the distance of the cluster exploding front from the cluster center, and  $E(r) \propto 1/r^2$  is the electric field of the Coulomb explosion outside of the cluster as a function of the distance  $r$  from the cluster center. In this study, the simulation has been performed up to  $t = 136.7$  fs and the maximum kinetic energy of the bunch has a quasimonoenergetic peak at 290 MeV, which is close to the estimated maximum attainable kinetic energy, with an energy spread of  $\sigma_E = \delta E/E \sim 7\%$  [red solid line in Fig. 5.9(a)]. Here, the energy  $E$  is evaluated at the peak energy of the quasimonoenergetic component in the energy spectrum. The conversion efficiency of the irradiated laser energy into kinetic energy of protons is approximately 8.3% and that into kinetic energy of quasimonoenergetic protons is approximately 0.042%. Notably, the bunch energy 290 MeV is much larger than the maximum proton energy 170 MeV accelerated by the Coulomb explosion of the hydrogen cluster [red solid line in Fig. 5.9(a)].

### 5.3.3 Effect of the magnetic field of the laser

Here, we discuss the effect of the magnetic field of the laser. The laser peak intensity  $I$  and the peak electric field of the laser  $E_0$  satisfy the following relation,

$$I (\text{W}/\text{cm}^2) = 13.272 \times 10^{-8} \times \{E_0(\text{V}/\text{m})\}^2. \quad (5.9)$$

$$\therefore E_0 (\text{V}/\text{m}) = 2.74 \times 10^3 \times \{I(\text{W}/\text{cm}^2)\}^{\frac{1}{2}}. \quad (5.10)$$

The peak magnetic field of the laser  $B_0$  (T) is represented by  $B_0 = E_0/c$ , where  $c$  is the light speed. Then, the laser peak intensity  $I$  and the peak magnetic field of the laser  $B_0$  satisfy the following relation,

$$B_0 (\text{T}) = 9.15 \times 10^{-6} \times \{I(\text{W}/\text{cm}^2)\}^{\frac{1}{2}}. \quad (5.11)$$

### 5.3. PROTON ACCELERATION BY INTRA-CLUSTER COLLISIONLESS SHOCK ( $R=0.8 \mu\text{M}$ )

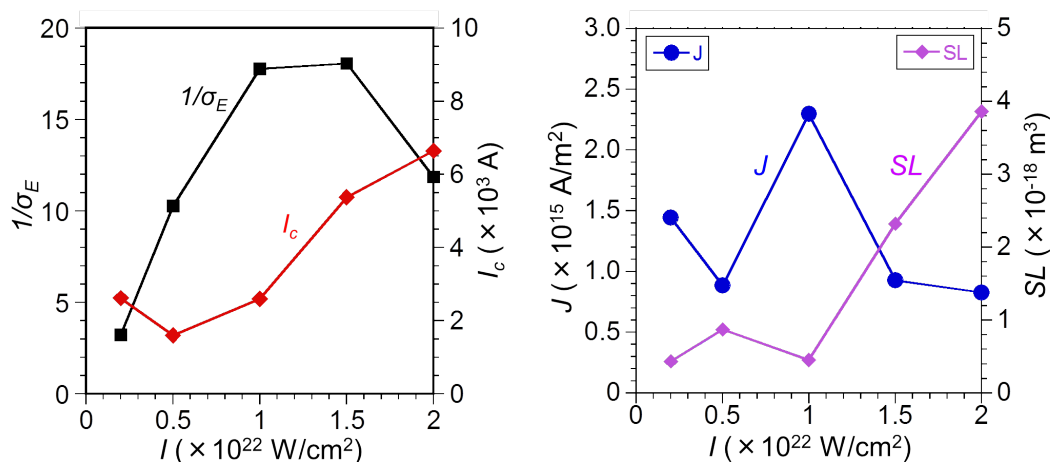


Figure 5.10: (a) The monochromaticity  $1/\sigma_E$  (black square) and the current  $I_c$  (red diamond) for the bunch within  $\sigma_E$ . (b) The current density  $J$  and the volume of quasimonoenergetic component within  $\sigma_E$ . Here,  $J$  is calculated by  $J = I_c/SL$ .

By using this relation, the intensity of laser magnetic field  $\mathbf{B}$  is calculated as approximately  $915 \text{ (kT)} = 9.15 \times 10^9 \text{ (G)}$  [ $1 \text{ (T)} = 10^4 \text{ (G)}$ ] at  $1.0 \times 10^{22} \text{ W/cm}^2$  and corresponding Larmor radius of electrons and protons are estimated to be approximately  $0.5 \mu\text{m}$  and  $2 \mu\text{m}$ , respectively. However, in this case, both electrons and ions are not confined in the  $(x, y)$  plane. This is because the time scale of gyration motion of particles is longer than the pulse width ( $\sim 33 \text{ fs}$  at FWHM). Instead, electrons are moved forward (in the  $+y$  direction) with a figure-eight motion as shown in Fig. 5.3(a) due to the magnetic component of the Lorentz force, i.e.,  $e\mathbf{v} \times \mathbf{B}$ . As a result, the intensity of the sheath electric field created around the cluster exploding front becomes anisotropic and shows the maximum value at the front where the quasimonoenergetic proton bunch flies out. This means that the bunch is suffered from the large electric field and is directed forward. Moreover, the large  $\mathbf{B}$  field essentially contributes to the onset of collisionless shock through the ponderomotive force. Therefore, we consider that the large  $\mathbf{B}$  field plays an essential role in the onset of the collisionless shock and resulting shock acceleration, and contributes to the maximum energy of the bunch.

#### 5.3.4 Dependence of laser intensity

The effect of the laser peak intensity  $I$  on the quasimonoenergetic proton bunch formation for  $R_0 = 0.8 \mu\text{m}$  is investigated in the range of  $1.0 \times 10^{21}$  to  $2.0 \times 10^{22} \text{ W/cm}^2$ , which is shown in Fig. 5.9(b). The bunch (energy spread  $\sigma_E \sim 10\%$ ) is found to be formed for  $I > 2.0 \times 10^{21} \text{ W/cm}^2$ . This indicates that the threshold value concerning the laser peak intensity exists for the multiple processes to be synchronized, leading to the bunch formation. The threshold value roughly coincides with that causing the RIT, which is the driving force to compress the bunch at the shock surface. The energy [Fig. 5.9(b)] and

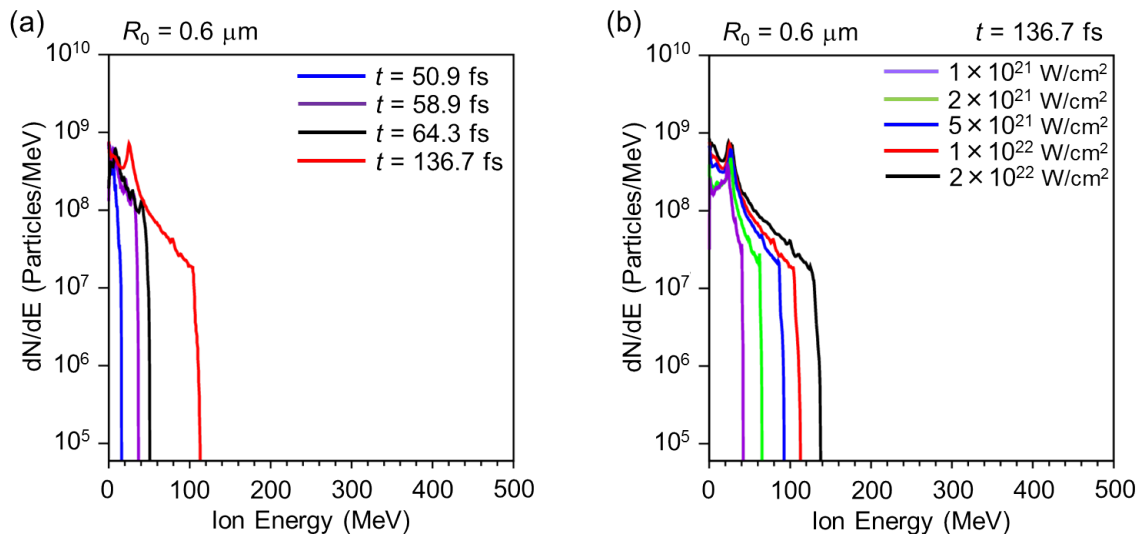


Figure 5.11: (a) Proton energy spectra for clusters with  $R_0 = 0.6 \mu\text{m}$  at different times. (b) Proton energy spectra for clusters with  $R_0 = 0.6 \mu\text{m}$  for different laser peak intensity  $I$ . The proton number is evaluated using a real value by multiplying the particle weight to the PIC particle.

the current  $I_c$  [Fig. 5.10(a)] for the bunch within  $\sigma_E$  increase with  $I$ . Notably, the bunch size increases with the current  $I_c$  due to the space-charge effect as seen in Fig. 5.10(a)(b). Namely, the optimum laser peak intensity for the maximum current density  $J$  is found to exist. The monochromaticity  $1/\sigma_E$  also increases with  $I$ , reaching the maximum value around  $I = (1.0-1.5) \times 10^{22} \text{ W/cm}^2$ , while decreases for further increase with  $I$  [Fig. 5.10(a)].

These results show that the optimum laser peak intensity exists for the formation of the bunch with the maximum monochromaticity and current density.

## 5.4 Dependence of the cluster size

### 5.4.1 Proton acceleration for $R=0.6 \mu\text{m}$

In order to investigate the effect of the cluster size, we changed the cluster size from  $0.8 \mu\text{m}$  to  $0.6 \mu\text{m}$ . In the smaller cluster case of  $R_0 = 0.6 \mu\text{m}$ , for  $I = 1.0 \times 10^{22} \text{ W/cm}^2$ , the bunch is not formed and the energy spectrum shows only the feature of the Coulomb explosion, i.e., the cut-off structure at 117 MeV [red line in Fig. 5.11(a)]. This is because the height of the shock potential does not reach enough value to reflect upstream protons due to the limited mass of the cluster when the RIT occurs. As a result, the shock structure collapses before the onset of the CSA. Figure 5.12 shows phase space distribution of protons for clusters with  $R_0 = 0.6 \mu\text{m}$  at different times. As shown in Fig. 5.12(a), when the crescent-shaped converging shock reaches the cluster center at  $t = 50.9$

## 5.4. DEPENDENCE OF THE CLUSTER SIZE

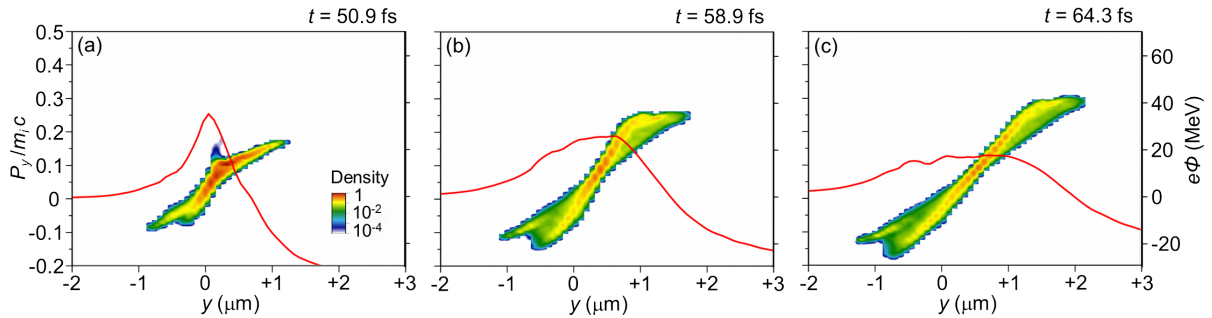


Figure 5.12: The phase space distribution of the cluster ions with  $R_0 = 0.8 \mu\text{m}$  on the  $y$  axis at  $x = z = 0 \mu\text{m}$  at (a)  $t = 50.9$  fs, (b)  $t = 58.9$  fs and (c)  $t = 64.3$  fs, which is normalized by the initial density of cluster ions and displayed on a log scale. The electrostatic potential is also shown as red solid lines.

fs, the intensity of the shock is small compared with that in the case with  $R_0 = 0.8 \mu\text{m}$  [see Fig. 5.7(a)]. As time goes on, the peak intensity of the laser pulse hits the shock structure at  $t = 56.3$  fs, leading to the RIT. As a result, shock structure disappears and only the feature of the Coulomb explosion appears as seen in Figs. 5.12(b) and 5.12(c).

The effect of the laser peak intensity  $I$  is also investigated in the range of  $1.0 \times 10^{21}$  to  $2.0 \times 10^{22}$  W/cm<sup>2</sup>, which is shown in Fig. 5.11(b). In all cases, the quasimonoenergetic proton bunch is not formed. This indicates that the threshold value concerning the cluster radius exists.

### 5.4.2 Proton acceleration for $R=1.0 \mu\text{m}$

The effect of the initial cluster radius is investigated by choosing  $R_0 = 1.0 \mu\text{m}$  in Fig. 5.13(a). In the large cluster case, the general tendency is similar to that for  $R_0 = 0.8 \mu\text{m}$ , indicating that the same acceleration mechanisms, i.e., the onset of the crescent-shaped collisionless shock on the laser-irradiated hemisphere, propagation of the collisionless shock into the cluster center with converging, collisionless shock acceleration and the onset of the RIT, are effective for  $I > 2.0 \times 10^{21}$  W/cm<sup>2</sup> [see Fig. 5.13(b)]. However, the monochromaticity becomes worse ( $\sigma_E \sim 30\text{--}40\%$ ) as seen in Fig. 5.13(b), compare to the case for  $R_0 = 0.8 \mu\text{m}$  ( $\sigma_E \sim 10\%$ ). This is because the RIT occurs before the shock convergence at the cluster center, so that a slope of the electric field associated with the shock is less steep as seen in Fig. 5.14.

These results indicate that the threshold value concerning the cluster radius for the quasimonoenergetic proton bunch formation exists around  $0.6 < R_0 < 0.8 \mu\text{m}$ , while the monochromaticity becomes worse for  $R_0 > 0.8 \mu\text{m}$ .

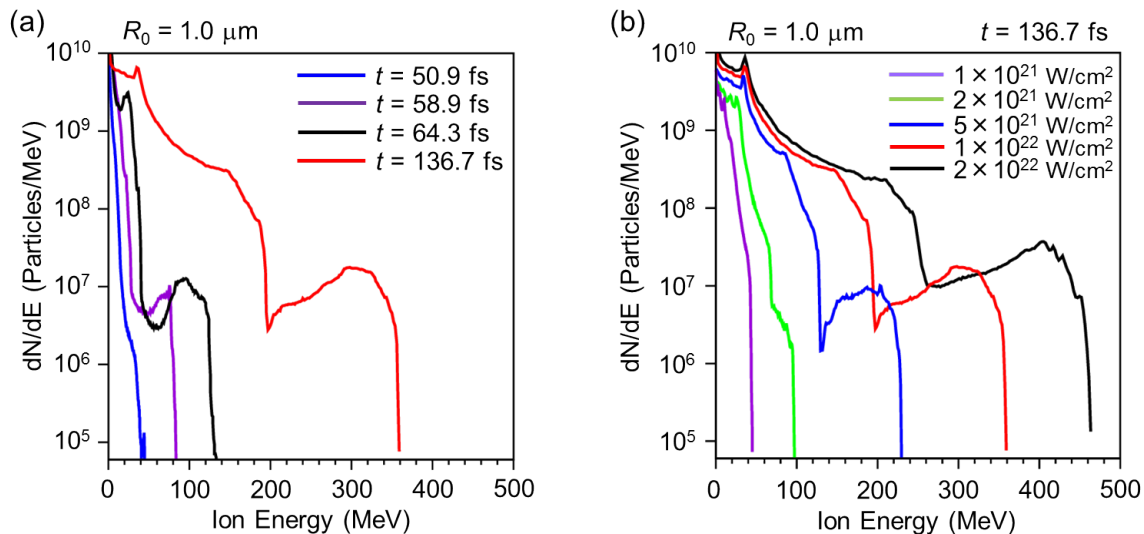


Figure 5.13: (a) Proton energy spectra for clusters with  $R_0 = 1.0 \mu\text{m}$  at different times. (b) Proton energy spectra for clusters with  $R_0 = 1.0 \mu\text{m}$  for different laser peak intensity  $I$ . The proton number is evaluated using a real value by multiplying the particle weight to the PIC particle.

## 5.5 Density dependence / Effect of prepulse

We also investigated the effect of the cluster electron density is also investigated while keeping  $I = 1.0 \times 10^{22} \text{ W/cm}^2$ . For the case of a carbon cluster with  $R_0 = 0.8 \mu\text{m}$  and  $n_e = 2.8 \times 10^{23} \text{ cm}^{-3}$ , the hemispherically converging collisionless shock is launched; however, it disappears before the onset of the CSA. Moreover, the RIT does not take place because  $\gamma_e n_c = 8.3 \times 10^{22} \text{ cm}^{-3}$  at the laser pulse peak is below  $n_e$  and  $\delta_e$  also decreases compared with the hydrogen cluster case. Therefore, for the proposed ion acceleration mechanism to work, at least  $n_e$  should be below  $\gamma_e n_c$  for a given laser peak intensity.

Finally, the preheating effect of the hydrogen cluster by the prepulse is considered. For example, J-KAREN-P laser has two kinds of prepulses, i.e., the early ( $\sim 100$  picosecond) one with the contrast of  $10^{10}$  and the later ( $\sim 40$  picosecond) one with the contrast of  $3 \times 10^8$  [138] and the energy containing in the former and later prepulses are approximately  $3 \times 10^{-9} \text{ J}$  and  $1 \times 10^{-7} \text{ J}$ , respectively. By taking into account the preheating of hydrogen cluster by these prepulses, the energy of these prepulses are expended as heat of melting and vaporization, binding energy and ionization energy. As a result,  $0.8 \mu\text{m}$ -radius hydrogen cluster hydrodynamically expands and the cluster geometry is estimated to be  $0.7 \mu\text{m}$ -radius spherical cluster with having the exponential decay around the surface when the main pulse reaches the cluster. Therefore, we performed simulation such cluster geometry as an initial condition. From simulation results, we also obtained high energy protons with a quasimonoenergetic peak ( $\sigma_E \sim 10\%$ ) at  $220 \text{ MeV}$ . This indicates that the effect of the laser contrast is considered to decrease the cluster size by approximately  $10\%$ , but does not significantly affect the proposed acceleration mechanism for the cluster

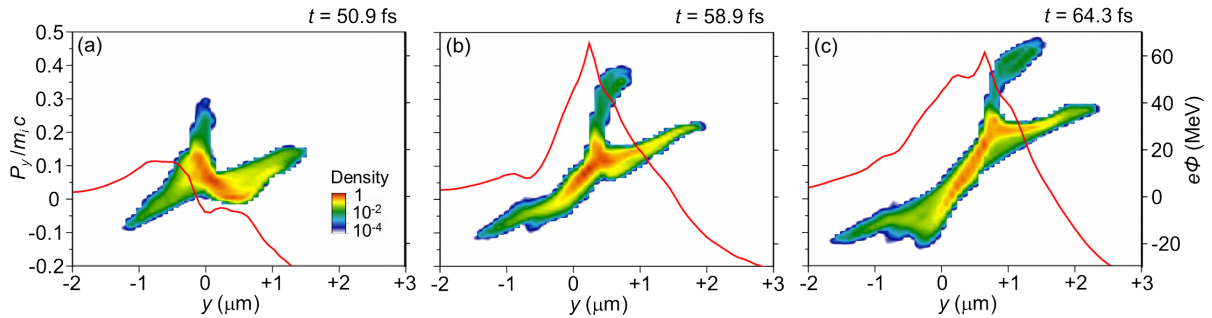


Figure 5.14: The phase space distribution of the cluster ions with  $R_0 = 1.0 \mu\text{m}$  on the  $y$  axis at  $x = z = 0 \mu\text{m}$  at (a)  $t = 50.9$  fs, (b)  $t = 58.9$  fs and (c)  $t = 64.3$  fs, which is normalized by the initial density of cluster ions and displayed on a log scale. The electrostatic potential is also shown as red solid lines.

with a radius of  $R \geq 0.8 \mu\text{m}$ .

## 5.6 Summary

In summary, we presented a new scheme for achieving high-energy quasimonoenergetic protons by causing multiple processes created through the internal and external degree of freedom ascribed to the spherical structure of micron-size hydrogen cluster irradiated by high-intensity laser and by synchronizing their spatial-temporal evolutions. We presented the scheme by utilizing a series of numerical studies using a three-dimensional (3D) particle-in-cell (PIC) method to introduce a new methodology in the field of laser ion acceleration to produce a highly directional quasimonoenergetic proton bullet with energy close to 300 MeV, which has not been demonstrated to date.

By the action of an ultrashort PW class laser pulse with a focused intensity of  $I = 1.0 \times 10^{22} \text{ W/cm}^2$  onto a micron-size spherical hydrogen cluster target, the crescent-shaped collisionless shock is launched at the laser-irradiated hemisphere and propagates inward. The multiple processes producing highly-directional and high-energy quasimonoenergetic proton punch reaching 300 MeV are below:

- Collisionless shock is launched on the laser-irradiated hemisphere of the cluster.
- Crescent-shaped shock propagates into the cluster center with converging.
- Collisionless shock acceleration (CSA) starts when the shock reaches the cluster center, leading to the formation of the quasimonoenergetic proton bunch.
- Relativistic induced transparency (RIT) contributes to the enhancement of the monochromaticity of the proton bunch.
- The proton bunch is further accelerated by the remnant of the shock electric field in the inside of the cluster.

## 5.6. SUMMARY

---

- The proton bunch is again further accelerated by the sheath electric field in the outside of the cluster.

The important point of our research is that the proposed method can be realized using currently available experimental techniques, thereby opening a new avenue for practical applications of laser accelerated protons, including proton therapy for cancer treatment that uses energy protons in the therapeutic energy window of interest between 60 and 250 MeV. In addition, the new physical findings showing that a quasimonoenergetic proton bunch is released from the shock surface similar to the firing of a bullet is achieved via a hemispherically converging collisionless shock created in laser-cluster interactions in the relativistic transparency regime, thereby solving the most difficult problem that has hindered the wider use of laser ion acceleration technology.

At present, the laser focal spot size is small for PW class laser. For example, concerning J-KAREN-P [136–138] laser system at KPSI-QST, the laser focal spot size of  $FW1/e^2$  and FWHM are  $\sim 2.2 \mu\text{m} \times 2.3 \mu\text{m}$  and  $\sim 1.3 \mu\text{m} \times 1.4 \mu\text{m}$  respectively [137]. In this case, only when the pulse peak of the laser coincides with the cluster center, a  $1.6\text{-}\mu\text{m}$  diameter cluster is almost covered with the laser focal spot size (FWHM) of  $I > 5 \times 10^{21} \text{ W/cm}^2$ , which exceeds the critical laser intensity for the quasimonoenergetic proton bunch formation as discussed above. However, the spatial intensity distribution of the laser pulse has possibilities to work in a negative way for hemispherically converging collisionless shock. Accordingly, in order for our proposed mechanism to stably work, the larger laser focal spot size is required. Therefore, further development of the laser technology, e.g., multi-PW class laser, would make possible the experimental achievement in the future.

In our simulation, we utilized the plane wave. Therefore, we defined the cross-section of the cluster, i.e.,  $\pi \times (0.8 \mu\text{m})^2$ , as the laser focal spot size. Then, the laser energy irradiated to the cross-section of the cluster is estimated to be approximately 6.3 J. The kinetic energy of cluster protons including quasimonoenergetic component is approximately 0.052 J. Therefore, approximately 8.3% of the irradiated laser energy is converted into the kinetic energy of protons. When we use cluster targets, composed of multi-clusters, the laser pulse has the potential to interact with multi-clusters in the longitudinal direction during the propagation. Then, the conversion efficiency of the irradiated laser energy into kinetic energy of protons is expected to increase. We will perform simulations using multi-hydrogen clusters in the next step and investigate the conversion efficiency.

Concerning the laser peak intensity, we have confirmed that the quasimonoenergetic proton bunch is formed for relatively wide range of the laser peak intensity, i.e.,  $I > 2 \times 10^{21} \text{ W/cm}^2$ . This range of the laser peak intensity is now routinely achievable using petawatt (PW) lasers worldwide. In addition, the pulse length is also easily achievable with current laser technology. Indeed, practical cluster target consists of randomly-placed and variable-sized clusters in an ambient gas. Concerning the cluster positioning, if we assume using PW laser [137], where the focal spot size ( $1/e^2$ ) is  $\sim 2.2 \mu\text{m} \times 2.3 \mu\text{m}$ , the probability of laser pulse hitting the micron-size cluster is estimated to be low ( $\sim 1/100$ ). The future 10 PW class laser systems will provide larger focal spot size, which will enhance the probability of laser pulse hitting cluster for more than 10 times. On the other hand,

## 5.6. SUMMARY

---

cluster sources produce clouds of clusters of a variable size and the adjustment of the cluster size remains unsolved. At present, we are trying to control the cluster size by changing the nozzle temperature [70] and also the shape of the conical nozzle. The adjustment of the cluster size and the cluster density is the on-going future work.

For medical applications, a sufficient flux of protons is also required. Indeed, from our simulations, the number of protons constituting monoenergetic peak (290 MeV at FWHM) is estimated to be  $\sim 10^8$ . However, the high-repetition rate is also an important parameter for applications. In the experimental condition, the repetition rate of producing hydrogen clusters is up to 600 Hz [135]. Therefore, when we suppose 0.8  $\mu\text{m}$ -radius hydrogen clusters are stably produced at 100 Hz with the use of future, high-repetitive-rate lasers, the number of monoenergetic protons we could obtain is estimated to be  $\sim 10^{10}$  per second, which is the comparable number of protons required for cancer therapy, i.e.,  $\sim 10^{10}$  per second [102]. On the other hand, the narrower energy spread and the lower emittance as well as further improvements of laser technology and the adjustment technique of the cluster size are also required for cancer therapy. These are the ongoing future works.

# Chapter 6

## Conclusion

### 6.1 Summary of the results

#### 6.1.1 Dynamics of boundary layer

In Chapter 2, we performed the two-dimensional (2D) particle-in-cell (PIC) simulations and investigated the dynamics of the boundary layer in between two distinct collisionless plasmas created by the expansion of the femtosecond laser-irradiated cluster in an ambient gas, and the associated acceleration of the ambient gas ions by utilizing extended particle-based integrated code, EPIC3D. We found that the dynamics of the boundary layer is classified into three successive phases, i.e., phase 1: cluster expansion with keeping the contact surface between the cluster expansion front and the compressed surface of ambient gas ions, phase 2: the formation of overlapping region between the cluster expansion front and the compressed surface, and phase 3: the collapse of the sharp structure of compressed surface as the rarefaction wave.

- In phase 1 (before  $t \sim 150$  fs), the contact surface exists during the expansion of the cluster ions and the compression of the ambient gas ions. In this phase, the ambient gas ions are reflected by the electrostatic potential associated with the ambipolar field around the contact surface, which causes the collisionless shock acceleration (CSA).
- In phase 2 ( $150 < t < 340$  fs), the contact surface disappears and the overlapping region between the cluster expansion front and the compressed surface is formed. In this phase, in addition to the ambipolar electric field around the cluster expansion front, a bipolar field is established around the compressed surface. The compressed surface propagates as the nonlinear wave, which causes the similar acceleration of ambient gas ions as that by the shock.
- In phase 3 (after  $t \sim 340$  fs), the compressed surface evolves as a rarefaction wave. The onset of the rarefaction wave is found to coincide with the termination of acceleration of ambient gas ions.

The excitation of the nonlinear waves, i.e., the ambipolar field and bipolar field, plays a central role. We found that the peak value of the ambipolar field decays quickly, while that of the bipolar field persists for a long time even after the passage of the laser pulse. This is because the nonlinear wave structure associated with the bipolar field is sustained as a quasi-stationary kinetic equilibrium established via the balance between trapped and passing electrons on the electrostatic potential. The equilibrium we reported in this paper is considered to be related to Bernstein-Greene-Kruskal (BGK) type kinetic equilibrium [117, 118].

We also studied the dynamics in a wide range of ambient gas densities. We found that various dynamics, e.g., the electric field causing shock acceleration, the time that the rarefaction waves are triggered, etc., depends on the ambient gas density, while the time that the crossing between the cluster expansion front and the compressed surface is weekly depends on the ambient gas density. However, the quasi-stationary kinetic equilibrium dominated by fast electrons is established not only in lower but also in higher density cases. The formation of such an equilibrium has been reported in space plasmas such as the plasma sheet boundary layer in the Earth's magnetotail [123] and the downward-current regions of the auroral zone [124]. The future observation of such nonlinear waves under laboratory conditions may help understand behaviors of nonlinear electrostatic waves and related particle accelerations in space and astrophysical plasmas.

On the other hand, in high density cases, the ring-like and/or staircase structure in the cluster ions is clearly observed during the destruction process of the compressed surface. Such ring-like and/or staircase structures are found to be widely observed in space and astrophysical plasmas. It is interesting to study the similarity with the present case. In future, we will study the long time-scale ( $\sim$ picosecond) dynamics.

Here, we consider the 2D case. It is valuable to discuss the effect of the dimension of the system on the dynamics and structure, specifically on the formation of the kinetic equilibrium. Since the phenomena after the laser irradiation is approximately spherically symmetric, so that one-dimensional (1D) simulation assuming electron distribution functions is possible, which would have an advantage in parametrizing the phenomena and/or deriving a scaling law. This is a future work. On the other hand, in terms of the three-dimensional (3D) effect, the establishment of the kinetic equilibrium observed in the 2D simulation is also expected to take place because it is driven by the 1D motion of electrons in the radial direction of the cluster. In future, we will perform 3D simulations and confirm the adequacy of present 2D simulations. Moreover, it is worthwhile to study the critical condition for the formation of kinetic equilibrium for other parameters such as cluster size and laser intensity, which is a next work.

### 6.1.2 Monoenergetic protons reaching 300 MeV

In Chapter 3, we introduced an approach for accelerating a quasimonoenergetic proton bunch via a hemispherically converging collisionless shock created by laser-cluster interactions at the relativistically induced transparency (RIT) regime by utilizing 3D PIC simulations. By the action of an ultrashort PW class laser pulse with a focused intensity

of  $I = 1.0 \times 10^{22}$  W/cm<sup>2</sup> onto a micron-size spherical hydrogen cluster, the crescent-shaped collisionless shock is launched at the laser-irradiated hemisphere and propagates inward. When the shock reaches the sphere center, the onset of the RIT in the dense plasma acts in conjunction with the shock to push the quasimonoenergetic proton bunch out from the shock surface in a manner similar to the firing of a bullet in the forward direction. The proton bunch is further accelerated by the remnant electric fields inside and outside of the cluster. Finally, the energy of the proton bunch reaches  $\sim 300$  MeV with  $\sim 10\%$  energy spread and a low  $\sim 5^\circ$  half-divergence angle.

This acceleration mechanism works only when the complex system consisting of multiple processes utilizing internal and external degree of freedom of spherical structure irradiated by high-intensity laser, i.e., 1) the onset of collisionless shock by an intense laser, 2) the propagation of the shock and the hemispherical convergence, 3) the bunch formation and the subsequent acceleration by the collisionless shock (CSA), 4) the onset of relativistically induced transparency (RIT), 5) further acceleration by the remnant shock electric field, and 6) that by the sheath electric field, is synchronized and self-organized.

In order to confirm the range which this mechanism works, we also performed simulations by changing the laser peak intensity  $I$  in the range of  $1.0 \times 10^{21}$  to  $2.0 \times 10^{22}$  W/cm<sup>2</sup>, and confirmed that the quasimonoenergetic proton bunch is formed for  $I > 2.0 \times 10^{21}$  W/cm<sup>2</sup> for  $0.8 \mu\text{m}$ -radius hydrogen cluster. This is because the RIT effect works for  $I > 2.0 \times 10^{21}$  W/cm<sup>2</sup> for solid hydrogen density. Namely, a threshold value concerning the laser peak intensity exists for the quasimonoenergetic bunch formation. On the other hand, the monochromaticity increases with the laser peak intensity  $I$ , reaching the maximum value at  $I \sim 1.0\text{--}1.5 \times 10^{22}$  W/cm<sup>2</sup>, and decreases. This result clearly shows that the optimum laser intensity exists at  $I \sim 1.0 \times 10^{22}$  W/cm<sup>2</sup> for the formation of the bunch with the maximum monochromaticity.

We have also performed simulations for  $0.6 \mu\text{m}$ -radius and  $1.0 \mu\text{m}$ -radius hydrogen clusters by changing the laser peak intensity  $I$ . For  $1.0 \mu\text{m}$ -radius cluster, the converging shock acceleration takes place in the range of  $I = 2.0 \times 10^{21}$  to  $2.0 \times 10^{22}$  W/cm<sup>2</sup>, while the monochromaticity becomes worse compared with that for  $0.8 \mu\text{m}$ -radius cluster. The RIT effect also works for  $I > 2.0 \times 10^{21}$  W/cm<sup>2</sup> for  $1.0 \mu\text{m}$ -radius cluster. On the other hand, for  $0.6 \mu\text{m}$ -radius cluster, the converging shock is formed, but the shock acceleration does not take place in the range of  $I = 1.0 \times 10^{21}$  to  $1.0 \times 10^{22}$  W/cm<sup>2</sup>. This is because the height of the shock potential does not reach enough value to reflect upstream protons due to the limited mass of the cluster. From these results, we concluded that the converging shock acceleration takes place and the RIT effectively works for  $I > 2.0 \times 10^{21}$  W/cm<sup>2</sup> and the optimum laser intensity which gives the maximum monochromaticity exists at  $I \sim 1.0\text{--}1.5 \times 10^{22}$  W/cm<sup>2</sup>. Moreover, the threshold value concerning the cluster radius for the quasimonoenergetic proton bunch formation exists around  $0.6 < R_0 < 0.8 \mu\text{m}$ , while the monochromaticity becomes worse for  $R_0 > 0.8 \mu\text{m}$ .

## 6.2 The meaning of this study

Combined with currently available experimental techniques, the proposed method represents a promising way of producing a highly directional, highly reproducible, impurity-free, debris-free, and quasimonoenergetic proton bunch with energy close to 300 MeV, thereby opening a new avenue for practical applications of laser accelerated protons, including proton therapy for cancer treatment that uses energetic protons in the therapeutic energy window of interest between 60 and 250 MeV.

On the other hand, the laser focal spot size is small [ $\sim 2 \times 2 (\mu\text{m})^2$ ] for PW class laser. In this case, only when the pulse peak of the laser coincides with the cluster center, a 1.6- $\mu\text{m}$  diameter cluster is almost covered with the laser focal spot size (FWHM) of  $I > 5 \times 10^{21} \text{ W/cm}^2$ , which exceeds the critical laser intensity for the quasimonoenergetic proton bunch formation. Namely, if we assume using PW laser, the probability of laser pulse hitting the micron-size cluster is estimated to be low ( $\sim 1/100$ ). The future 10 PW class laser systems will provide larger focal spot size, which will enhance the probability of laser pulse hitting cluster for more than 10 times.

Secondly, practical cluster target consists of randomly-placed and variable-sized clusters in an ambient gas. Namely, cluster sources produce clouds of clusters of a variable size and the adjustment of the cluster size remains unsolved. At present, we are trying to control the cluster size by changing the nozzle temperature and also the shape of the conical nozzle. The adjustment of the cluster size and the cluster density is the on-going future work, and against the intent and beyond the purpose of this paper, i.e., proposing a new acceleration method.

In conclusion, in order for the present scheme to deserve practical application, further progresses about the manipulation and optimization of all-optical techniques and target fabrication are requested. This is ongoing work.

## 6.3 Future work

In this work, we assume that the clustered medium consists of a single cluster and ambient gas. That is, our viewpoint is *microscale* dynamics in the cluster medium. However, in the experimental condition, the cluster medium consists of many clusters, which would lead to *macroscale* structures, such as blast wave and large-scale and stable magnetic structure by multi-cluster effects. Therefore, we will perform large-scale simulations concerning the interaction between the clustered medium containing multi clusters and a high power laser, and investigate the multi-cluster effect coupled with the microscale structure. Also, we chose 2D simulations in order to represent laser-spherical cluster interactions and resultant dynamics. If we assume electron distribution functions artificially including the spatial dependence both for a cluster and an ambient gas at  $t = 0$  without considering the interaction with laser, it could be possible to consider and/or set-up a spherically symmetric 1D simulation. This approach is likely as a pure theoretical one and could have an advantage in discussing a universality of the phenomena, e.g. the

### 6.3. FUTURE WORK

---

parametrization of the phenomena and/or deriving a scaling law. Therefore, we would like to perform the approach as a future work.

Secondly, in order to obtain protons which are available to medical applications, such as cancer therapy,  $\sim 10^{10}$  per second protons with an energy of  $\sim 200$  MeV are required. In order to improve the probability of the laser peak intensity hitting the cluster center, at present, we are trying to control the cluster size by changing the nozzle temperature [70] and also the shape of the conical nozzle. In addition to the further development of the laser technology, the adjustment of the cluster size and the cluster density is the on-going future work.

# Bibliography

- [1] D. Strickland and G. Mourou, *Opt. Commun.* **56**, 219 (1985).
- [2] L. Romagnani *et al.*, *Phys. Rev. Lett.* **101**, 025004 (2008).
- [3] Y. Kuramitsu *et al.*, *Phys. Rev. Lett.* **106**, 175002 (2011).
- [4] H. Ahmed *et al.*, *Phys. Rev. Lett.* **110**, 205001 (2013).
- [5] N. L. Kugland *et al.*, *Nat. Phys.* **8**, 809 (2012).
- [6] J. Meinecke *et al.*, *Nat. Phys.* **10**, 520 (2014).
- [7] B. Albertazzi *et al.*, *Science* **346**, 325 (2014).
- [8] C. M. Huntington *et al.*, *Nat. Phys.* **11**, 173 (2015).
- [9] J. Posthumus, *Molecules and Clusters in Intense Laser Fields* (Cambridge University Press, 2009).
- [10] T. Fennel *et al.*, *Rev. Mod. Phys.* **82**, 1793 (2010).
- [11] T. Ditmire *et al.*, *Phys. Rev. Lett.* **78**, 3121 (1997).
- [12] T. Tajima *et al.*, *Phys. Plasmas* **6**, 3759 (1999).
- [13] Y. Kishimoto *et al.*, *Phys. Plasmas* **9**, 589 (2002).
- [14] N. Iwata *et al.*, *Phys. Plasmas* **23**, 063115 (2016).
- [15] A. McPerson *et al.*, *Nature (London)* **370**, 631 (1994).
- [16] T. Ditmire *et al.*, *Nature (London)* **386**, 54 (1997).
- [17] T. Ditmire *et al.*, *Nature (London)* **398**, 489 (1999).
- [18] I. Alexeev *et al.*, *Phys. Rev. Lett.* **90**, 103402 (2003).
- [19] K. Y. Kim *et al.*, *Phys. Rev. E* **73**, 066403 (2006).
- [20] M. McCormick *et al.*, *Phys. Rev. Lett.* **112**, 045002 (2014).

- [21] Y. Fukuda *et al.*, Appl. Phys. Lett. **92**, 121110 (2008).
- [22] Y. Fukuda *et al.*, Phys. Rev. Lett. **103**, 165002 (2009).
- [23] L. Zhang *et al.*, Appl. Phys. Lett. **100**, 014104 (2012).
- [24] L. M. Chen *et al.*, Sci. Rep. **3**, 1912 (2013).
- [25] R. Rajeev *et al.*, Nat. Phys. **9**, 185 (2013).
- [26] A. Marocchino *et al.*, Appl. Phys. Lett. **112**, 264104 (2018).
- [27] F. Wagner *et al.*, Phys. Rev. Lett. **116**, 205002 (2016).
- [28] I. J. Kim *et al.*, Phys. Plasmas **23**, 070701 (2016).
- [29] A. Higginson *et al.*, Nat. Commun. **9**, 724 (2018).
- [30] E. L. Clark *et al.*, Phys. Rev. Lett. **84**, 670 (2000).
- [31] R. A. Snavely *et al.*, Phys. Rev. Lett. **85**, 2945 (2000).
- [32] S. C. Wilks *et al.*, Phys. Plasmas **8**, 542 (2001).
- [33] J. Fushs *et al.*, Nature Phys. **2**, 48 (2006).
- [34] B. M. Hegelich *et al.*, Nature (London) **439**, 441 (2006).
- [35] H. Schworer *et al.*, Nature (London) **439**, 445 (2006).
- [36] A. Macchi *et al.*, Rev. Mod. Phys. **85**, 751 (2013).
- [37] T. Esirkepov *et al.*, Phys. Rev. Lett. **92**, 175003 (2004).
- [38] T. V. Liseikina *et al.*, Appl. Phys. Lett. **91**, 171502 (2007).
- [39] A. P. L. Robinson *et al.*, New J. Phys. **10**, 013021 (2008).
- [40] O. Klimo *et al.*, Phys. Rev. ST Accel. Beams **11**, 031301 (2008).
- [41] X. Q. Yan *et al.*, Phys. Rev. Lett. **100**, 135003 (2008).
- [42] A. Henig *et al.*, Phys. Rev. Lett. **103**, 245003 (2009).
- [43] M. Chen *et al.*, Phys. Rev. Lett. **103**, 024801 (2009).
- [44] B. Qiao *et al.*, Phys. Rev. Lett. **102**, 145002 (2009).
- [45] A. Macchi *et al.*, Phys. Rev. Lett. **103**, 085003 (2009).
- [46] C. A. J. Palmer *et al.*, Phys. Rev. Lett. **106**, 014801 (2011).

- [47] B. Qiao *et al.*, Phys. Rev. Lett. **108**, 115002 (2012).
- [48] S. Kar *et al.*, Phys. Rev. Lett. **109**, 185006 (2012).
- [49] Z. M. Zhang *et al.*, Appl. Phys. Lett. **100**, 134103 (2012).
- [50] S. Steinke *et al.*, Phys. Rev. ST Accel. Beams **16**, 011303 (2013).
- [51] J. H. Bin *et al.*, Phys. Rev. Lett. **115**, 064801 (2015).
- [52] K. H. Pae *et al.*, Phys. Plasmas **23**, 033117 (2016).
- [53] C. Scullion *et al.*, Phys. Rev. Lett. **119**, 054801 (2017).
- [54] S. Palaniyappan *et al.*, Nat. Commun. **6**, 10170 (2015).
- [55] L. O. Silva *et al.*, Phys. Rev. Lett. **92**, 015002 (2004).
- [56] D. Haberberger *et al.*, Nature Phys. **8**, 95 (2012).
- [57] F. Fiuza *et al.*, Phys. Rev. Lett. **109**, 215001 (2012).
- [58] F. Fiuza *et al.*, Phys. Plasmas **20**, 056304 (2013).
- [59] H. Zhang *et al.*, Phys. Plasmas **22**, 013113 (2015).
- [60] W. L. Wang *et al.*, Phys. Plasmas **23**, 073118 (2016).
- [61] S. N. Chen *et al.*, Sci. Rep. **7** 13505 (2017).
- [62] H. Zhang *et al.*, Phys. Rev. Lett. **119**, 164801 (2017).
- [63] Y. Fukuda *et al.*, Radiat. Meas. **50**, 92 (2013).
- [64] M. Borghesi *et al.*, Fusion Sci. Technol. **49**, 412 (2006).
- [65] A. V. Kuznetsov *et al.*, Plasma Phys. Rep. **27**, 211 (2001);
- [66] S. V. Bulanov *et al.*, Plasma Phys. Rep. **31**, 369 (2005).
- [67] T. Zh. Esirkepov *et al.*, Phys. Rev. Lett. **98**, 049503 (2007).
- [68] T. Nakamura *et al.*, Phys. Rev. Lett. **105**, 135002 (2010).
- [69] S. Jinno *et al.*, Opt. Express **25**, 18774 (2017).
- [70] S. Jinno *et al.*, Plasma Phys. Control. Fusion **60**, 044021 (2018).
- [71] T. Ditmire *et al.*, Phys. Rev. A. **53**, 3379 (1996).
- [72] H. M. Milchberg *et al.*, Phys. Rev. E. **64**, 056402 (2001).

## BIBLIOGRAPHY

---

- [73] M. Eloy *et al.*, Phys. Plasmas **8**, 1084 (2001).
- [74] K. Nishihara *et al.*, Nucl. Instrum. Methods Phys. Res. A **464**, 98 (2001).
- [75] J. Purnell *et al.*, Chem. Phys. Lett. **229** 33 (1994).
- [76] Y. L. Shao *et al.*, Phys. Rev. Lett. **77**, 3343 (1996).
- [77] M. Lezius *et al.*, Phys. Rev. Lett. **80**, 261 (1998).
- [78] V. Kumarappan, M. Krishnamurthy, and D. Mathur, Phys. Rev. Lett. **87**, 085005 (2001).
- [79] A. McPherson *et al.*, Phys. Rev. Lett. **72**, 1810 (1994).
- [80] A. McPherson *et al.*, Nature **370**, 631 (1994).
- [81] A. L. Lytle *et al.*, Phys. Rev. Lett. **76**, 2472 (1996).
- [82] T. Donnelly *et al.*, Phys. Rev. Lett. **98**, 123904 (2007).
- [83] Y. Fukuda *et al.*, JETP Lett. **78**, 115 (2003).
- [84] A. S. Boldarev *et al.*, Rev. Sci. Instrum. **77**, 083112 (2006).
- [85] S. Jinno *et al.*, Opt. Express **21**, 20656 (2013).
- [86] D. G. Jang *et al.*, Appl. Phys. Lett. **105**, 021906 (2014).
- [87] M. McCormick *et al.*, Phys. Rev. Lett. **112**, 045002 (2014).
- [88] T. Ditmire *et al.*, Astrophys. J. Suppl. Ser. **127**, 299 (2000).
- [89] D. R. Symes *et al.*, Nucl. Instrum. Methods Phys. Res. A **653**, 186 (2011).
- [90] Y. Fukuda *et al.*, Phys. Lett. A **363**, 130 (2007).
- [91] L. M. Chen *et al.*, Sci. Reports **3**, 1912 (2013).
- [92] C. Rose-Petruck *et al.*, Phys. Rev. A. **55**, 1182 (1997).
- [93] I. Last and J. Jortner, Phys. Rev. A. **62**, 013201 (2000).
- [94] K. Ishikawa *et al.*, Phys. Rev. A. **62**, 063204 (2000).
- [95] C. Jungreuthmayer *et al.*, Phys. Rev. Lett. **92**, 133401 (2004).
- [96] T. Taguchi *et al.*, Phys. Rev. Lett. **92**, 205003 (2004).
- [97] Y. Fukuda *et al.*, Phys. Rev. A **73**, 031201 (2006).

## BIBLIOGRAPHY

---

- [98] M. Murakami *et al.*, Phys. Plasmas **13**, 012105 (2006).
- [99] H. Daido *et al.*, Rep. Prog. Phys. **75**, 056401 (2012).
- [100] M. Borghesi *et al.*, Phys. Plasmas **9**, 2214 (2002).
- [101] S. V. Bulanov *et al.*, Phys. Lett. A **299**, 240 (2002).
- [102] S. V. Bulanov *et al.*, Plasma Phys. Rep. **28**, 453 (2002).
- [103] V. Malka *et al.*, Med. Phys. **31**, 1587 (2004).
- [104] K. W. D. Ledingham *et al.*, Science **300**, 1107 (2003).
- [105] N. V. Zamfir, Eur. Phys. J. Spec. Top. **223**, 1221 (2014).
- [106] M. Roth *et al.*, Phys. Rev. Lett. **86**, 436 (2001).
- [107] Y. Kitagawa *et al.*, Phys. Rev. Lett. **114**, 195002 (2015).
- [108] P. K. Patel *et al.*, Phys. Rev. Lett. **91**, 125004, (2003).
- [109] B. Dromey *et al.*, Nat. Commun. **7**, 10642 (2016).
- [110] S. Jinno *et al.*, Appl. Phys. Lett. **102**, 164103 (2013).
- [111] M. Kanasaki *et al.*, Plasma Phys. Control. Fusion **58**, 034013 (2016).
- [112] Y. Kishimoto and T. Masaki, J. Plasma. Phys. **72**, 971 (2006).
- [113] M. V. Ammosov, N. B. Delone, and V. P. Krainov, Sov. Phys. JETP **64**, 1191 (1986).
- [114] S. Katsuda, THE ASTRONOMICAL HERALD **102**, 429 (2009).
- [115] A. Macchi *et al.*, Phys. Rev. Lett. **94**, 165003 (2005).
- [116] W. L. Zhang *et al.*, Phys. Plasmas **23**, 073118 (2016).
- [117] I. B. Bernstein, J. M. Greene, and M. D. Kruskal, Phys. Rev. **108**, 546 (1957).
- [118] R. C. Davidson, *Methods in nonlinear plasma theory* (Academic, New York and London, 1972), Vol. 37, p. 75.
- [119] N. Iwata *et al.*, Phys. Plasmas **23**, 063115 (2016).
- [120] Y. Kishimoto *et al.*, J. Phys. Soc. Jpn **59**, 118 (1990).
- [121] K. Imadera *et al.*, J. Comput. Phys. **228**, 8919 (2009).
- [122] Y. Kishimoto *et al.*, Phys. Fluids **26**, 2308 (1983).

## BIBLIOGRAPHY

---

- [123] H. Matsumoto *et al.*, Geophys. Res. Lett. **21**, 2915 (1994).
- [124] L. Muschietti *et al.*, Geophys. Res. Lett. **26**, 1093 (1999).
- [125] S. Ter-Avetisyan *et al.*, Phys. Plasmas **19**, 073112 (2012).
- [126] T. M. Ostermayr *et al.*, Phys. Rev. E **94**, 033208 (2016).
- [127] D. Jung *et al.*, Phys. Rev. Lett. **107**, 115002 (2011).
- [128] B. Gonzalez-Izquierdo *et al.*, *et al.*, Nat. Commun. **7**, 12891 (2016).
- [129] S. Palaniyappan *et al.*, Nat. Phys. **8**, 763 (2012).
- [130] J. Fernández *et al.*, Phys. Plasmas **24**, 056702 (2017).
- [131] L. Yin *et al.*, Laser Part. Beams **24**, 291 (2006).
- [132] L. Yin *et al.*, Phys. Plasmas **14**, 056706 (2007).
- [133] L. Yin *et al.*, Phys. Rev. Lett. **107**, 045003 (2011).
- [134] A. Henig *et al.*, Phys. Rev. Lett. **103**, 045002 (2009).
- [135] U. Even, Adv. Chem. **2014**, 636042 (2014).
- [136] H. Kiriyaama *et al.*, IEEE J. Sel. Top. Quantum Phys. **21**(1), 232-249 (2015).
- [137] A. S. Pirozhkov *et al.*, Opt. Express **25**(17), 20486 (2017).
- [138] H. Kiriyaama *et al.*, Optics Letters **43**, 2595 (2018).

# Scientific contributions during this PhD

## Publications

1. R. Matsui, Y. Fukuda and Y. Kishimoto, “Quasimonoenergetic proton bunch acceleration driven by hemispherically converging collisionless shock in a hydrogen cluster coupled with relativistically induced transparency”, Phys. Rev. Lett. 122, 014804 (2019).
2. S. Jinno, M. Kanasaki, M. Uno, R. Matsui, M. Uesaka, Y. Kishimoto and Y. Fukuda, “Micron-size hydrogen cluster target for laser-driven proton acceleration”, Plasma Phys. Control. Fusion 60, 044021 (2018).
3. S. Jinno, H. Tanaka, R. Matsui, M. Kanasaki, H. Sakaki, M. Kando, K. Kondo, A. Sugiyama, M. Uesaka, Y. Kishimoto and Y. Fukuda, “Characterization of micron-size hydrogen clusters using Mie scattering”, Opt. Express 25 16, 18774 (2017).
4. N. Iwata, H. Nagatomo, Y. Fukuda, R. Matsui, and Y. Kishimoto, “Effects of radiation reaction in the interaction between cluster media and high intensity lasers in the radiation dominant regime”, Phys. Plasmas 23, 063115 (2016).
5. N. Iwata, Y. Kishimoto, R. Matsui and Y. Fukuda, “Laser-matter interaction in cluster medium in the radiation dominated regime”, Journal of Physics: Conference Series 688, 012038 (2016).
6. M. Kanasaki, S. Jinno, H. Sakaki, A. Ya. Faenov, T. A. Pikuz, M. Nishiuchi, H. Kiriya, M. Kando, A. Sugiyama, K. Kondo, R. Matsui, Y. Kishimoto, K. Morishima, Y. Watanabe, C. Scullion, A. G. Smyth, A. Alejo, D. Doria, S. Kar, M. Borghesi, K. Oda, T. Yamauchi, Y. Fukuda “Observation of the inhomogeneous spatial distribution of MeV ions accelerated by the hydrodynamic ambipolar expansion of clusters” Radiat. Meas. 83, 12 (2015).
7. R. Matsui, Y. Fukuda and Y. Kishimoto, “Dynamics of the boundary layer created by the explosion of a dense object in an ambient dilute gas triggered by a high power laser”, under review in Phys. Rev. E (2019).

## International presentations

1. R. Matsui, Y. Fukuda and Y. Kishimoto, “Acceleration of ambient gas ions and establishment of a kinetic equilibrium in boundary layers created by a Coulomb explosion of a cluster”, JIFT2018, Hiroshima, March 28, 2018. (oral)
2. R. Matsui, Y. Fukuda and Y. Kishimoto, “Generation of quasi-monoenergetic protons exceeding 200 MeV via intra-cluster collisionless shocks in a laser-irradiated micron-size H<sub>2</sub> cluster”, IFSA2017, Saint Malo, France, September 11-15, 2017. (poster)

3. R. Matsui, Y. Fukuda, D. Kawahito and Y. Kishimoto, “Structure and dynamics of electric fields produced in the interaction between a single cluster and a background gas irradiated by a high power laser”, HEDS2016, Yokohama, May 19, 2016. (oral)
4. R. Matsui, Y. Fukuda, D. Kawahito and Y. Kishimoto, “Structure of electric field and dynamics of contact surface due to the interaction between cluster and background gas irradiated by high power lasers”, ISUILS14, Hawaii, December 9-15, 2015. (poster)

### Domestic presentations

1. R. Matsui, Y. Fukuda and Y. Kishimoto, “Formation of quasi-stationary nonlinear waves and acceleration of ambient gas ions in boundary layers created in a cluster medium”, JPS Annual Meeting, Noda, March, 2018. (oral)
2. R. Matsui, Y. Fukuda and Y. Kishimoto, “Acceleration of 290 MeV quasi-monoenergetic protons triggered by the intracluster collisionless shocks in the relativistically-induced transparency regime”, Joint Symposium on Advanced Photon Research, Suita, May 2017. (poster)
3. R. Matsui, Y. Fukuda and Y. Kishimoto, “Acceleration of 290 MeV quasi-monoenergetic protons triggered by the intracluster collisionless shocks in the relativistically-induced transparency regime”, JPS Annual Meeting, Toyonaka, March, 2017. (oral)
4. R. Matsui, Y. Fukuda, D. Kawahito and Y. Kishimoto, “Formation of an anisotropic electric field and longitudinal acceleration of 100-MeV protons triggered by intense laser irradiation of submicron-size H<sub>2</sub> cluster media”, JPS Annual Meeting, Sendai, March 2016. (oral)
5. R. Matsui, Y. Fukuda, D. Kawahito and Y. Kishimoto, “Simulation studies on the structure formation of fields and ion acceleration due to the interaction between high power lasers and clustered media”, ILE meeting (Osaka university), Suita, January 2016. (oral)
6. R. Matsui, Y. Fukuda, D. Kawahito and Y. Kishimoto, “Forward acceleration of 100-MeV protons triggered by intense laser irradiation of H<sub>2</sub> cluster targets”, JLS Annual Meeting, Nagoya, January 2016. (oral)
7. R. Matsui, Y. Fukuda, D. Kawahito and Y. Kishimoto, “Structure of electric field and dynamics of a background gas acceleration triggered by the Coulomb explosion of a cluster”, the 16th Symposium on Advanced Photon Research, Kizugawa, November, 2015. (poster)
8. R. Matsui, Y. Fukuda, D. Kawahito and Y. Kishimoto, “Structure of electric field and dynamics of contact surface due to the interaction between cluster and background gas irradiated by high power lasers”, JPS Annual Meeting, Suita, September, 2015. (oral)

9. R. Matsui, Y. Fukuda, M. Kanasaki, H. Sakaki, N. Iwata, K. Kondo and Y. Kishimoto, “Simulation studies on acceleration of background gas ions in clustered media irradiated by high power lasers”, JPS Annual Meeting, Tokyo, March, 2015. (oral)
10. R. Matsui, Y. Fukuda, M. Kanasaki, H. Sakaki, N. Iwata, K. Kondo and Y. Kishimoto, “Simulation studies on acceleration of background gas ions due to an electric field produced by a Coulomb explosion of a cluster”, the 15th Symposium on Advanced Photon Research, Kizugawa, November, 2014. (poster)
11. R. Matsui, Y. Fukuda, M. Kanasaki, H. Sakaki, N. Iwata, K. Kondo and Y. Kishimoto, “Simulation studies on the structure formation of fields and ion acceleration due to the interaction between high power lasers and clustered media”, Quantum Beam Science Center Meeting, Himeji, August, 2014. (poster)
12. R. Matsui, N. Iwata, Y. Fukuda and Y. Kishimoto, “Simulation studies on an interaction between a high power laser and clustered media”, JPS Annual Meeting, Hiratsuka, March, 2014. (oral)
13. R. Matsui, Y. Fukuda and Y. Kishimoto, “Laser-cluster media interaction and ion acceleration”, ILE meeting (Osaka University), Suita, January 2014. (oral)

### Awards

1. R. Matsui, “Acceleration of 290 MeV quasi-monoenergetic protons triggered by the intracuster collisionless shocks in the relativistically-induced transparency regime”, Student Best Presentation Award, JPS Annual Meeting, Toyonaka, March, 2017.

### Domestic patents

1. Y. Fukuda, Y. Kishimoto and R. Matsui, “Method of the production of high-energy monoenergetic proton beam using Hydrogen cluster target”, submitted on 16 March 2016, reference number: 2016-051832